THE SEA BREEZE AT MONTEREY BAY: COMPARISONS BETWEEN LIDAR MEASUREMENTS AND TWO-DIMENSIONAL NUMERICAL SIMULATIONS

Lisa S. Darby

NSF Grant No. ATM-9910857
Roger A. Pielke, P.I.

Colorado State University

DEPARTMENT OF ATMOSPHERIC SCIENCE

PAPER NO. 710

THE SEA BREEZE AT MONTEREY BAY: COMPARISONS BETWEEN LIDAR MEASUREMENTS AND TWO-DIMENSIONAL NUMERICAL SIMULATIONS

Lisa S. Darby

Department of Atmospheric Science
Colorado State University
Fort Collins, Colorado
Spring 2001

Atmospheric Science Paper No. 710

ABSTRACT

THE SEA BREEZE AT MONTEREY BAY: COMPARISONS BETWEEN LIDAR MEASUREMENTS AND TWO-DIMENSIONAL NUMERICAL SIMULATIONS

The NOAA/ETL TEA CO_2 Doppler lidar measured the life cycle of the land- and sea-breeze system along the California coast under various synoptic conditions during the Land and Sea Breeze Experiment (LASBEX) in September, 1987. The lidar was stationed at Moss Landing, 1.5 km east of the shore of Monterey Bay, measuring winds on 12 days. On days with offshore synoptic flow, the transition to onshore flow (the sea breeze) was a distinct process easily detected by lidar. Fine-scale lidar measurements showed the reversal from offshore to onshore flow near the coast, and its gradual vertical and horizontal expansion. Lidar scans taken along an east/west cross-shore line, horizon-to-horizon, on days with ambient offshore flow, showed a dual structure to the sea breeze flow in its early formative stages. First, a shallow (<500 m) sea breeze formed which later became embedded in a weaker onshore flow that was ~1 km deep. Eventually these two flows blended together to form a mature sea breeze at least 1 km deep.

Regional Atmospheric Modeling System (RAMS) two-dimensional simulations successfully simulated this dual structure of the sea breeze flow when both the coastal

mountain range just east of Monterey Bay and the Sierra Nevada range, peaking 300 km east of the shore, were included in the domain. Various sensitivity simulations were conducted to isolate the roles played by the land/water contrast, the coastal mountain range, and the Sierra Nevada range. Notable results include 1) the Sierra Nevada Range greatly affected the winds above 1500 m at the shore, even though the peak of the mountain range was 300 km east of the shore, 2) the winds at the shore, below 1500 m, were most affected by the land/sea contrast and the coastal mountain range, and 3) the presence of the coastal mountain range enhanced the depth of the sea breeze flow, but not necessarily the speed of it.

A factor separation method was employed to further isolate the contributions of the terrain and land/water contrast to the vertical structure of the modeled u-component of the wind. When both mountains were included in the domain, the interaction of the slope flows generated by these mountains acted to strongly enhance onshore flow early in the morning, and then enhance a return flow layer during the day. In contrast, the interaction of flows generated by the land/water contrast and the sloping terrain had its strongest effect late in the afternoon and early evening, working to oppose the sea breeze flow. The triple interaction of the flows generated by the coastal mountain, inland mountain, and the land/water contrast enhanced the sea breeze flow from the surface to 500 m ASL throughout the day.

Lisa S. Darby
Department of Atmospheric Science
Colorado State University
Fort Collins, Colorado 80523
Spring 2001

ACKNOWLEDGMENTS

I would like to thank my advisor, Dr. Roger Pielke, Sr., for his support and his scientific contributions to this thesis. I also thank Drs. Richard Johnson and Chiao-Yao She who served on my committee. This thesis is based on work completed by Dr. Robert Banta at the NOAA/Environmental Technology Laboratory. His in-depth analysis of the lidar data obtained at Monterey Bay forms the basis for the motivation for and the analysis of the model simulations presented in this paper. His encouragement and creativity is greatly appreciated. Dr. R. Michael Hardesty's support was instrumental in making this thesis work possible.

I would also like to thank the following people for helping me to successfully use RAMS: Drs. Greg Poulos, Cathy Finley, Robert Walko, and Graham Feingold.

TABLE OF CONTENTS

Chapter 1

Introduction

1.1 Motivation

The sea breeze is a thermally direct circulation that has been studied with varying degrees of sophistication for many years (Atkinson 1981; Pielke 1984; Simpson 1994). Just spending time near the shore of any large body of water allows one to qualitatively experience the diurnal cycle of the breezes associated with the land/water contrast. Its simplicity lends itself well to analytical and numerical modeling. However, there are components of the sea breeze that have been difficult for researchers to measure in detail, such as the structure of the winds over the water.

The development of clear-air remote sensing instruments has allowed researchers to observe the land- and sea-breeze cycle in detail. A Doppler lidar developed and deployed by the National Oceanic and Atmospheric Administration/Environmental Technology Laboratory (NOAA/ETL), measured the land- and sea-breeze circulations at Monterey Bay, CA, in September of 1987, during the LAnd/Sea Breeze Experiment (LASBEX). While stationed at Moss Landing (Fig. 1.1), ~1.5 km from the shore, the ETL lidar regularly scanned from horizon-to-horizon along an east-west line (perpendicular to the shore), capturing the evolution of the land- and sea-breeze flows under different synoptic conditions. Of particular interest was the vertical structure of the

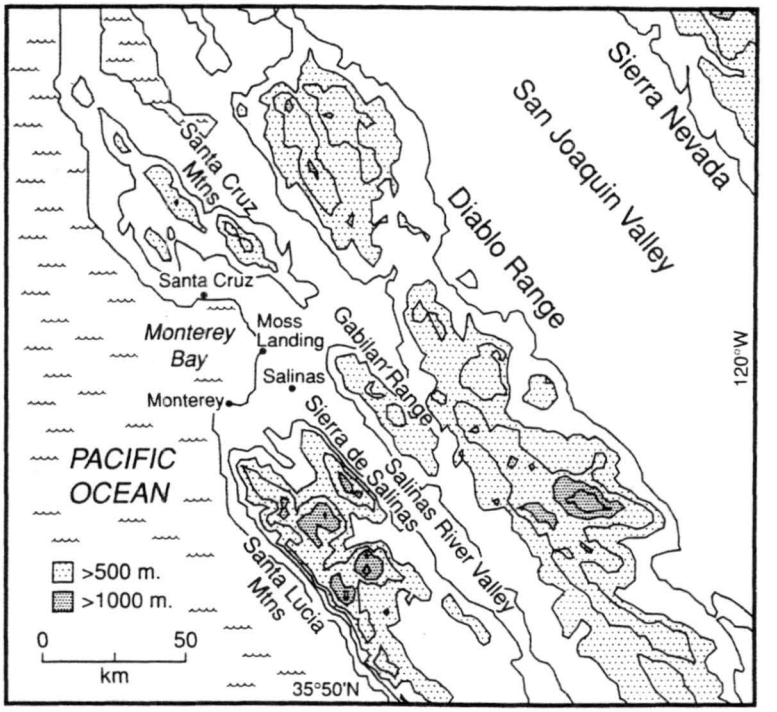

Figure 1.1a Terrain map of region surrounding Monterey Bay (from Banta et al. 1993). (a) Mountain ranges and valleys impacting the coastal wind flows. Terrain above 500 m has light shading and terrain greater than 1000 m has dark shading.

sea breeze as revealed by this type of scan. On at least 2 days during LASBEX that began with offshore synoptic flow, the sea breeze included two scales of flow: a shallow, stronger sea breeze imbedded in a weaker, deeper sea breeze (Banta et al. 1993; Banta 1995). These two flows eventually merged into a well-blended layer of onshore flow ~1 km deep. The purpose of this study is to ascertain whether the Regional Atmospheric Modeling System (RAMS) can reproduce these two scales of onshore flow on a day with ambient offshore flow and to perform terrain sensitivity studies to give insight into the role that the complex terrain east of Monterey Bay plays in the vertical structure of the sea breeze.

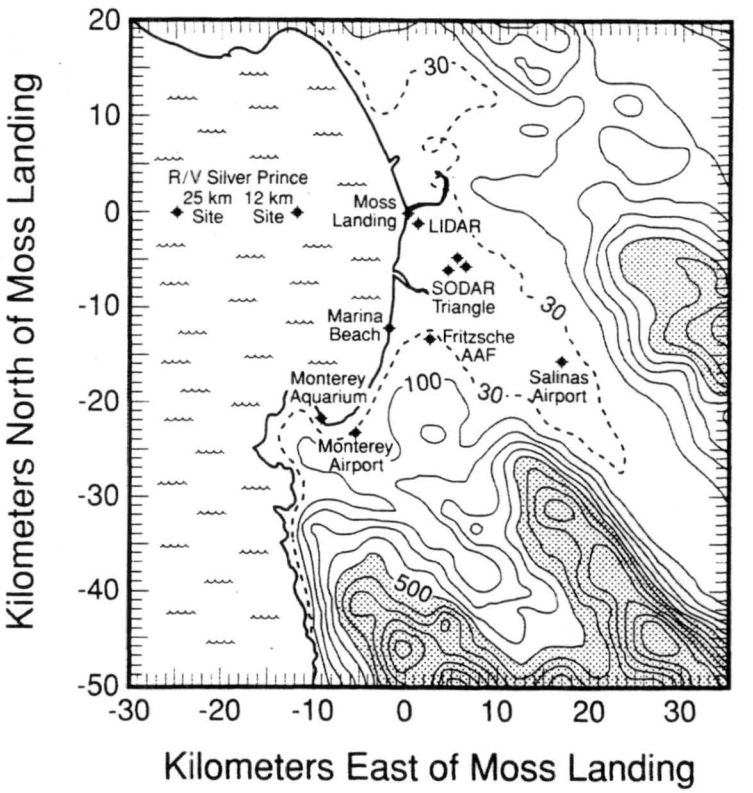

Figure 1.1b Smaller-scale map of region. Locations of sensors and sites with routine surface meteorological measurements. The dashed terrain contour is 30 m above sea level. Solid terrain contours are at 100-m intervals. Terrain above 500 m is shaded (originally adapted from Fagan, 1988).

The remainder of this section includes a brief discussion of the physics of the sea breeze flow. Section 2 is a literature review of sea breeze observation papers and an overview of the Land/Sea Breeze Experiment, with an emphasis on the Doppler lidar measurements. A literature review of nonlinear modeling of the sea breeze, modeling sensitivity studies, and a brief overview of RAMS are in Section 3, including the description of the model setup used for the simulations in this paper. Section 4 contains model results from 2-D simulations with various terrain configurations and different choices of vegetation. Section 5 reviews the factor separation method of Stein and Alpert

(1993), and includes the application of this method to various pairs of factors from our model results. Conclusions and ideas for future work are in Section 6.

1.2 The land/sea breeze circulation

The sea breeze flow is driven by the temperature difference between land and water. Since the heat capacity of a large body of water is high, the sea surface temperature is nearly constant throughout the course of a day. As the adjacent land mass heats up early in the day, the air mass over the land has greater vertical expansion than the air mass over the water. Thus, lines of constant pressure slope downward toward the water. Lines of constant density, however, slope downward over the land.

The circulation theorem, as derived in Holton (1992), is

$$\frac{DC_a}{Dt} = -\oint \rho^{-1} dp, \tag{1.1}$$

where C_a is the absolute circulation, ϱ is density, and p is pressure. The term on the right-hand side is the solenoidal term, representing the circulation across the shore line caused by the intersection of the sloping lines of constant pressure and density. The top and bottom branches of the circulation are bounded by lines of constant pressure.

Substituting the ideal gas law, $p = \rho RT$, into Eqn. (1.1) yields

$$\frac{DC_a}{Dt} = -\oint RT d\ln p. \tag{1.2}$$

Integrating around the circuit gives

$$\frac{DC_a}{Dt} = R\ln\left(\frac{P_0}{P_1}\right)\left(\bar{T}_2 - \bar{T}_1\right) > 0, \tag{1.3}$$

the rate of increase of the circulation resulting from the pressure differences with height (p_0 is pressure at the surface and p_1 is pressure aloft) and the temperature differences over land (T_2) and water (T_1). The greater the temperature difference across the shore line, the stronger the circulation. The lower branch of this circulation is the sea breeze. The upper branch is the return flow, wind flowing from land toward the sea. To provide mass continuity for this closed circulation, upward vertical velocity over the heated land mass and subsidence over the water is required. At night, when the land surface cools to a temperature less than the surface temperature of the water, the circulation reverses (the land breeze). The land breeze is shallower and weaker than the sea breeze because 1) the temperature gradient at night between the land and water is weaker than during the day, and 2) the air mass in contact with the land has greater stability.

The circulation theorem does not account for the opposing force of friction or the deflection of the sea-breeze flow by the Coriolis effect. Haurwitz (1947) shows that frictional forces, assumed to oppose the sea breeze with a force proportional to the onshore wind velocity, cause the onshore flow to weaken before the temperature difference between the land and water reaches its maximum. Haurwitz (1947) and Schmidt (1947) also show that in the northern hemisphere the Coriolis effect will cause the sea breeze to veer with time. Subsequent observations, discussed in Section 2.1, show that the sea breeze does not necessarily veer with time, as do the LASBEX observations shown in Section 2.2. Reasons for this include the influence of strong synoptic flow and the lack of a closed circulation (Banta et al. 1993). And finally, the circulation theorem does not include the effects of self-modification inherent in the sea-

breeze circulation, such as the weakening, due to the onshore flow, of the temperature difference that drives the circulation.

Atkinson (1981) provides a comprehensive overview of sea breeze research and states that the two most important meteorological features that influence the sea breeze are the gradient wind and stability. The gradient wind influences the sea breeze strength by weakening or intensifying the temperature gradient at the shore. If the gradient wind is onshore, then the horizontal temperature gradient at the surface near the shore is weak, causing a weaker circulation to develop than on days with offshore flow. While the sea breeze superimposed on an onshore gradient wind will be weaker due to the weaker temperature gradient, the inland propagation of the marine air will be enhanced by the onshore gradient flow. The opposite occurs for an offshore gradient flow. The thermodynamic stability also affects the inland penetration of the sea breeze front. As the air over the land becomes more unstable, the sea breeze penetrates farther inland.

Topography is also an important factor in the development of the sea-breeze circulation. Central California has coastal mountain ranges, a hot interior valley, and the steep Sierra Nevada range (Fig. 1.1). Frenzel (1962), when describing the winds in the central valley of California, summed up the main factors influencing the valley winds as 1) differential heating between land and water, 2) diabatic heating of sloping terrain, and 3) the constraining influence of topography. These factors can also be applied to the winds at Monterey Bay, as will be shown.

The barrier effects of the coastal mountain ranges along the west coast of the United States have been investigated both through observations (Johnson and O'Brien

1973; Schroeder et al. 1967) and numerical modeling (Doyle 1997 and Cui et al. 1998, for example). The along-shore flows and sea-breeze flows affect each other. Large-scale onshore flow, often caused by a subtropical high over the Pacific, is blocked by the coastal mountain ranges along the coast, prompting the coastal winds to become northerly. This leads to upwelling, colder water rising to the surface, and a decrease in the sea surface temperatures, which increases the temperature gradient across the coastline between land and water (Johnson and O'Brien 1973; Mizzi and Pielke 1984), driving a stronger sea breeze. In turn, the presence of the sea breeze imposes a diurnal cycle on the along-coast flow (Cui et al. 1998). Topographical flows influence the along-shore pressure gradients that feed the coastal jet (Doyle 1997). Another influence on the temperature gradient across the shore is the separation of the cool, moist marine air from the hot, dry interior valley air by a coastal mountain range (Schroeder et al. 1967; Johnson and O'Brien 1973).

The behavior of the sea breeze in the complex topography of Japan has lead researchers to conclude that inland mountain ranges do have an effect on the sea-breeze flow. It is possible for the subsidence associated with the return flow of the upslope flow of an inland mountain to warm the nearby plain, creating an extended sea breeze (a sea breeze with greater vertical extent and inland penetration than a sea breeze propagating inland over flat terrain) (Kitada et al. 1998). On the Nohbi Plain of Japan, Kitada et al. (1998) show that the Japanese Alps, 100-200 km from the shore, helped to maintain the onshore flow into the evening hours in this way, providing evidence that inland mountain ranges can affect the flow at the shore. Kimura and Kuwagata (1993) also present

observations from Japan of an extended sea breeze due to enhancement from a mountain range that peaks more than 100 km from the shore. A thermal low in the basin beyond this mountain range further enhanced the inland intrusion of marine air, along with the downslope flows that formed at night, having strong implications for the transport of pollutants.

While the topography in Japan is quite different from the topography of California, the concepts presented in the above referenced papers apply to studies of the sea breeze flow along the California coast. In addition to these larger-scale influences of terrain, sloping terrain near the shore complicates the horizontal and vertical structure of the sea and land breezes with the addition of slope flows and gaps in the terrain through which the sea- and land-breeze flows can be channeled. These complications cause the structure of the sea breeze to deviate from theoretical predictions (Frenzel 1962).

Chapter 2

Sea and land breeze observations

2.1 Literature review

2.1.1 Vertical structure of the sea-breeze circulation

Early studies of the sea breeze and land breeze circulations often included vertical cross sections of winds and temperature measured by balloon-borne instruments, which required interpolation and smoothing of the data. These measurements provided much information regarding the time evolution of the vertical structure of the sea breeze winds and temperature, including the inland propagation of the marine air. However, the spatial and temporal resolutions of these types of measurements were coarse.

A constant theme in sea breeze observational studies is the question of how to differentiate the sea breeze flow from the ambient wind field. Observations of the return flow and the veering (in the northern hemisphere) of the sea-breeze flow with time due to Coriolis, can be masked or altered by the larger-scale winds. Considering these issues, sea breeze observationalists often prefer quiescent synoptic conditions for measurements, i.e., light winds and clear skies, to isolate the land- and sea-breeze circulation. On the other hand, investigating the differences in the behavior of the sea breeze under different types of synoptic conditions resulting in different ambient flow regimes (onshore, offshore, or parallel to the shore) is another fruitful area of land- and sea-breeze research.

Fisher (1960) studied the vertical structure of the land and sea-breeze circulations over both land and water with pilot balloons launched from 5 stations. These stations comprised a line of measurements straddling the coast, extending +/- 25 km across the shore of Rhode Island. To gather measurements over the water, the pilot balloons were launched from a ship and an island deemed small enough not to influence the sea breeze structure over water. Measurements from a buoy also helped to fill the gap in measurements over the water. The cross sections drawn from these measurements documented the time evolution of the vertical structure of the wind, both perpendicular and parallel to the coast, from the surface to ~ 1800 m AGL. A light plane measured temperatures below 760 m along the line created by the pilot balloon stations.

In both days studied, the onshore component of the flow increased in speed and depth throughout the day, the maximum winds seen near the Rhode Island coast. The transition was gradual enough that no frontal structure to the leading edge of the intruding marine air mass was evident. The sea breeze reached a depth of ~900 m, with a maximum speed of ~15 m s^{-1}. A return flow was more obvious on one day than the other due to the larger scale wind direction opposing the return flow on one of the days. The author concluded that it is difficult to completely separate the sea-breeze circulation from the ambient wind and that the large-scale flow can retard the return flow. When assessing the effect of Coriolis, again the ambient wind was a factor. The sea breeze did not veer with time as expected. However, comparing coastal observations with inland observations showed that the amount of backing that occurred inland due to the larger scale flow was more than the amount of backing measured at the coastal station. In other

words, although the winds did not veer, Coriolis may still have influenced the coastal sea-breeze flow by reducing the backing due to the large-scale winds. A final key observation by Fisher was the decoupling of the sea breeze flow from the surface as the nocturnal cooling began and the stability near the surface increased, with the sea-breeze flow forming what appeared to be a low-level jet.

Johnson and O'Brien (1973) show other examples of measurements taken along a line perpendicular to the shore. No soundings were launched over the water, but measurements taken from 5 buoys within 55.6 km of the coastal city of Newport, Oregon provided some information about conditions over water. Cross sections were derived from soundings launched from 3 land stations, one at Newport, one ~ 30 km inland, and another one ~60 km inland. The characteristics observed included a sea-breeze front propagating inland, a wind maximum trailing the front, the sea breeze flow capped by the marine inversion, and easterly flow above the sea breeze. The easterly flow aloft gained strength and depth as the sea breeze also strengthened and deepened. Since the surges in this easterly flow coincided with surges in the sea breeze, Johnson and O'Brien concluded that these winds were a return flow because they were responding to the sea breeze flow. However, with data from only three soundings, the spatial resolution of these measurements was coarse. Though there was a rise in terrain across this study region, the authors felt that the terrain did not impact the sea-breeze flow because the height of the terrain did not exceed the height of the marine inversion. A veering in the winds due to Coriolis was not seen in their data.

When comparing temperature measurements from buoys to temperatures from the

land stations, the authors theorized that there were 2 scales of forcing involved in the onshore flow. Between the open ocean and the hot interior valley there was a temperature difference of 7° C /100 km while a pair of stations closer to the shore (also a buoy and a land station) showed a difference of 5° C/20 km. With the landward penetration of marine air, the cooler marine air may reduce the valley heating, leading to a decrease in the pressure gradient across the coast, thus decreasing the thermal forcing that drives the sea breeze.

Lyons and Olsson (1973) investigated the lake breeze in Chicago, IL, with an extensive array of instrumentation, including a dense network of surface stations, satellite imagery, time-lapse photography, pilot balloons, tetroons, and aircraft. While the sea-breeze return flow can be a nebulous feature for researchers, Lyons and Olsson (1973) use the presence of a return flow as an indication of when the onshore flow was a lake breeze (wind driven by the temperature difference between land and lake water) as opposed to a synoptically driven flow. Measurements showed that the Chicago lake breeze has a structure similar to that of observed sea breezes: development at the shore that with time extends horizontally over both land and water, a depth of 500 - 1000 m, a frontal convergence zone, a change in temperature and moisture with the passage of the front, and cloud formation along the convergence zone. A nice addition to this observational paper is the measurement of airborne particles by the instrumented aircraft. It was found that it is possible for the smaller particles to drift inland with the lake breeze, rise in the frontal updraft, stay suspended in the return flow layer, advect over the lake, and sink in the subsiding air, ready to be transported to the shore the next day. This of

course has major implications for industrialized coastal areas, where pollutants can be recirculated back into the city (see also Eastman et al. 1995).

2.1.2 Sea-breeze fronts

Atkins and Wakimoto (1997) used dual-Doppler radar analyses to reconstruct the wind field associated with the sea breeze front. The convergence of winds between an ambient offshore flow and a marine air intrusion creates enhanced reflectivity in the radar data, possibly due to a higher concentration of insects in the convergence zone, making the sea breeze front easily distinguishable by radar. Their analyses show that radar backscatter, divergence, horizontal vorticity, and upward vertical velocity are all enhanced in the sea-breeze frontal region. A final step in the dual-Doppler analysis was to remove the mean wind from a vertical-slice vector plot of the winds surrounding the frontal region. An enhanced flow above and opposing the sea breeze flow, a return flow, was evident.

Another interesting feature of this paper was the density current calculations applied to sea breeze fronts in 3 different flow regimes (ambient flow that is onshore, offshore, or parallel to the shore) and thunderstorm-generated gust fronts. Sea breeze fronts on days with ambient offshore or flow parallel to the shore had Froude numbers similar to the thunderstorm gust fronts, all falling within the boundaries of density current theory. Days with ambient onshore flow did not have a well-formed sea-breeze front.

Other papers concerned with the behavior of sea-breeze fronts include Simpson et al. (1977) who measured the inland penetration of sea-breeze fronts across the coast of England. It was noted that often the sea-breeze fronts gained definition and speed later in

the afternoon. Comparisons between the measurements of sea-breeze fronts and water-tank models indicated that sea-breeze fronts have characteristics similar to density currents. For instance, one of their examples shows that aircraft measurements of mixing ratios in a sea-breeze frontal region compared very well to the distribution of dye in a water-tank modeled front.

Reible et al. (1993) continued the investigation of the afternoon development of the sea breeze front as documented in Simpson et al. (1977), using measurements of temperature and humidity from a light aircraft. The front can be diffuse at the coast line and gain definition and strength as it propagates inland. This difference in frontal structure is determined by the balance between the convergence of the winds at the front, which enhances frontogenesis, and the turbulent convective mixing, which serves to oppose frontogenesis. The convergence of winds that enhances frontogenesis may also inhibit the inland penetration of the sea breeze. It is possible, however, as Reible et al. (1993) show, that the frontogenesis may be strong enough to promote landward propagation of the sea-breeze front even with ambient offshore flow. They developed an equation that predicts the tendency for frontogenesis based on this balance between the convergence of winds and turbulence.

Holland and McBride (1989) also found similarities between sea breeze fronts and density currents, including Kelvin-Helmholtz billows, and mixing between marine and continental air in the wake region of the front, behind the head. They used a parachute-borne sonde floating in the sea-breeze frontal region to obtain measurements.

Nakane and Sasano (1986) documented the shape and turbulent structure of the

sea breeze front on the Kanto Plain of Japan (~60 km NE of Tokyo) using an aerosol lidar. A region of higher backscatter separating the different air masses defined the sea breeze front. The difference in backscatter implies a difference in aerosol concentration. Lidar measurements detected the rising of the continental air mass over the sea-breeze front and billows behind the sea-breeze front due to Kelvin-Helmholtz instability.

A ground-based aerosol lidar on the shore of the Black Sea, paired with pilot balloon measurements, captured the transition from offshore to onshore flow (Kolev et al. 1998). Again, the backscatter field was considered a relative measure of the aerosol concentration, with cleaner (lower backscatter values) air associated with the offshore flow. The authors theorize that the higher backscatter values associated with the air mass over the water were due to either the increased humidity and aerosol growth as the air moved over the Black Sea or the possibility that this air mass was an air mass that had remained over the water for an extended period of time. The combination of lidar and balloon measurements revealed the seaward motion of the cleaner air in the morning, the transition to marine air moving inland, and a recirculation signature, or return flow.

While sea-breeze fronts receive most of the attention in the literature, there have been observations of land-breeze fronts. Meyer (1971) observed a land breeze front 2 days in a row in August of 1969, while a high-pressure system dominated the region under study. A radar on Wallops Island, Va., detected a 'thin line' offshore during routine scanning. The enhanced echo region formed in the convergence zone of the offshore land-breeze flow and light onshore ambient winds. Constant elevation angle and constant azimuth angle scans documented the advance and retreat of the land-breeze

front, as well as its dissipation. Surface station data confirmed the presence of a land breeze front.

2.1.3 Sea-breeze climatologies

In contrast to detailed measurements of the land- and sea-breeze cycle, there are sea breeze studies aimed at establishing a climatology of the sea-breeze flow for a region. Mizuma (1995) used long-term surface observations to establish a classification scheme for the sea breeze characteristics at Osaka Bay in Japan. Numerous factors affect the winds in this region: A bay, islands in the bay, the nearby ocean, and the surrounding complex terrain. Mizuma used hourly vector-mean winds gathered from 2 years of measurements from surface stations to classify the Osaka Bay sea breeze into 5 major types. Some features of note were the measurements of a combined upslope and sea breeze flow, converging sea breezes from both major coasts of Japan, and the evolution of breezes driven by the contrast between land and the bay, or the land and the sea. The purpose of Mizuma's study was to have a comprehensive data set for model verification.

Skinner and Tapper (1994) were interested in developing a sea breeze climatology for spring time in Melville and Bathurst Island, Australia. In the spring, significant deep, moist convection develops in this region, and Skinner and Tapper wanted to ascertain the sea breeze's role in thunderstorm initiation. From the climatology of the land and sea breezes, they assessed the divergence patterns associated with them, which coincided with thunderstorm initiation. They also focused on the surface energy balance and radiation regimes. Three broad categories emerged from their analysis: pre-monsoon inter-tropical convergence zone, monsoon, and the breakdown of the monsoon.

As indicated by this overview, there are numerous features of the sea-breeze circulation that researchers are interested in investigating, especially the vertical structure of the winds and temperature of the sea breeze, including the front. These features are quite important for air pollution transport and dispersion issues, a common motivation for studying the sea breeze. While many investigators present detailed measurements of a given sea-breeze phenomenon, they are usually quite limited in the areal distance they can cover, and accordingly are limited in the number of features to measure. It is difficult to simultaneously measure the sea breeze with high spatial and temporal resolutions. If the focus is on the vertical structure, as it usually is, then the horizontal variability of the winds will be missed. Because of these difficulties, investigators have turned to numerical modeling to better understand the sea breeze.

2.2 The Land/Sea Breeze Experiment (LASBEX)

The introduction of clear-air remote sensing instrumentation to the research community has helped to alleviate some of the restrictions on the time and spatial scales of measurements experienced in earlier sea breeze experiments. The work presented by Atkins and Wakimoto (1997), which consisted of radar observations imbedded in a dense network of research instrumentation, is an excellent example. During LASBEX, wind measurements from a Doppler lidar deployed at Monterey Bay provided unprecedented measurements of the vertical and horizontal structure of the winds over many hours at a time. Sweeps of lidar data take 3 min or less to complete, allowing for high temporal resolution surveillance of wind features and the transitions that occur in response to the diurnal heating and cooling cycle. Features measured by the lidar include the transitions

between offshore and onshore flow, the vertical and horizontal expansion of the sea-breeze flow, the variability of the flow due to the nearby terrain, the absence of a Coriolis effect on the sea-breeze winds, and the absence of a consistent, compensatory return flow (Banta et al. 1993; and Banta 1995). One of the most significant and interesting findings was the two scales of onshore flow, seen in the vertical structure of the lidar measurements, as a shallow sea breeze imbedded in a weaker, deeper sea breeze, that developed on days with ambient offshore flow.

2.2.1 Instrumentation

For LASBEX, researchers from several institutions studied the life cycle of the land- and sea- breeze circulation at Monterey Bay, California in September of 1987. Intrieri et al. (1990) present a description of instruments used in the study and preliminary results. A synopsis of their paper follows.

September was chosen for the study because climatology indicated a higher incidence of sea breezes and less fog than at other times of the year. The ETL [known as the Wave Propagation Laboratory (WPL) at the time] Doppler lidar, the Pennsylvania State University Doppler sodar, and the Naval Post Graduate School (NPS) monostatic sodar measured winds. The Louisiana State University and the NPS launched soundings to measure pressure, temperature, and relative humidity. There were 6 surface stations deployed by NPS and the Naval Environmental Prediction Research Facility (NEPRF, now the Naval Research Laboratory) that measured pressure, temperature, relative humidity, and winds. The research vessel (R/V) Silver Prince was available for 8 days of the experiment. From either 11 km or 22 km from the shore, directly west of the lidar

site, 28 soundings were launched from the R/V Silver Prince by NPS and meteorological observations 5 m above the water surface were taken throughout LASBEX. Instrumentation sites are shown in Figure 1.1b.

Central to the experiment was the ETL Doppler lidar. A lidar is a laser-based remote sensing instrument, similar to a Doppler weather radar. The technical aspects of the Doppler lidar deployed at LASBEX are discussed in Post and Cupp (1990). Characteristics of this lidar are shown in Table 2.1. Two general characteristics of lidar that set it apart from radar are 1) a narrow beam and 2) no ground-clutter. The narrow beam allows for high resolution scanning measurements, and the lack of ground clutter allows the lidar to obtain measurements close to terrain. These characteristics make the lidar particularly useful in a complex terrain setting. In addition to the LASBEX papers incorporating Doppler lidar data (Intrieri et al. 1990; Banta et al. 1993; and Banta 1995), numerous studies have been published using ETL Doppler lidar data obtained in other complex terrain settings, such as the Rocky Flats Plant northwest of Denver, CO (Darby et al. 1999), the Grand Canyon (Banta et al. 1999), and Vancouver, B.C. (Banta et al. 1997). In all cases the lidar measured flows with spatial and temporal resolutions that could not have been measured by conventional instrumentation.

As the lidar scans, the emitted light is scattered back to the detector by aerosols 1-3 μm in size. The Doppler shift of the scattered light due to the motion of these aerosols along the beam is detected, and a radial velocity, u_r, is calculated from this Doppler shift. The backscattered signal intensity, analogous to a radar's reflectivity field, is dependent on the aerosols' size, shape, composition, and concentration. The beam is attenuated by

Table 2.1 Characteristics of the transverse-excited atmospheric pressure (TEA) CO_2 Doppler lidar deployed at LASBEX.

Typical parameters for the TEA CO_2 Doppler lidar	
Wavelength (Fully eye-safe)	10.59 μm
Pulse energy	0.5 J
Maximum range	up to 30.00 km
Minimum range	1.50 km
Scan coverage	upper hemisphere to 3° below horizon
Along-beam resolution	300.00 m
Across-beam resolution	1 m
Beam width	90 μrad or 0.005°
RMS velocity accuracy	60.00 cm s^{-1}
Calibrated backscatter	3 dB or better
Pulse repetition frequency	10.00 Hz
Pulses averaged	3.00

fog, cloud, and precipitation. The nominal maximum range of 30 km is most likely achieved in a dry, polluted environment. During LASBEX the maximum horizontal range, when no fog was present, was typically 10-15 km. Research goals for the Doppler lidar deployment at LASBEX included: 1) measurements of the radial winds to map out the three-dimensional structure of the land- and sea-breeze circulations and smaller-scale circulations embedded in the land breeze and sea breeze, 2) assessing the usefulness of using the lidar's backscattered signal intensity field to infer the distribution of aerosols within the sea- and land-breeze flows, and 3) testing the Doppler lidar's performance in a marine environment. LASBEX was the first deployment of an ETL

Doppler lidar near a coastline, and it was not clear how the high relative humidity would affect lidar measurements. Fortunately, the abundance of aerosols >1 μm in diameter in this marine environment during LASBEX enhanced the lidar signal.

The lidar scanning strategy included range-height indicator (RHI) scans, during which the scanning mirrors remain at a constant azimuth while varying in elevation, and plan-position indicator (PPI) scans during which the scanning mirrors maintain a constant elevation angle while varying in azimuth. The east-west RHI's proved invaluable for assessing the vertical structure of the land- and sea-breeze flows. Measurements from these scans are central to this study. RHI scans along the Salinas River Valley were also very useful. Low-angle (1° - 3°) PPI scans revealed much information about the horizontal variability of the winds at Monterey Bay.

2.2.2. Data analysis

2.2.2.1 Surface data

The 12 days of lidar data were organized by categorizing them according to the type of transition to sea-breeze flow that occurred in the morning. Surface data from a meteorological measuring station near the lidar were used to categorize the days. Wind direction, wind speed, mixing ratio, and temperature time series were analyzed and grouped into one of three categories: Abrupt, gradual, or in-between. Fig. 2.1 (from Banta et al. 1993) shows an example of each type of day. In the top two plots, an abrupt shift to westerly flow, with an accompanying increase in wind speed, occurred at 1800 UTC (1000 am LST). The temperature dropped impressively as the cooler air mass behind the sea breeze front advected landward. On days with this type of transition the

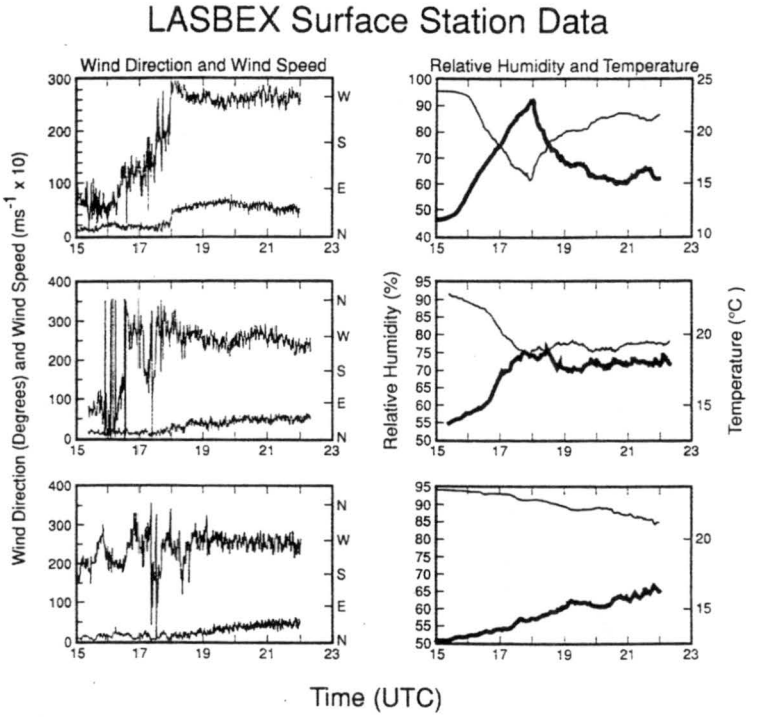

Figure 2.1 Surface data from LASBEX showing 3 different types of offshore to onshore transition (from Banta et al. 1993). Surface station traces of temperature, mixing ratio, wind direction, and wind speed at the primary sodar site for the three types of day observed during LASBEX. The top pair is for an abrupt day (29 September 1987). The sharp drop in temperature, sudden increase in wind speed, and the shift from land breeze to sea breeze are evident. The bottom pair (23 September 1987) is for a gradual day. Such days did not have a sharp change in temperature, and the wind speed increased more gradually. The middle pair (24 September 1987) is for an in-between day. The wind shift, increase in wind speed, and drop in temperature are not as abrupt as during the offshore days, but more well defined than during the gradual days.

early morning ambient winds had an offshore flow component. These were optimum days for the lidar to capture the development of the sea breeze because even in its earliest stages it was easily distinguishable from the ambient flow. Additionally, because of the

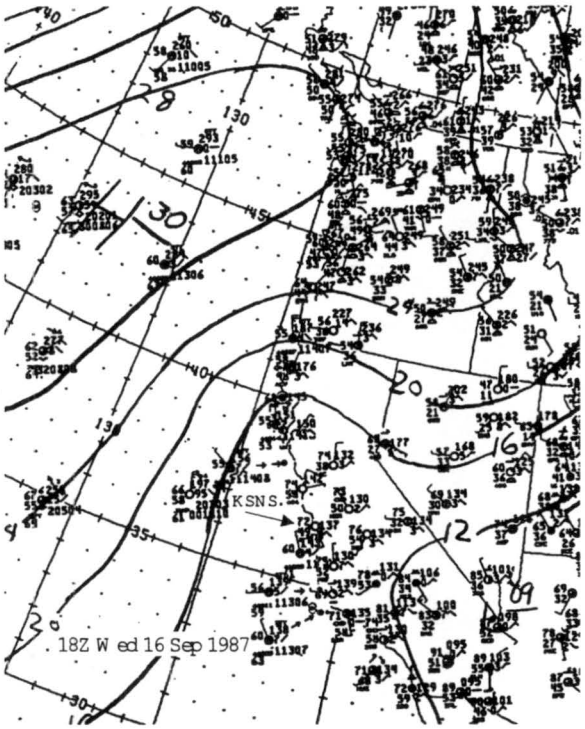

Figure 2.2a Synoptic map for the western United States. A red box surrounds the Monterey Bay region. 1800 UTC, 16 September 1987.

offshore component, fog was not hugging the shoreline on these days as on many other days in September. Five days of lidar data fell into this category.

The bottom plots show a change from weak flow with an onshore component to an onshore flow with stronger winds and less directional variability. The onset of the sea breeze (defined as steady westerly flow) occurred about an hour later than on the abrupt day. The temperature dropped slightly with the onset of the sea breeze, unlike the abrupt day. Four days of lidar data fell into this category.

The middle two panels show a transition with characteristics more well defined than the gradual day, but not as swift as the abrupt day. The large-scale flow on these days was nearly parallel with the shoreline. Three days of lidar data belong in this

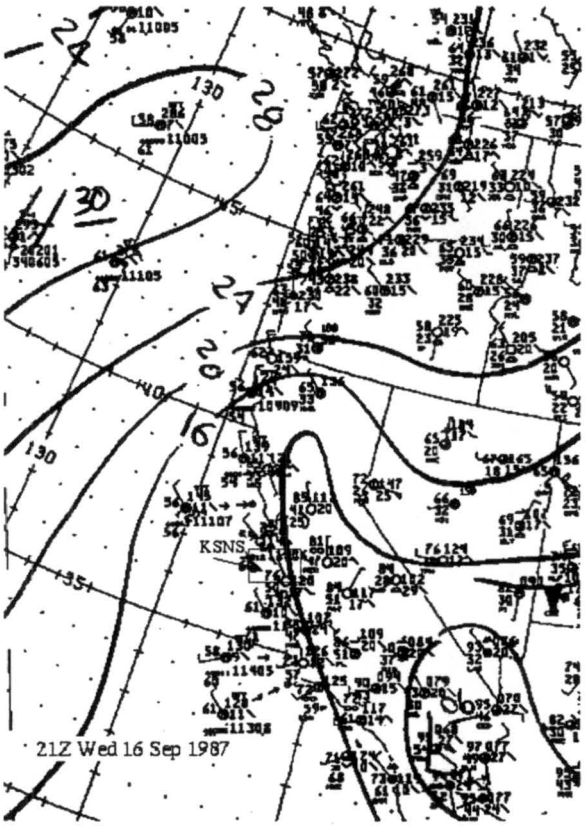

Figure 2.2b As in Fig. 2.2a, except for 2100 UTC, 16 September 1987.

category.

The different types of synoptic conditions which produce onshore or offshore flow are discussed in detail in Banta et al. (1993). Several features of the sea breeze flow were investigated within the context of these synoptic-flow categories. For instance, time of onset, wind speed, depth of onshore flow, the detection of a return flow, and the horizontal variability of the winds were all affected by the synoptic conditions in which the sea breeze flow was embedded.

September 16, 1987, classified as an abrupt day, was chosen for extensive analysis because the lidar operated from early morning into the night, capturing the transition from early morning offshore flow to onshore flow, the maturation of the sea

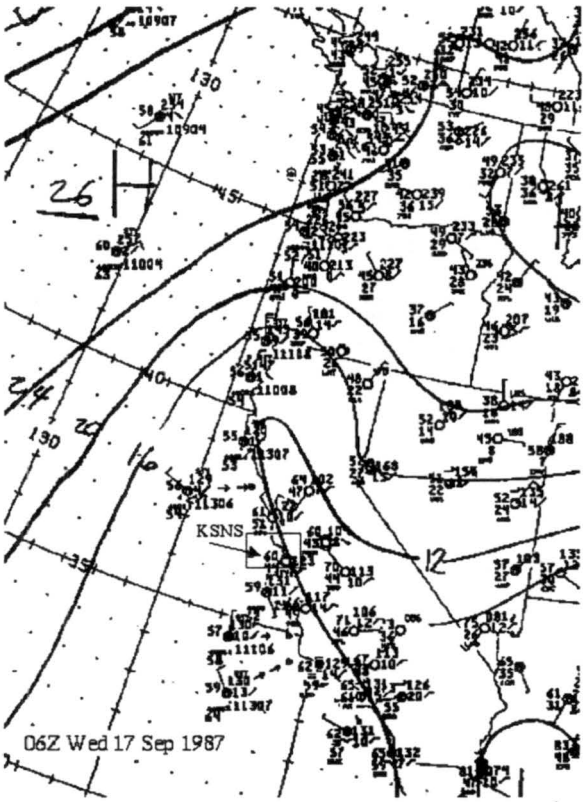

Figure 2.2c As in Fig. 2.2a, except for 0600 UTC, 17 September 1987.

breeze during the day, and the reversal back to offshore flow in the evening (as seen in the next sub-section). Surface synoptic maps for 16 September 1987 are shown in Fig. 2.2. The dominant synoptic features were a Pacific High west of Oregon and a thermal low in southern CA., causing an offshore pressure gradient along the west coast. Superimposed upon this pattern was a thermal trough along the interior valley of California that deepened throughout the day. Associated with the axis of the thermal trough were north-northwesterly winds along the coastline stations and north-northeasterly flow in the interior stations (the winds flowing toward the axis of the thermal trough). The presence of this thermal trough indicates a larger secondary scale of thermal forcing for the sea breeze as suggested by in Johnson and O'Brien (1973), and

Kimura and Kuwagata (1993). Local scale factors that influenced the winds included the land/water contrast at the shore, slope flows, and valley flows.

Morning offshore flow was seen at several coastal stations on the 1800 UTC map (1000 LST, Fig. 2.2a), with southeasterly flow from the Salinas River Valley as indicated by the Salinas Municipal Airport (KSNS) observation. Temperatures at KSNS and in the interior valley stations east of Monterey Bay were nearly the same. Between 1800 UTC and 2100 UTC (1000 and 1300 LST, Fig. 2.2b) the thermal trough became more pronounced, and the coastal stations were more likely to have an onshore component. This pattern maintained itself throughout the day. With the sea breeze in full swing, temperatures were much cooler along the coast than in the interior valley stations. Well after sunset, the thermal trough weakened, the temperature gradient across the coast weakened, and the winds at most stations also became weaker (0600 UTC (2200 LST), 17 September, Fig. 2.2c). The 50 kPA chart (not shown) indicated a trough with its axis east of the California coast, causing northwesterly flow aloft.

2.2.2.2 Lidar data

The first step in analyzing the lidar data was to peruse the radial velocity and backscatter data using color display software. Examples of color radial velocity plots are shown in Fig. 2.3 (backscatter plots will not be shown in this paper). Negative velocities (green and blue) indicate flow toward the lidar and positive velocities (orange and red) indicate flow away from the lidar, which is in the center of each plot. In Fig. 2.3a, taken at 0829 LST, 16 September 1987, at a 1° elevation angle, the offshore flow nearer the surface (measurements closest to the lidar) was from the southeast. These winds were

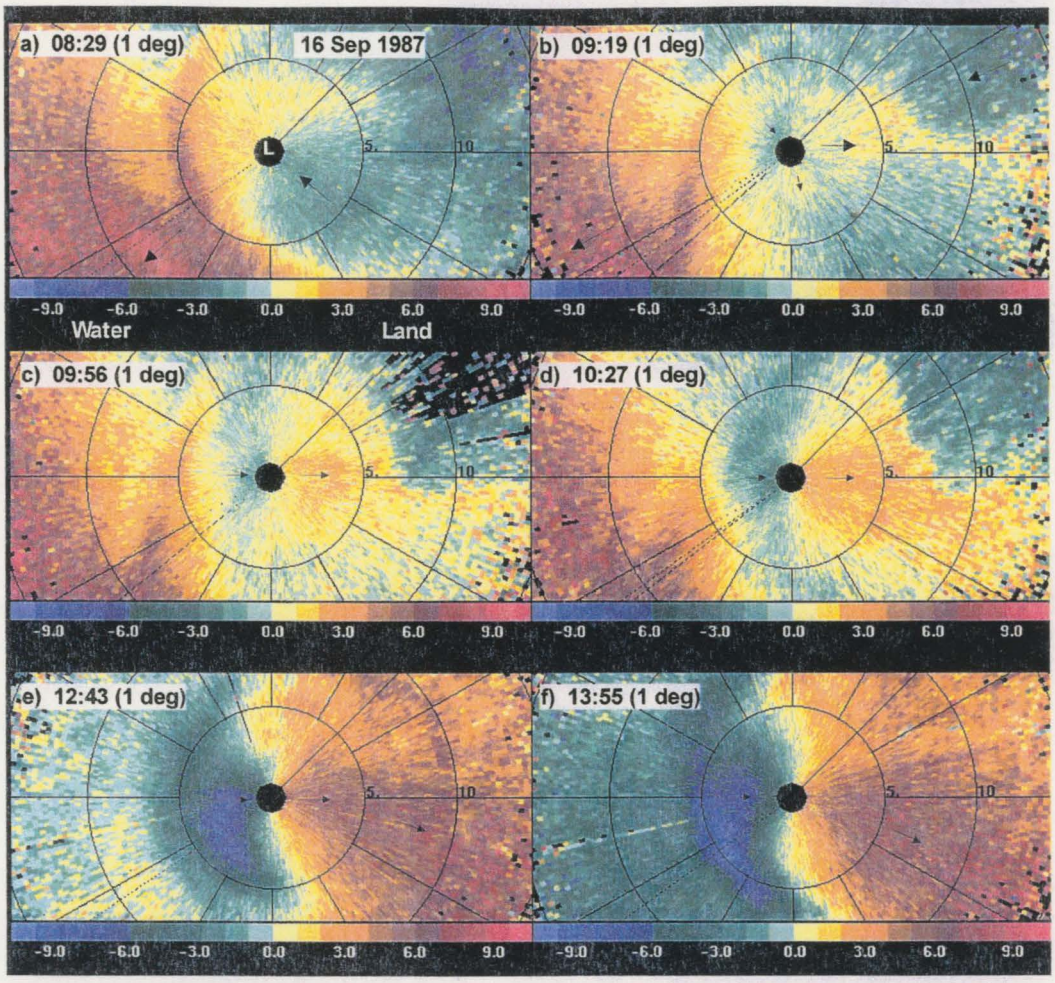

Figure 2.3 Doppler lidar constant-elevation-angle radial velocity scans showing the evolution of flow near the shore on 16 September 1987. The lidar (indicated by an L in the top left scan) is in the center of each scan and was located 1.5 km east of the shore. The lidar's minimum range was 1.5 km, so measurements on the left-hand side of each plot are over water, whereas measurements over the right-hand side are over land. Green and blue indicate flow toward the lidar, orange and red indicate flow away from the lidar. Range rings are 5 km apart. Wind speeds are in m s^{-1} (the white numbers under the color scale). Times are LST. Elevation angle is 1° above the horizon. Flows are described in text.

oriented along the direction of the Salinas River Valley (see Fig. 1.1a). Above this southeasterly flow (measurements farther away from the lidar), the flow was from the northeast. Higher elevation scans (not shown) indicated northwesterly flow above that, in

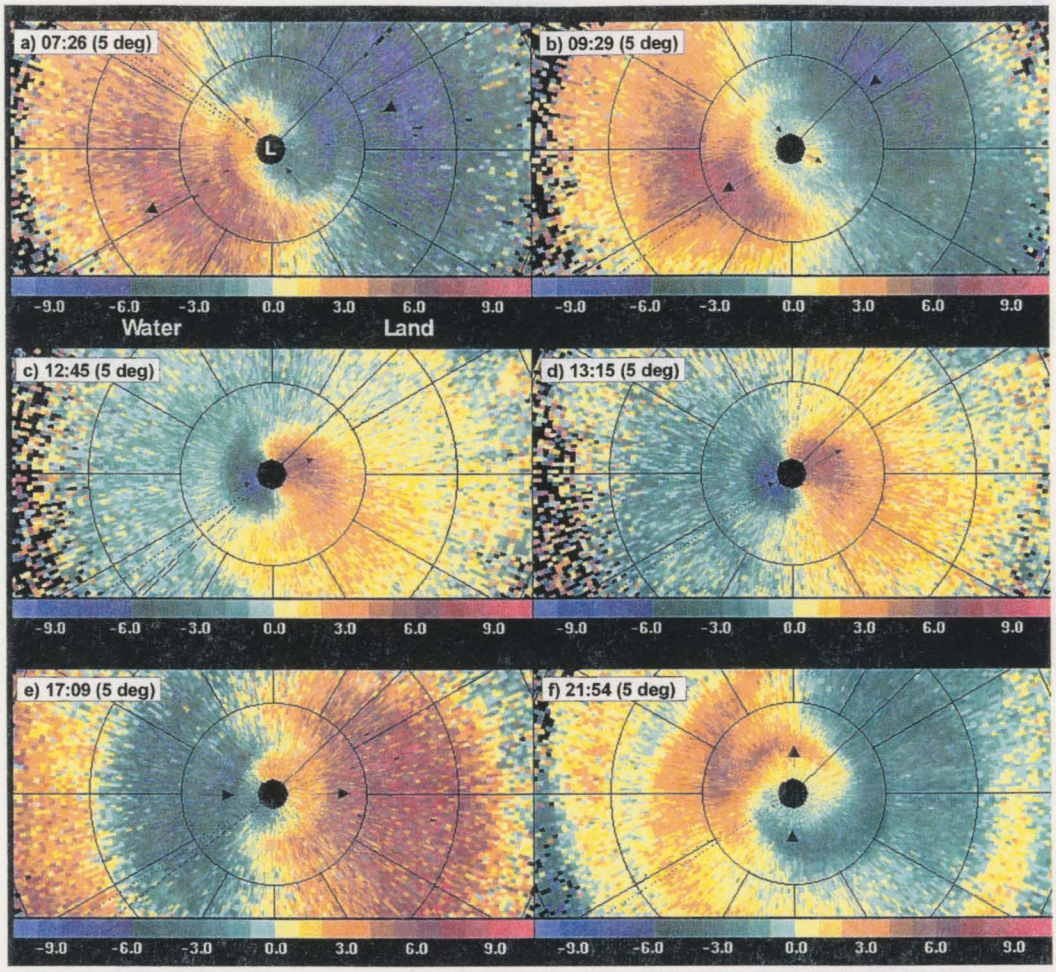

Figure 2.4 Same as in Fig. 2.3, except that the elevation angle was 5° above the horizon.

accordance with the upper-air analysis. Figure 2.3b shows a small region of onshore flow west of the lidar, the newly formed sea breeze. The offshore flow from the Salinas River Valley had weakened considerably and the sea breeze was starting to flow into the valley. In addition to this flow toward the southeast, the horizontal extent of the sea breeze flow was enhanced east of the lidar (the elongated region of westerly flow at ~90° azimuth), probably due to upslope flow generated by the nearby terrain. In Fig's 2.3c and 2.3d the sea breeze continued to strengthen and expand. Figure 2.3e shows strong onshore flow at

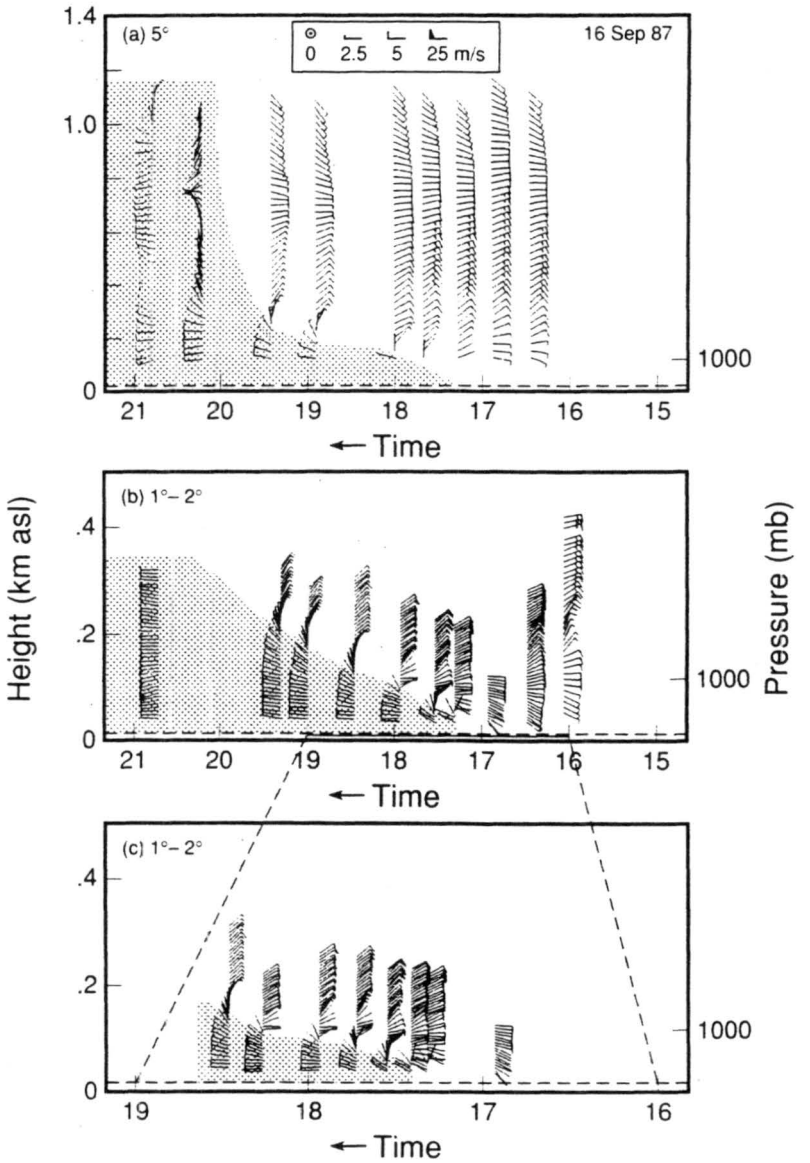

Figure 2.5 Profiles of the horizontal wind on 16 September derived from conical (PPI) lidar scans using the VAD procedure (from Banta et al. 1993). Time (UTC) is from right to left. Barbs point into the wind. Westerly flow, the sea breeze, is shaded. (a) Profiles from 5° PPIs. (b) Profiles from 1° and 2° PPIs. (c) Additional 1° and 2° profiles for the time period 1600 to 1900 UTC.

lower heights over water, with light and variable winds above (greater range from lidar), whereas the winds over the land were more uniform with height (distance). A mature sea breeze is shown in Fig. 2.3f. Note that the strongest flow over land in the bottom two plots was oriented along the Salinas River Valley. These lidar measurements show the complexity of the winds in the Monterey Bay region. The land/water contrast and the nearby terrain each played a role in the horizontal variability of the wind.

Fig. 2.4 shows a similar series of lidar scans, but the elevation angle was 5° above the horizon, thus providing more information about the winds higher above the ground than the 1° plots. At 0726 LST (Fig. 2.4a) the directional shift of the flow with height was very clear: southeasterly flow from the Salinas River Valley near the surface and east-northeasterly flow above that. The newly formed sea breeze was seen as a very weak westerly to north-westerly wind near the surface in Fig. 2.4b. Fig. 2.4c shows the two scales of sea breeze flow, stronger onshore flow at low levels, and weaker onshore flow above, as described in the introduction. The strengthening of the sea breeze over a half-hour's time is seen in the comparison of Fig. 2.4c and Fig. 2.4d. By 1709 LST (Fig. 2.4e), the two scales of flow had blended, and the wind near the surface was now south-southwesterly. A few hours later, in the evening (Fig. 2.4f), the flow at the surface still had a southerly component, but the flow above this layer had switched to offshore.

Another technique for displaying constant-elevation-angle lidar scans is the Velocity-Azimuth Display (VAD) technique described by Browning and Wexler (1968). With this technique, vertical profiles of the horizontal wind can be calculated. An example of this type of analyses is shown in Fig. 2.5 (Fig. 12 in Banta et al. 1993). Note

that times are in Universal Time Coordinates (UTC = LST + 8 hr). The plot shows the evolution of the offshore easterly flow to onshore westerly flow (shaded) as calculated from lidar scans with constant elevation angles of 5° (upper panel) and 1° or 2° (lower two panels). The morning offshore flow, at least 1 km deep, was too deep and strong to be a land breeze. The synoptic situation dictated offshore flow.

Figure 2.6 is a 6-panel figure of constant-azimuth vertical-slice scans showing the evolution of the vertical structure of the sea breeze along a line perpendicular to the coast on 16 September 1987. Again, negative (blue/green) velocities indicate flow toward the lidar, and red and orange indicate flow away from the lidar. In Fig. 2.6a, the early morning offshore flow was ~1.5 km deep. The flow above this layer had a westerly component. Almost 2 hr later, at 0949 LST, a very shallow (< 200 m) sea breeze, indicated by the white arrows in Fig. 2.6b, had formed underneath the morning offshore flow. The landward extent of the onshore flow was much greater than the seaward extent, as seen in the constant elevation angle scans in Fig. 2.3. The two scales of sea breeze were evident at 1226 LST (Fig. 2.6c). A shallow (<400 m deep) layer of onshore flow was several m s^{-1} stronger than the weaker onshore flow developing between 400 m and ~1000 m. The sea breeze was deeper over land than over water, and the winds were stronger over the water surface, indicating an asymmetry in the sea breeze development. The stronger winds are probably due to less surface roughness over the water than over the land, and a deeper boundary layer over the warmer land surface would allow a deeper layer of onshore flow to form. Traces of the early morning offshore flow existed above the sea breeze.

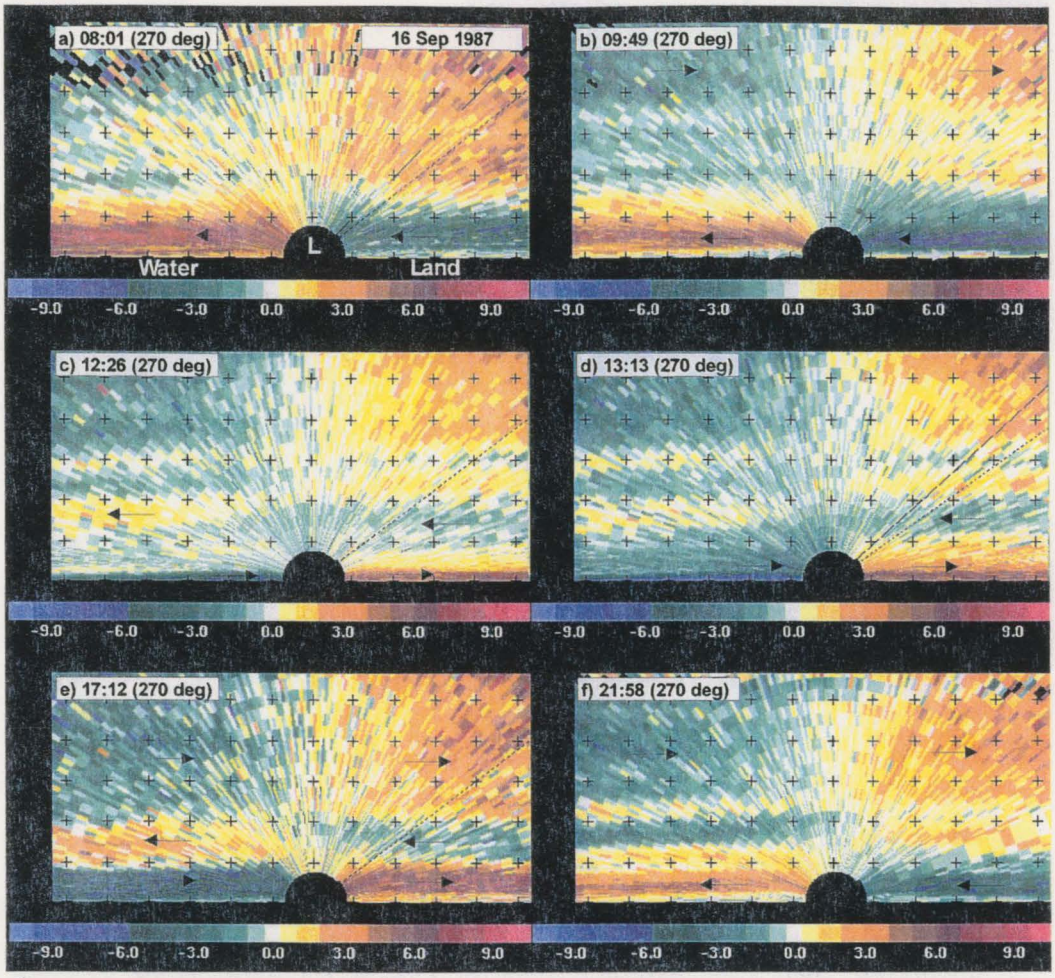

Figure 2.6 Doppler lidar east-west constant-azimuth-angle radial velocity scans for 16 September 1987. The location of the lidar is indicated by an L in the top left-hand plot. As in the constant-elevation-angle plot, measurements to the left of the lidar are over water, measurements to the right of the lidar are over land. Green and blue indicate flow toward the lidar, orange and red indicate flow away from the lidar. The vertical axis is height above the lidar, and the horizontal axis is distance from the lidar (tick marks 1 km apart). Flows are described in the text.

In Fig. 2.6d the onshore flow was at least 6 m s^{-1} from the surface to 500 m AGL. Over water the sea breeze flow deepened near the shore, and the winds over the water's surface continued to be stronger than the winds over the land. A mature sea breeze 1 km deep was seen in Fig. 2.6e, 1712 LST, with a layer of offshore flow above it, also 1 km

deep. The westerly component of the synoptic-scale upper-level northwesterly flow was seen above that (as in the previous plots). The evening offshore flow was established by 2200 LST, as shown in the final panel of the figure (Fig. 2.6f), taken several hours after the scan shown in Fig. 2.6e. The complexity of the winds shown in the constant elevation scans (Fig. 2.3 and 2.4) clearly demonstrate that these vertical east-west scans cannot possibly tell the whole story of the sea breeze flow, but they are a very good starting place for investigating the vertical structure of the sea breeze at Monterey Bay.

Figure 2.7 shows the process for the final step in assessing the vertical structure of the sea breeze using the east-west cross-sections. Radial velocity data from all east-west RHIs like the one in the top plot were transformed from polar coordinates to Cartesian coordinates (Fig. 2.7b). Then, for each scan, a horizontal average of the u-component of the wind from x = - 4 to -1.5 (i.e., just offshore) was calculated at the height of each vertical grid point (vertical grid spacing was 25 m). Thirty-one of these profiles through RHIs taken on 16 September were compiled into the time-height plot shown in the bottom panel of the figure. Similar time-height plots were created from the sea breezes modeled with RAMS, and are shown in Section 4. The comparisons between this lidar plot and the model time-height plots will be used to assess the model's success in capturing the vertical structure of the Monterey Bay sea breeze, therefore it is important to review here the features of interest in the lidar plot.

In the morning hours (0700 to 1000 LST) the offshore flow was at least 1.5 km deep, as seen in the color plots (Fig. 2.6), with a maximum speed of 7 m s^{-1} just before 0800 LST. Above this offshore flow was a weak layer of westerly flow. The reversal

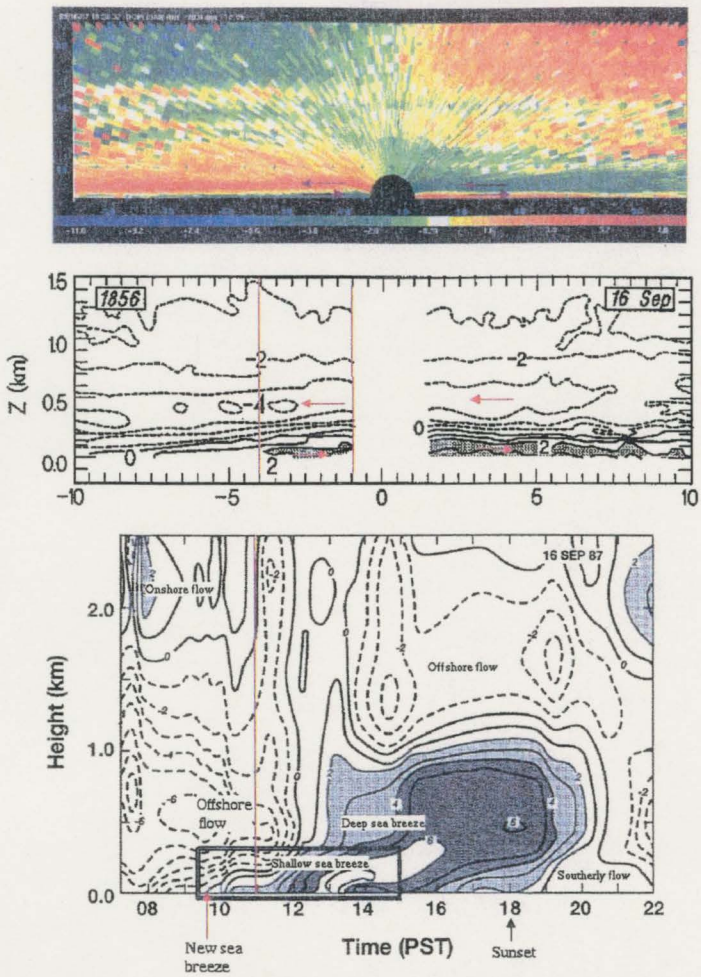

Figure 2.7 Plots illustrating the process of converting east-west cross sections of radial velocity to time-height profiles of the *u*-component of the wind. (Top) Color plot of lidar radial velocity scan perpendicular to the shore. Interpret as in Fig. 2.6. (Middle) Lidar radial velocity measurements converted to Cartesian coordinates from polar coordinates. In the conversion process, radial velocities were divided by the cosine of the elevation angle, giving the *u*-component of the wind. Measurements between the vertical red lines were averaged horizontally at each vertical grid point to produce a single profile of the *u*-component of the wind with height. (Bottom) Profiles from 31 east-west cross-section scans were compiled into this figure. The red vertical line indicates the location of the profile derived from the middle figure.

from offshore to onshore flow was first indicated at the surface at 0930 LST. The onshore flow layer was quite shallow (< 300 m) for the first hour, then rapidly increased in depth at 1200 LST. Two scales of flow, the shallow, stronger sea breeze imbedded in a weaker, deeper sea breeze, were evident until 1500 LST. Finally, the mature, blended sea breeze stage was evident for more than 4 hr starting at ~1500 LST. The apparent weakening of the wind below 500 m between 1800 and 2000 LST was actually a gradual backing of the wind from westerly to southerly, as seen in the PPI color plots, so the radial component of the wind approached zero in the east-west cross-sections. Near 2200 LST, the reversal from onshore to offshore flow began.

Model results shown in sections 4 and 5 reproduce the features seen in Fig. 2.7, some more successfully than others. Sensitivity simulations and factor separation results lend insight on possible reasons why the dual structure of the sea breeze was present and why there was not an obvious compensating return flow.

Chapter 3

Nonlinear modeling of the sea-breeze circulation

3.1 Previous modeling studies

3.1.1 Early development of nonlinear sea breeze models

Early nonlinear sea-breeze models were usually two-dimensional, until the 1970's when McPherson (1970) and Pielke developed 3-dimensional models (Pielke 1973, 1974). Typically one side of the domain was land and the other side water. The sea breeze was treated as a perturbation flow within the larger-scale flow. The models were based on the equations of momentum, heat, and mass continuity, with velocity, temperature, and pressure the forecast meteorological variables. Model features that improved over the last three decades include domain size and grid spacing, lateral and upper boundary conditions, and turbulent diffusion parameterization. Early 2-dimensional models only had a few hundred grid points, usually with finer resolution near the shoreline than near the lateral boundaries. Vertical grid points were more closely spaced near the surface than at the top of the domain. As computer power increased, it became possible to increase the domain size and decrease the grid spacing. The treatment of turbulent diffusion was more challenging, however. Progress in the turbulent diffusion problem involved advances in theory and numerical methods rather than advances in computing power.

Pearce (1955) published a seminal paper regarding a numerical method for evaluating a system of nonlinear equations to predict the vertical structure of winds, atmospheric pressure and temperature associated with the sea breeze. He divides the wind into two scales of flow, the tidal motion and the sea breeze. The tidal motion has small velocities and 'continental dimensions.' It is governed by linear equations, therefore ignoring the effects of advection. The sea-breeze flow has velocities greater in magnitude than the tidal motion, and affects a smaller region near the shore. Since the sea breeze modifies the environment in which it develops, the advection terms are necessary to accurately describe the evolution of the sea breeze life cycle. Pearce implements his new numerical method in order to allow a system of nonlinear equations to govern the sea-breeze flow. An artificial heat source over the land is imposed as a function of time onto an atmosphere that is initially at rest and isothermal. The land surface temperature attains a maximum, then remains constant. In the sea breeze region of the model, advection and convection currents transport the heat added to the domain by the land surface. Well inland, away from the influence of the sea breeze, $\partial \square / \partial t = 0$. Pearce uses the admittedly 'crude but convenient' assumption of no surface drag.

Fisher (1961) and Estoque (1961) build on Pearce's work. A notable difference between Fisher's model and Estoque's model is that Fisher uses the vertical component of the equation of motion while Estoque uses the vertical derivative of the continuity equation, in conjunction with the hydrostatic equation. Fisher (1961) adds 1) a land heating mechanism based on sea breeze observational studies, while the temperature over the water remains constant, 2) the transfer of heat from the ground to the atmosphere

through turbulent processes as computed from a heat-diffusion equation, 3) a heat sink (or cooling), and 4) surface frictional drag. Sensitivity studies performed by Fisher include withdrawing internal and surface friction, and varying the upper boundary conditions. For the first 8 hours or so of Fisher's simulation, the vertical structure of the sea breeze circulation looks reasonable. However, the vertical velocity values grow unsteadily in the upper levels of the domain. With time these bad values migrate downward through the domain, producing 'computational waves' and unrealistic vertical structure. Fisher postulates that the logarithmic vertical grid system produced errors in the u-component of the wind, resulting in poor estimates of w.

Estoque (1961) divides the domain into two layers, a constant flux sublayer and an upper sublayer. The constant flux sublayer is a relatively thin surface layer and the vertical momentum and heat eddy fluxes are constant with height in this layer. Eddy diffusivities are calculated using one of two schemes based on the Richardson number (free convection or forced convection), and decrease linearly with height. Values across the upper sublayer range from the constant flux sublayer value at the bottom to zero at the top. The model calculations for winds, pressure and temperature occur in the upper sublayer, where momentum and sensible heat fluxes are determined from existing fields in the model. For computational stability (in lieu of small time steps), Estoque uses the vertical derivative of the continuity equation, with the hydrostatic approximation. This suppresses gravity waves, but ultimately leads to a violation of mass conservation. [Neumann and Mahrer (1971) show the unrealistically large values of divergence produced near the shoreline when using Estoque's equations.] While the initial winds are

generally at rest in these early nonlinear models, Estoque (1962) performs sensitivity studies by varying the initial winds. He initializes his model with winds that are zero, offshore, onshore, and parallel to the shore. He also varies the surface pressure during parallel wind cases, and varies lapse rates with the zero initial wind cases. Overall, Estoque's results are encouraging, with the evolution of the sea-breeze flow and the vertical structure of temperatures closely resembling sea breeze observations.

After Estoque's early work, several modeling papers based on his model appeared in the literature. Each author added increasingly more sophisticated elements to the domain, boundary conditions and computations. Moroz (1967) uses Estoque's equations and techniques (1961, 1962) to investigate a lake breeze. The main difference between his version of the model and Estoque's is that there is land on both sides of the domain, with water in the middle, rather than land on one side and water on the other. This domain is symmetric, with a centerline boundary that the horizontal wind cannot cross. His model becomes unstable after ~8 hr, possibly due to the boundary condition of $u = 0$ at the centerline.

McPherson (1970) designed a three-dimensional model based on Estoque's equations. Rather than a straight coastline, there is a square bay in the domain. In the upper sublayer, or transition layer in McPherson's model, the eddy diffusivities decrease exponentially with height rather than linearly. This exponential decrease, along with smaller grid spacing in the horizontal, leads to larger modeled vertical velocity values than seen in previous studies. Given that this is the first three-dimensional sea-breeze model, McPherson's paper focuses on the horizontal structure of the modeled sea breeze.

Notable results attained from the simulation presented include 1) divergence over the bay due to the onshore winds early in the simulation; 2) the strengthening of the onshore flow with time; 3) the veering of the wind direction over the bay due to Coriolis; and 4) convergence zones associated with the onshore flow are influenced by the shape of the bay. This type of information would obviously not be available from a two-dimensional model. Pielke (1974) points out that McPherson's difference scheme is linearly unstable and the model needs 'excessive explicit diffusion' to remain stable.

Neumann and Mahrer (1971) continued to build on Estoque's work. However, by dimensional analysis they show that the accelerational term for the vertical component of motion is large enough that it cannot be neglected as Estoque had. By dropping the hydrostatic assumption, using a modified pressure term, assuming density is constant with height (since the sea breeze is a shallow feature) and changing the pressure disturbance boundary conditions, they were able to use the continuity equation in its usual form rather than the vertical derivative. Neumann and Mahrer's analysis focuses on the land breeze portion of the land/sea breeze cycle.

Pielke (1974) addresses many deficiencies in the previous models by developing a new hydrostatic three-dimensional model. For the grid spacing used, Pielke determined that the incompressible and hydrostatic forms of the equations would be acceptable, and adds a conservative continuity equation for water vapor. Rather than using a rigid lid, as in the previously referenced works, Pielke adds a material surface at the top of the domain. This material surface responds to the addition of heat to a column of air, i.e., the column expands with the addition of heat. While the previous authors used a prescribed

height for the surface and boundary layers, Pielke's model determined the height of these layers as a function of wind stress, u_*. Pielke also introduces a detailed subgrid-scale parameterization scheme for obtaining values for exchange coefficients. The vertical exchange coefficients are calculated for three layers: 1) surface layer, 2) planetary boundary layer, and 3) above the planetary boundary layer, and are calculated independently for land and water. The horizontal exchange coefficients are calculated independently from the vertical exchange coefficients due to the difference in horizontal and vertical grid spacing and are used only for smoothing. Other additions to Pielke's model include a staggered grid and different roughness values for land and water. Results suggest that there is an increase in the turbulent transfer of heat due to the different roughnesses. The staggered grid, with $\tilde{w}$ at the half-grid point in the horizontal, leads to smoother solutions near the lateral boundaries.

Included in Pielke's 1974 paper are sensitivity studies. He compares the development of the south Florida sea breeze and convection under southwest synoptic flow vs. southeast synoptic flow on synoptically quiescent days, and the removal of Lake Okeechobee vs. its presence. He also compares model results to radar returns for general convective features and for a particular case study. Pictures taken from spacecraft, when compared to model results, show similarities in the general convergence patterns and divergence over Lake Okeechobee. The curvature of the coast enhanced the modeled convergence zones. These convergence zones coincided with typical patterns of afternoon thunderstorms in south Florida for the given synoptic flow.

Physick (1976) was the first to include an equation to predict surface temperatures

using feedback between the surface and the atmosphere. The vertical exchange coefficient for momentum, K_m, is 'specified as a nonlinear function of stability and wind shear at all levels.' Through a heat balance equation the surface temperature is calculated. Physick ran simulations of a land-locked body of water, at the time a natural transition between 2-D and 3-D modeling of the sea breeze. Simulating the breezes formed by two lakes of different sizes, he found that with a wider lake there was more area to distribute heat, forming a greater temperature gradient between land and water, resulting in stronger breezes.

Arritt (1989) investigated the offshore extent of the sea breeze with another nonlinear model. He varied the water temperature, thus varying the stratification of the air mass near the surface. The most important effect was when the water temperature created an unstable stratification, which eroded the sea breeze. Varying the ambient wind showed a strong effect on the offshore extent, with onshore ambient flow reducing the seaward extent of the sea breeze circulation.

3.1.2 Mesoscale model sensitivity studies investigating the land/water contrast and terrain effects

Mahrer and Pielke (1977) were the first to present model comparisons of the sea breeze, slope flows, and the combination of both. They used idealized cases designed to investigate the differences among these types of simulation. Mahrer and Pielke concluded from their results that the combined sea breeze and slope flow was stronger than either flow separately. Ookouchi et al. (1978) continued with 2-D idealized case studies, comparing a no mountain case, a thermally insulated mountain case (the slopes

did not heat or cool), and a heated mountain case, all with water in the western portion of the domain. They found that the greatest sea-breeze inland penetrations occurred with the insulated mountain case. The strongest land breeze occurred with the heated-mountain case because of the strong downslope winds that formed (the insulated mountain case had no downslope winds due to a lack of cooling on the slopes). Their strongest sea-breeze flow was seen in the no mountain case, which agrees with our results shown in sections 4 and 5.

Kondo (1990) investigated the interaction between flows generated by a land/sea contrast, a sloping plateau adjoining a plain, and the combination of the two, using 2- and 3-D numerical modeling. In the 2-D simulations Kondo found that the slope flow enhanced the sea-breeze flow in the morning and opposed it in the afternoon. Kondo also investigated the relationship between the height of the plateau and the depth of the mixed layer, finding that if the height of the plateau was less than the height of the mixed layer, the winds were as deep as the mixed layer. If the height of the plateau was greater than the mixed layer, the winds were deeper than the mixed layer. The results shown in Kondo's Fig. 2 show slightly weaker sea-breeze return flow if the inland sloping plateau was present, similar to our result of a weaker or non-existent return flow if the inland mountain was present (section 4).

Doyle's (1997) modeling study of a coastal jet and rainband along the California coast used a 3-D model to perform a control simulation (terrain as is), a no terrain simulation, and a simulation with the coastline displaced 100 km westward to investigate the effect of the increased surface roughness of land over water. In the control run the

near-surface coastal jet was 45% stronger than the no topography case (in agreement with Cui et al. (1998)), due to the lack of blocking effects of the terrain.

Other studies relevant to the present investigation are Cui et al. (1998) and Lu and Turco (1994). These studies are described in conjunction with the results of the present study in Section 4.1.

3.2 The Regional Atmospheric Modeling System (RAMS)

3.2.1 RAMS Overview

The Regional Atmospheric Modeling System (RAMS), based in part on Pielke's sea breeze model discussed in the previous section, has evolved into a sophisticated atmospheric model that can handle a wide range of meteorological scales. The non-hydrostatic Reynold's-averaged primitive equations for momentum, thermodynamic energy, water species mixing ratio, and mass continuity are solved in two or three dimensions. Simulations can be performed on a single staggered grid, or on an arrangement of nested staggered grids, with each grid capable of having finer resolution than its parent grid in the horizontal and vertical. The nested grids are two-way interactive and can move with a weather system. The specification of vegetation, soil type, and soil moisture allow for appropriate surface sub-grid-scale parameterizations to be used. Terrain heights can be interpolated to the model grids and the vertical coordinate system is the σ_z terrain-following coordinate system. The model has several choices of lateral and vertical boundary conditions and two choices for longwave and shortwave radiation schemes, each one with or without clouds. A simulation can be initialized with a single sounding or by interpolating a 3-D upper-air data set, surface

observations, and soundings to the coarsest grid, with subsequent interpolation to nested grids. Four-dimensional data assimilation (4DDA) with nudging has been incorporated into the model. All of these features, and more, are described in detail in Tremback and Walko (1994).

Numerous types of meteorological events that have been simulated with RAMS appear in the literature. Some of the more recent papers include simulations of coastally trapped disturbances in Australia (Reason et al. 1999) and the west coast of North America (Guan et al. 1998; Jackson et al. 1999), a sensitivity study of anthropogenic landscape changes in south Florida, (Pielke et al. 1999), simulations of local-scale pollution dispersion in Athens, Greece (Kotroni et al. 1999), and real-time forecasting for the 1996 summer Olympics in Atlanta, Georgia (Snook et al. 1998). This short list points to the immense flexibility of RAMS. For the coastally trapped disturbance and the pollution dispersion simulations, complex terrain features needed to be adequately represented in the model domain. Sophisticated surface parameterization schemes to account for the variable vegetation in the land use sensitivity simulations were necessary for the successful results in Pielke et al. (1999). Snook et al. (1998) show that a research-grade mesoscale model can function well in a real-time mode with adequate initialization and setup.

3.2.2 Model Setup

All of the simulations shown in this paper are two dimensional (2-D). The dotted line in Fig. 3.1 represents the domain, an east-west cross section through the center of Monterey Bay at the same latitude as the lidar deployment at Moss Landing. The western

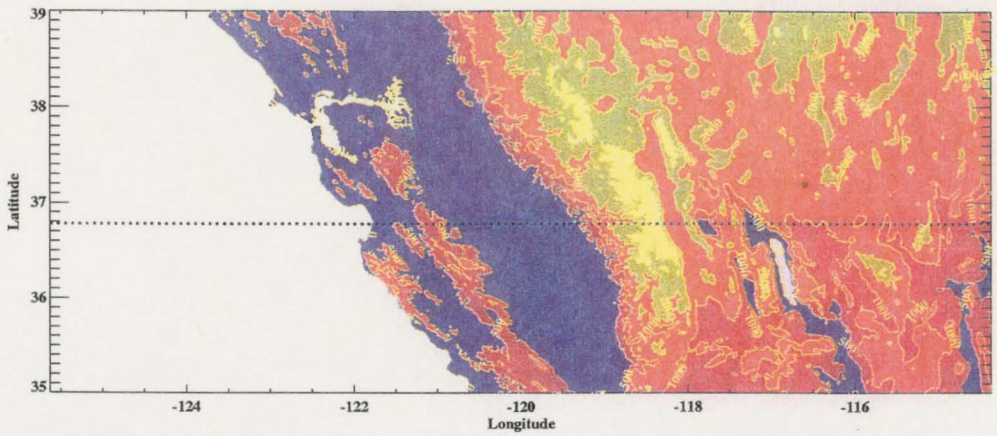

Figure 3.1 Terrain map showing the vast changes in topography across the modeling domain. The dotted horizontal line indicates the location of the 2-D domain used in the simulations presented in this paper.

third of the domain extended over Monterey Bay and the Pacific Ocean. A constant sea surface temperature of 15° C, determined from the monthly average for September 1987, was assigned to the water portion of the domain.

To ascertain how the mountain ranges east of Monterey Bay affect the sea breeze, it was necessary to include the Sierra Nevada mountain range. Cui et al. (1998) found that the inclusion of the Sierra Nevada range was needed to realistically model the winds near the shore along the California coast, including the Monterey Bay region. In their 2-D simulations, the presence or absence of the Sierra Nevada range strongly influenced the *along-shore* component of flow. We will show that the Sierra Nevada range greatly affects the across-shore winds at Monterey Bay, both at the surface and above the sea-breeze layer. According to Avissar et al. (1990), the needed domain size and grid spacing for mesoscale numerical modeling of sea- and land-breezes with homogeneous initialization are at least as large as 1000 km and as small as 20 km, respectively. In our

case, the east-west domain size was 1000 km, large enough to extend beyond the bay and the Sierras, and falling within the limits of what Avissar et al. suggest. The simulations were designed to have high vertical resolution because the focus of this study is the vertical structure of the sea breeze. The vertical grid spacing from the surface to 1.0 km AGL was 25 m. The grid spacing then increased very gradually with height, never exceeding 500 m. A total of 90 grid points in the vertical featured one-half the grid points in the lowest 1.2 km AGL. The domain height was 15 km. Because of the steep slope of the Sierra Nevada range directly east of Monterey Bay, and the desire for high vertical resolution, it was necessary to have a relatively small horizontal grid spacing, Δx = 2 km, for the single-grid domain.

A modified morning sounding launched from the R/V Silver Prince on 16 September 1987 was used for the homogeneous initialization. A strong marine inversion was represented in the sounding, as is typical of the region. Since this profile only extended to 7 km AGL, the 16 September 1987 morning rawinsonde from Oakland, CA., filled out the sounding to the top of the domain. Winds below 5 km ASL in the initial sounding were easterly at 1 m s^{-1}, backing to westerly by 6.5 km ASL. The simulations, which began at 1200 UTC 15 September, were run for 42 hours to allow the model to complete one diurnal cycle before being analyzed, as is recommended in Avissar et al. (1990) and Cui et al. (1998) when the domain is large and homogeneous initialization is used.

The Coriolis parameter was turned off in the model simulations, yielding true 2-dimensional simulations, because of the steepness of the terrain. When the Coriolis

parameter was activated, the model became unstable in the afternoon when the sea breeze became established and the winds became supergeostrophic, resulting in an acceleration of the winds out of the model domain (i.e., to the north or south). A 2-D model is unable to have cross-domain pressure gradient force feedback when complex terrain is present. The remainder of model parameters not discussed thus far are shown in Table 3.1.

Table 3.1 RAMS options used in the simulations shown in sections 4 and 5

Time step	4 s
Grid origin	Longitude = -120.00°, Latitude = 36.78°
Topography	Idealized or 30 s elevation data
Vegetation	Specified or satellite derived data set
Microphysics	Dry
Time differencing scheme	Hybrid:
Top boundary condition	wall
Lateral boundary condition	Klemp/Wilhelmson
Large-scale gradient	zero gradient inflow and outflow
Shortwave radiation scheme	Mahrer/Pielke
Longwave radiation scheme	Mahrer/Pielke

Table 3.2 shows the various types of simulation used for the sensitivity studies of topography, land/water contrast, and vegetation class. The first group of simulations, 1-5, comprises the terrain sensitivity set with a land/water contrast included in the domain. The only change in the model input among these simulations was the shape of the terrain. Figure 3.2 schematically shows the different terrain configurations. In simulation 1 the

Table 3.2 Simulation numbers with corresponding terrain configuration and vegetation.

Simulation	**Terrain**	**Vegetation**
Terrain sensitivity with land/water contrast		
1	Smoothed terrain	short grass
2	Inland Mtn and Coastal Mtn	short grass
3	Coastal Mtn	short grass
4	Inland Mtn	short grass
5	Flat terrain	short grass
Terrain sensitivity without land/water contrast		
6	Smoothed terrain	short grass
7	Inland Mtn and Coastal Mtn	short grass
8	Coastal Mtn	short grass
9	Inland Mtn	short grass
10	Flat terrain	short grass
Vegetation sensitivity with land/water contrast		
2	Smoothed terrain	short grass
11	Smoothed terrain	evergreen needleleaf
12	Smoothed terrain	satellite derived

terrain was read from a 30-sec terrain data set, interpolated to the model grid and smoothed (Fig. 3.2a). An even smoother version of the terrain was implemented in simulations 2 - 4 (Figures 3.2b - 3.2d). The coastal mountain represented the Gabilan and Diablo Ranges (see map, Fig. 1.1a) and the inland mountain, peaking 310 km east of the shore, represented the Sierra Nevada Range. Simulation 2 had the smoother version of

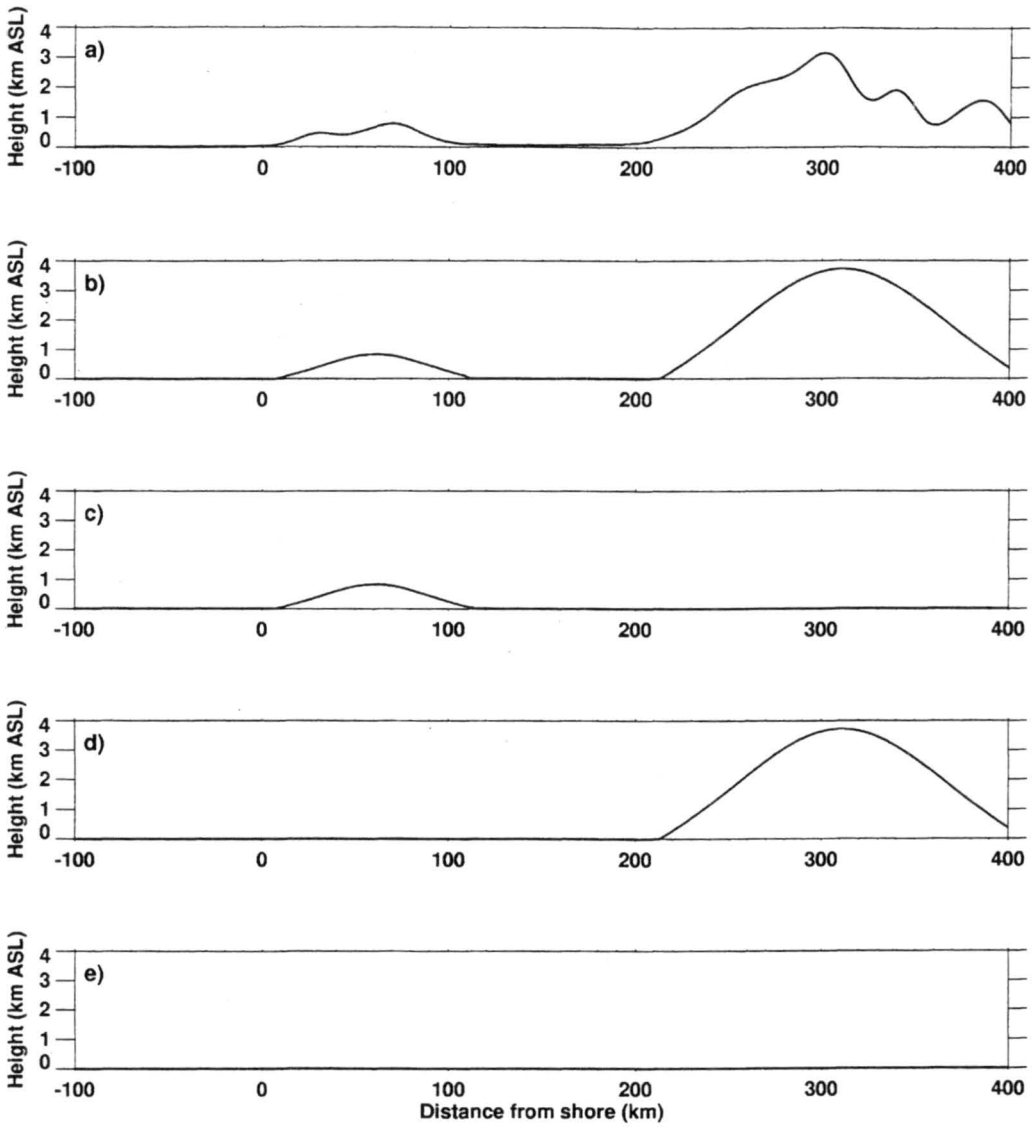

Figure 3.2 The terrain profiles used in the model sensitivity studies. Only the part of the domain immediately surrounding the terrain is shown. (a) Smoothed realistic terrain. (b) Idealized dual-mountain. (c) Idealized coastal mountain. (d) Idealized inland mountain. (e) Flat terrain.

both mountains, simulation 3 included only the coastal mountain, and simulation 4 included only the inland mountain. Simulation 5 had only flat terrain (Fig. 3.2e). In this group of simulations the western 325 km of the domain was water and the remaining portion of the domain was land. The vegetation class was short grass for all land grid

points.

In the second group of simulations, 6-10, the entire domain consisted of land grid points (i.e., no water in the domain) with a vegetation classification of short grass. The same five terrain variations used in the first group were also used here. The water was eliminated to isolate the effects of the slope flows from the sea breeze flow.

The last simulations, 11 and 12, tested the effects of different vegetation types, and used the smoothed 30-sec terrain data set. Only the vegetation was varied between these two simulations. In simulation 11, the vegetation classification was evergreen needleleaf. Simulation 2 also falls into this vegetation sensitivity group, since it includes the smoothed terrain and water. The needleleaf evergreen in simulation 11 provided a contrast to the short grass used in simulation 2. In simulation 12 the vegetation classes were based on the AVHRR satellite data set.

Chapter 4

Results

4.1 West-east cross sections

Figures 4.1 - 4.5 show west-east (left-right) cross sections of contours of the *u*-component of the wind for simulations 1-5. Note that only the region of most interest has been plotted; the domain extended another 300 km east and 250 km west of the region shown and the domain height was 15 km. This section presents the results of these simulations, showing vast differences in the vertical structure of the sea breeze and slope flows when the terrain was varied. The next section (4.2) gives analyses and comparisons with the lidar data using time-height cross sections.

The simulation with smoothed terrain is shown in Fig. 4.1. In the earliest plot shown, 0800 LST (Fig. 4.1a), both mountains had a shallow layer of downslope flow, most easily identified as the thin, blue layer attached to the western slopes of both mountain ranges. The noise in the contours west of the steep terrain of the inland mountain, 2-3 km ASL, disappeared as the land surface heated during the day. The combination of a stable layer at the surface that suppressed vertical mixing, steep terrain, and high vertical resolution was responsible for the noise. The shore is near x = 0 km, so when the contours switch to positive (solid) in this region, the combined sea breeze/slope flow is in progress. By 1000 LST (Fig. 4.1b) the sea breeze and upslope flows had

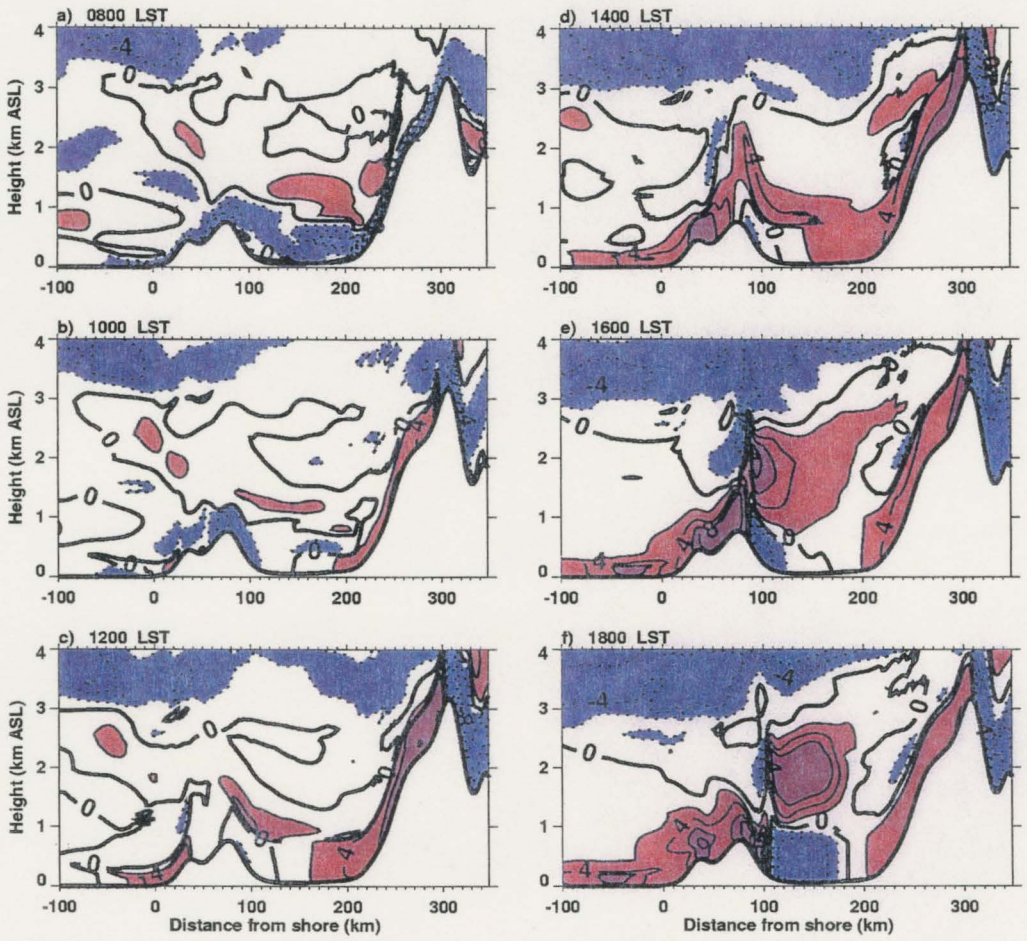

Figure 4.1 West-east cross sections of the modeled *u*-component of the wind (in m s^{-1}). Plots are every 2 hours from 0800 to 1800 LST for the smoothed terrain case. Solid (positive) contours indicate westerly flow, and increment every 2 m s^{-1}. Speeds greater than 2 m s^{-1} are shaded red. Dashed (negative) contours indicate easterly flow, also incrementing every 2 m s^{-1}. Speeds with magnitude greater than 2 m s^{-1} are shaded blue. The shore lies at x = 0 km, with water filling the domain west (left) of the shore.

started, now identified as the shallow red layer on the western slopes, and the blue layer on the eastern slopes. Over the course of the day, as demonstrated in the rest of the plots in this figure, the upslope flow/sea breeze grew in both the horizontal and vertical dimensions. By 1400 LST (Fig. 4.1d) a well-defined solenoidal flow structure had developed for each mountain range: upslope flow on both sides of each mountain with a compensating return flow. However, the return flow for the westward slope of each mountain range was quite weak. The convergence zone associated with the sea breeze crossed the crest of the coastal mountain by 1600 LST (Fig. 4.1e).

In the idealized-terrain simulation with both mountain ranges (Fig. 4.2) the terrain was slightly steeper than in the smoothed terrain case, so the fluctuations were stronger, giving the appearance of more noise along the slope of the inland mountain range in the early morning. Also, because of the steeper slopes, the downslope winds were stronger in this simulation relative to the smoothed terrain case. Since the sea breeze developed under a stronger downslope flow than in the smoothed terrain case, it initially appeared that the sea breeze had a well-defined return flow (1200 LST, Fig. 4.2c). With time, however, this easterly flow was eroded away. Overall, the vertical structure of the sea breeze was similar to the previous case shown, making this terrain setup suitable for sensitivity studies, such as comparing the differences in the winds at the shore with the coastal mountain only and inland mountain only cases.

With only the coastal mountain in the domain (Fig. 4.3), the main wind feature of the morning was a very shallow slope flow that was much more well-defined and stronger on the landward side of the mountain. In fact, this downslope flow on each slope of the

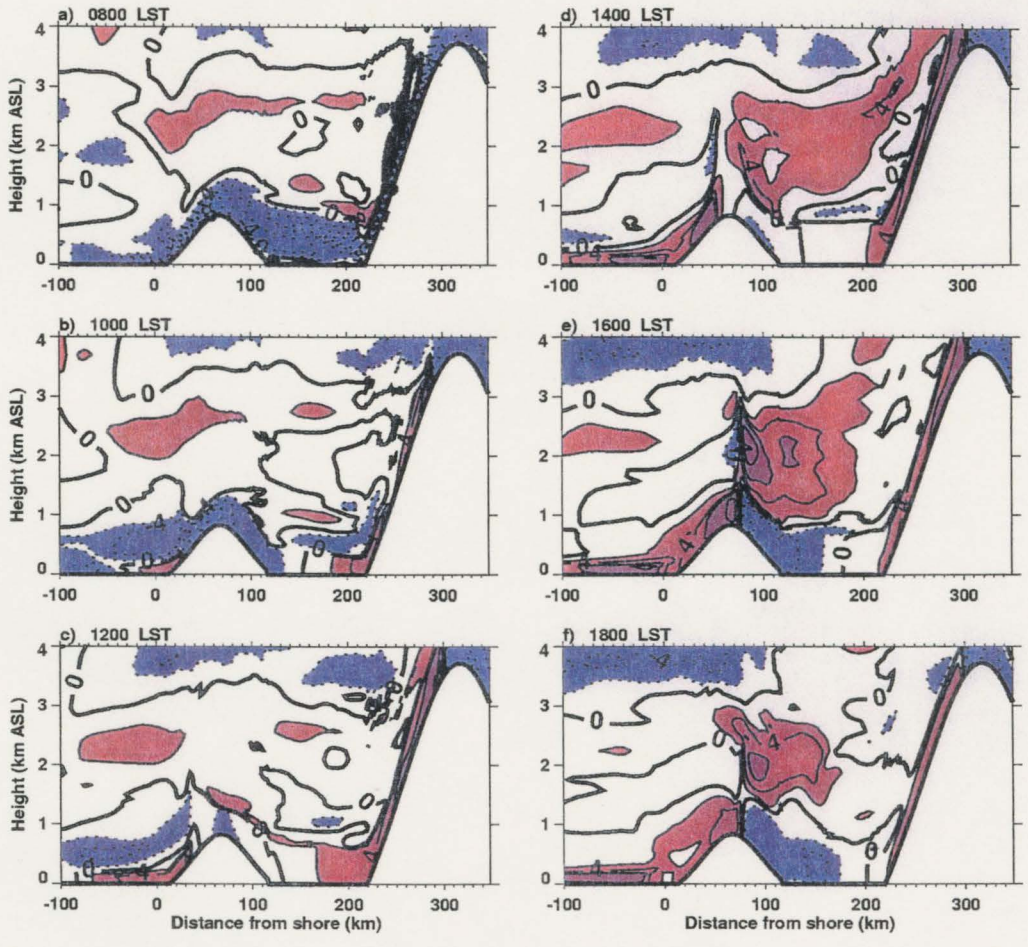

Figure 4.2 As in Fig. 4.1, except for the idealized dual-mountain case.

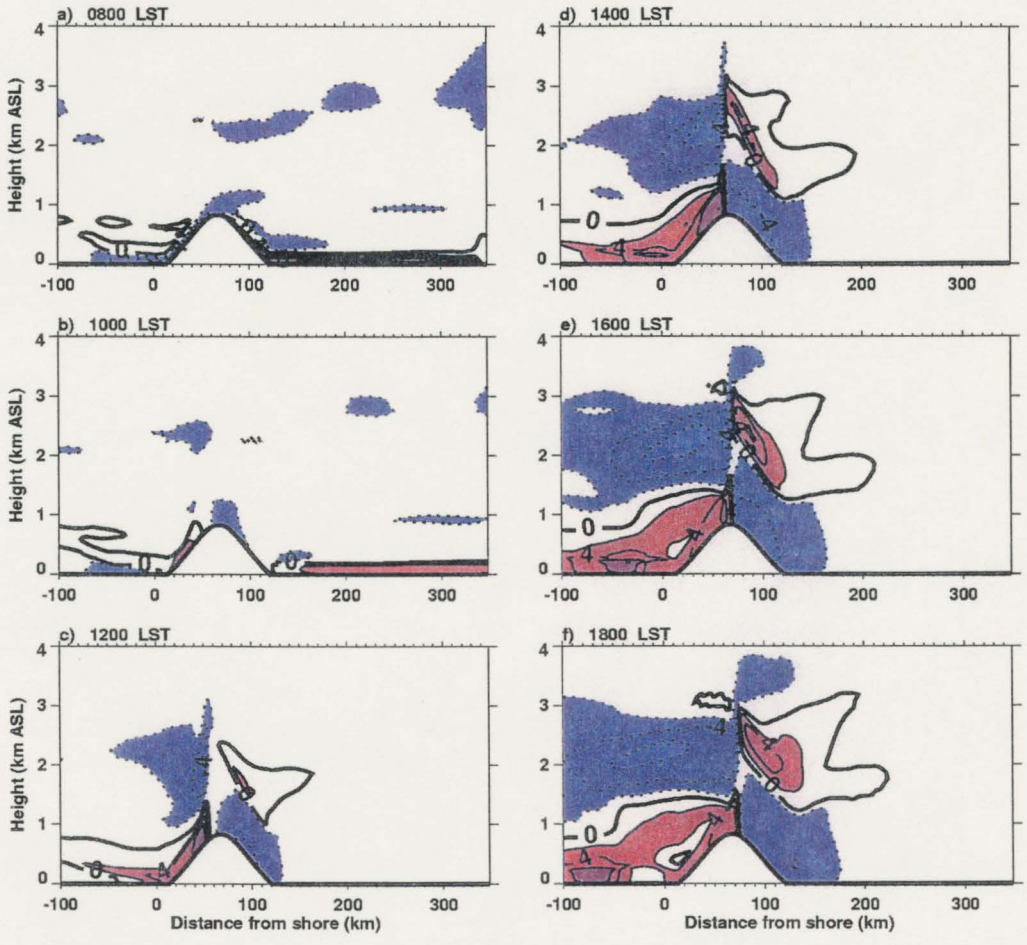

Figure 4.3 As in Fig. 4.1, except for the idealized coastal mountain case.

coastal mountain propagated away from the mountain with a density current-like structure (0800 LST, Fig. 4.3a). As the temperature of the land increased, the upslope flows and their return flows became established. The solenoidal flow had a greater horizontal extent on the westward side of the mountain because of the addition of the sea-breeze flow. The vertical structure of the flow was simpler in this case than in any other simulation that included sloping terrain.

Similar to this study, Cui et al. (1998) compared simulations across Monterey Bay with and without the Sierra Nevada range. In contrast with our results, they show a stronger sea-breeze return flow with the Sierra Range present. This is possibly because their initial background wind direction was northeasterly. Cui et al. (1998) suspect that the gravity-inertia waves produced by flow with an easterly component over the Sierra Nevada have an amplitude great enough to modify the coastal flows. They found a larger difference in the along-coast winds, the focus of their study, than the across-coast winds when comparing the Sierra vs. no-Sierra simulations.

Fig. 4.4 shows the no-coastal-mountain case, with the inland mountain as the only mountain in the simulation. Strong downslope flow that developed in the night and its strong return flow dominated the winds in the morning. Whereas the downslope flow weakened considerably between 0800 LST and 1200 LST, the westerly flow above weakened very little, continuing to dominate the winds above 1 km ASL throughout the day.

The results for the case with flat terrain are shown in Fig. 4.5. In this simulation

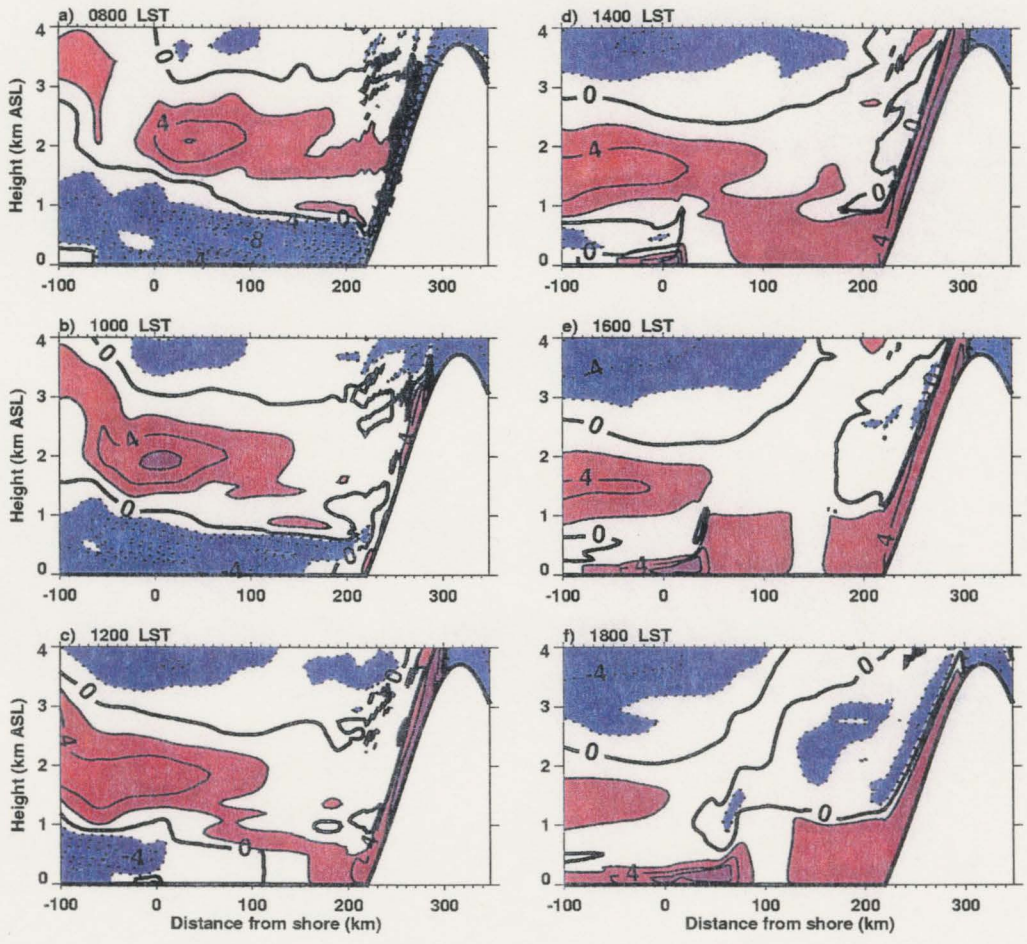

Figure 4.4 As in Fig. 4.1, except for the idealized inland mountain case.

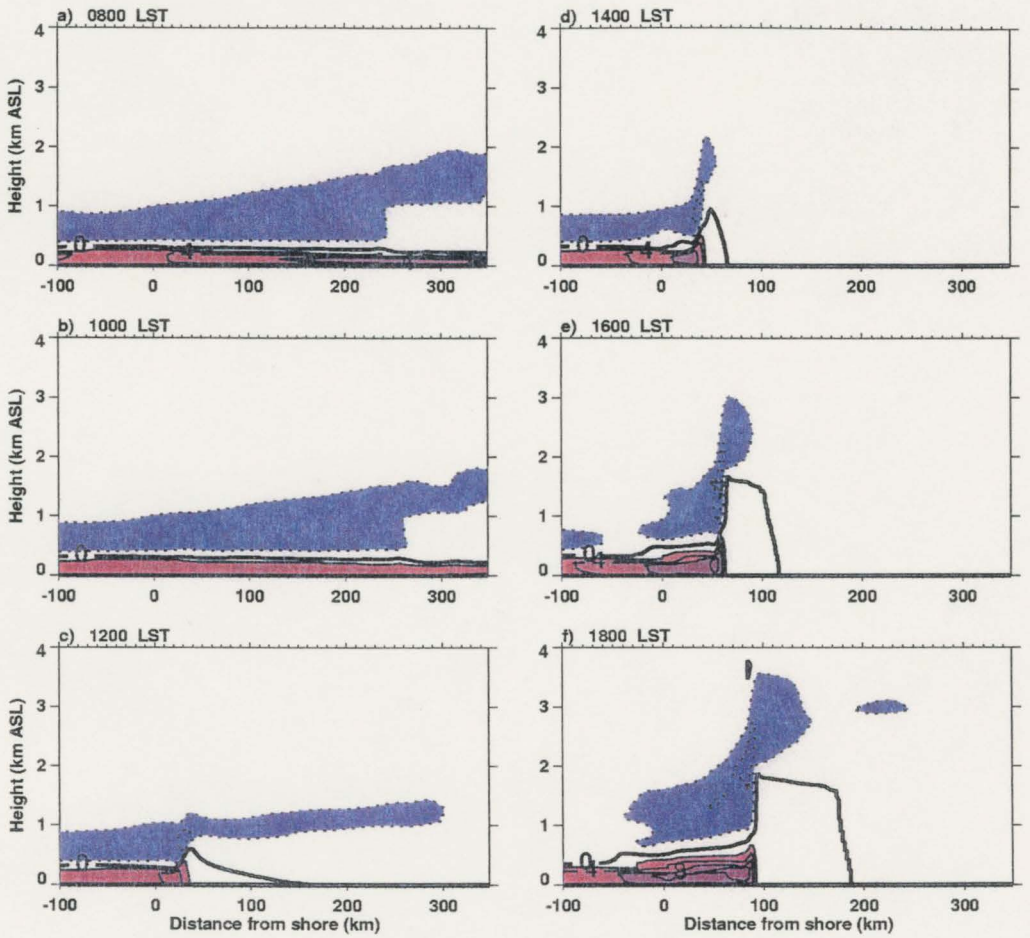

Figure 4.5 As in Fig. 4.1, except for the flat terrain case.

the onshore flow from the previous day did not reverse over night as expected. The sea breeze continued inland with a gravity current-like structure (not shown). A possible explanation is that the soil was too moist and therefore the land did not cool off enough during the night for the temperature gradient between land and water to reverse. Nevertheless, a new sea breeze did form by 1200 LST (Fig. 4.5c) after the old sea breeze diminished. The strongest sea breeze flow seen in any of the simulations presented here, with a speed of 8 m s^{-1}, developed in a shallow layer, with a weak return flow above it. Ookouchi et al. (1978) also produced a stronger modeled sea breeze in their flat terrain case than their mountain cases. These model results are consistent with observations, e.g., the sea breeze at Melville and Bathurst Islands (Skinner and Tapper 1994), which have a maximum terrain height of approximately 120 m, is stronger than the sea breeze measured on Taiwan, which has a maximum terrain height of ~3000 m (Johnson and Bresch 1991; Chen and Li 1995). In the absence of terrain, the vertical structure of the sea breeze was dominated by the thermal structure of the air mass, i.e., the onshore flow was confined to the inversion layer (time series of potential temperature are shown in the next section).

Lu and Turco (1994) ran a similar set of 2-D simulations: sea breeze flow with 1) flat terrain, 2) a coastal mountain (3 different heights), and 3) an inland mountain (also with 3 different heights), but they did not simulate the sea breeze with both a coastal and an inland mountain in the domain. The flat terrain case and medium height coastal mountain case (their Figures 6 and 14, respectively) have vertical structures similar to the flat terrain and coastal mountain cases shown here. The coastal mountain in this study

and in Lu and Turco's (1994) were about the same distance from the shore, making those simulations more appropriate to compare. The mountain in their highest inland mountain case is 2 km high, about one-half the height of the inland mountain case shown here. Consequently, the vertical structure of their inland-mountain-only case is quite different in the later stages of the sea breeze (see, for example, their Figure 17), but some similarities appear in the early stages, such as a clearly defined slope flow separate from the sea breeze. The comparison of their inland-mountain case with our inland-mountain case during the first day of the simulation (not shown), which did not include strong westerly flow above 1 km, show more similarities, but the fact that our inland mountain was 140 km farther inland from the shore than theirs naturally caused differences in the timing of the blending of the sea breeze and upslope flows.

Figures 4.6 - 4.10 show results from simulations 6 - 10, the simulations that have the same terrain configurations as in simulations 1-5, but no water in the domain, only short grass. The smoothed terrain case, Fig. 4.6, shows the winds at 0800 LST (Fig. 4.6a) were quite similar to the winds in the corresponding case with water (Fig. 4.1a), except for a greater westward extension of the slope flow on the west side of the coastal mountain in the simulation with water. By 1200 LST (Fig. 4.6c), however, the winds were very different from the land/water contrast case west of the crest of the coastal mountain below 1 km ASL, yet almost identical east of the crest. Instead of the blended sea breeze and upslope flow, only a small region of weak upslope flow developed on the western side of the coastal mountain. With time, a deep upslope flow formed, but the winds were weaker than the winds in the combined sea breeze/slope flow in the

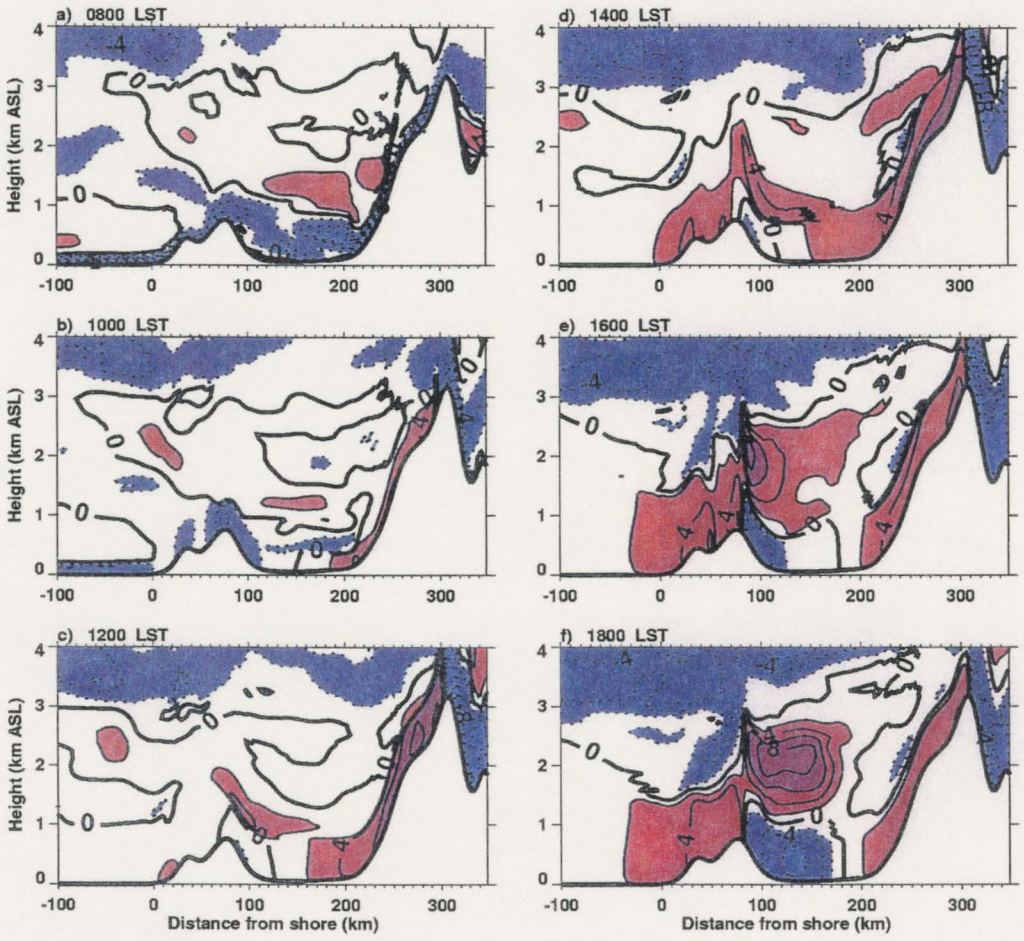

Figure 4.6 As in Fig. 4.1, except there is short grass rather than water west (left) of x = 0 km.

corresponding case with water (Fig. 4.1).

In the idealized dual-mountain case, without the effects of the land-water contrast, the downslope flow for the coastal mountain was much stronger in the morning (Fig. 4.7) than the case with water and propagated westward as a density current (not shown). The upslope flow started later in the day without the enhancement from the land/water contrast (compare Fig. 4.7 with Fig. 4.2). The solenoidal flow about the coastal mountain

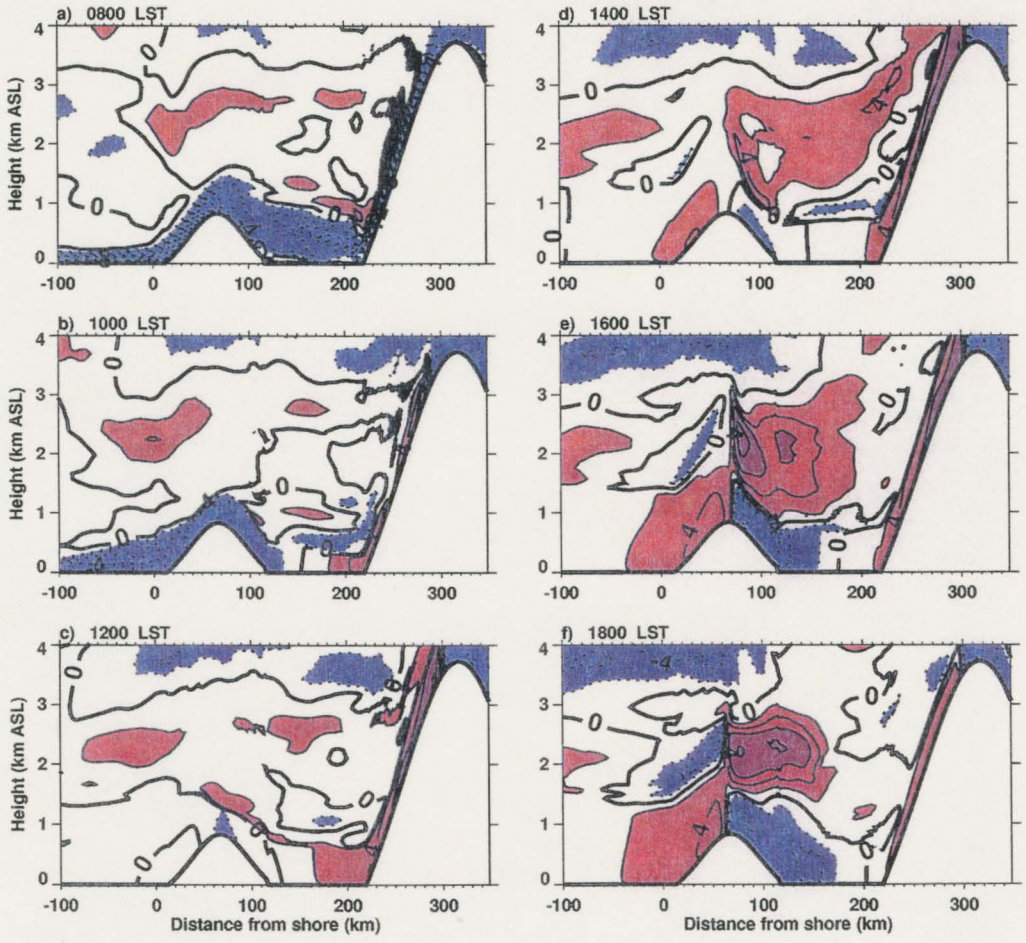

Figure 4.7 As in Fig. 4.6, except for the idealized dual-mountain case.

was more symmetrical than in the water case, as expected, but it was perturbed by the presence of the inland mountain. Again, the results east of the crest of the coastal mountain were quite similar to the case with water (Fig. 4.2).

The simulation with only the coastal mountain and no water (Fig. 4.8) looked very similar to the corresponding case with water (Fig. 4.3) from the mountain crest eastward. Again, without the sea breeze, the upslope flow on the west side of the mountain was

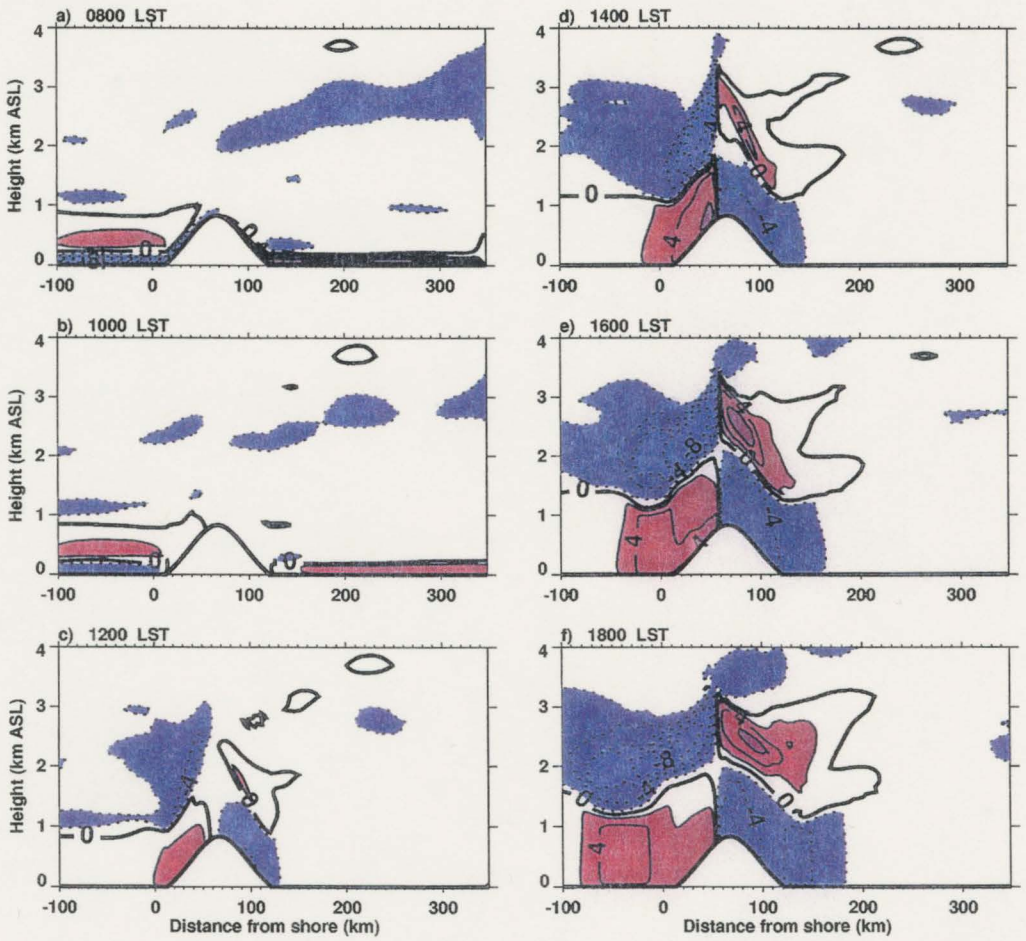

Figure 4.8 As in Fig. 4.6, except for the idealized coastal mountain case.

much weaker than in the water case. With only the inland mountain in the domain (Fig. 4.9) the downslope flow at 0800 LST (Fig. 4.9a) was much stronger than in the corresponding case with water and propagated westward like a density current, uninhibited by any perturbation created by the presence of the water. Even though the downslope flow was stronger, the return flow was weaker than in the corresponding water case. With no sloping terrain or land/water contrast, there was almost no evolution of the

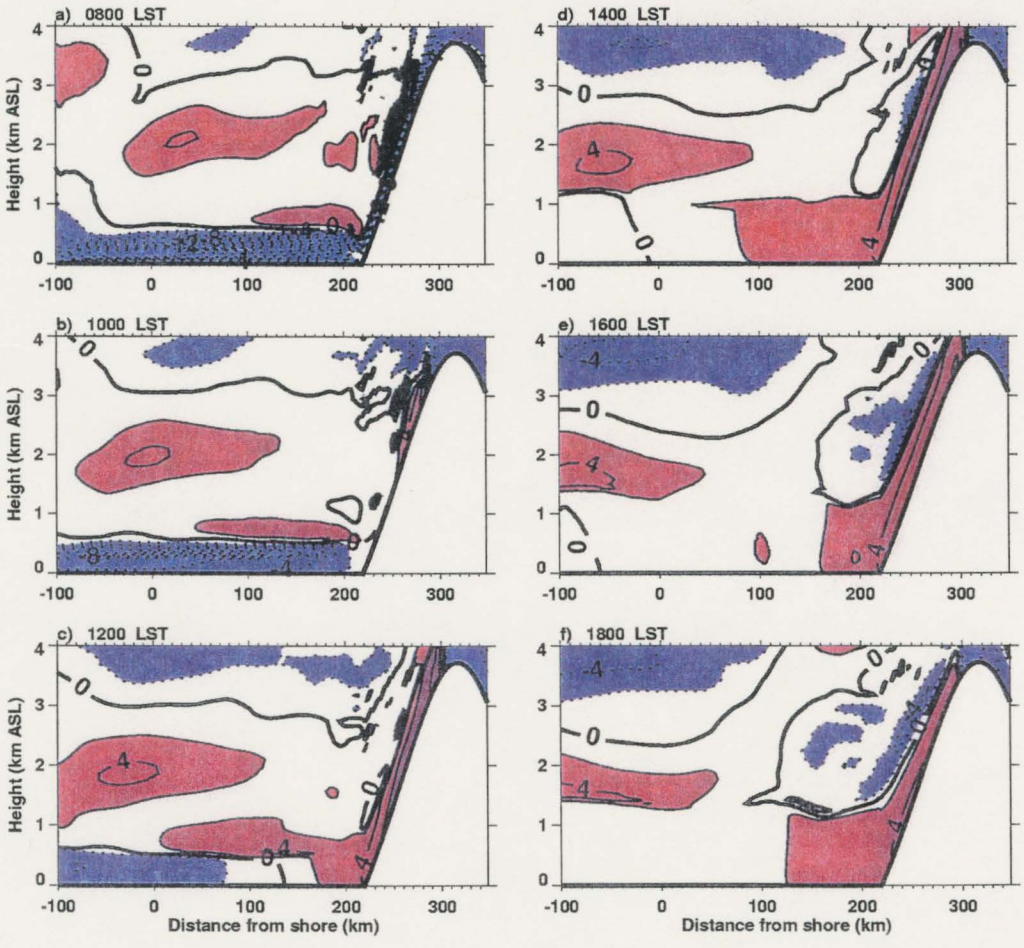

Figure 4.9 As in Fig. 4.6, except for the idealized inland mountain case.

winds with time. The winds stayed easterly at 1 m s^{-1}, as initialized (not shown).

As mentioned previously, Mahrer and Pielke (1977) were the first to publish comparisons of a mountain-valley wind system, sea breeze, and the combination of both. Their case with a single mountain and no water in the domain had a solenoidal wind system that was more symmetrical than the case shown in Fig. 4.8, possibly because their simulation was initialized with a zero gradient wind, unlike our case. When the slope flow was combined with the sea breeze due to the land-water contrast, Mahrer and Pielke (1977) found that the upslope flow and the sea breeze flow became integrated, leading to stronger flow on the seaward side, and the advection of the east side circulation to the east. Our results are consistent with these. The third and final set of west-east cross sections show the differences in the sea breeze and slope flows that occurred when only the vegetation was varied among the simulations. In the runs shown so far, the vegetation was specified as short grass. Fig. 4.10 shows the results of a simulation using evergreen needleleaf. It was expected that the increased surface roughness over land due to the evergreens would slow down the sea breeze flow, and that is what happened. The final simulation (Fig. 4.11), where the vegetation was read into the domain from a satellite derived data set, had results very similar to the evergreen needleleaf simulation, which was not a surprise since much of the mountainous terrain in the region is covered by evergreen needleleaf vegetation.

4.2 Time-height series

4.2.1 Terrain sensitivity with the land/water contrast included

To compare the model results with the lidar data, time-height series of the *u*-

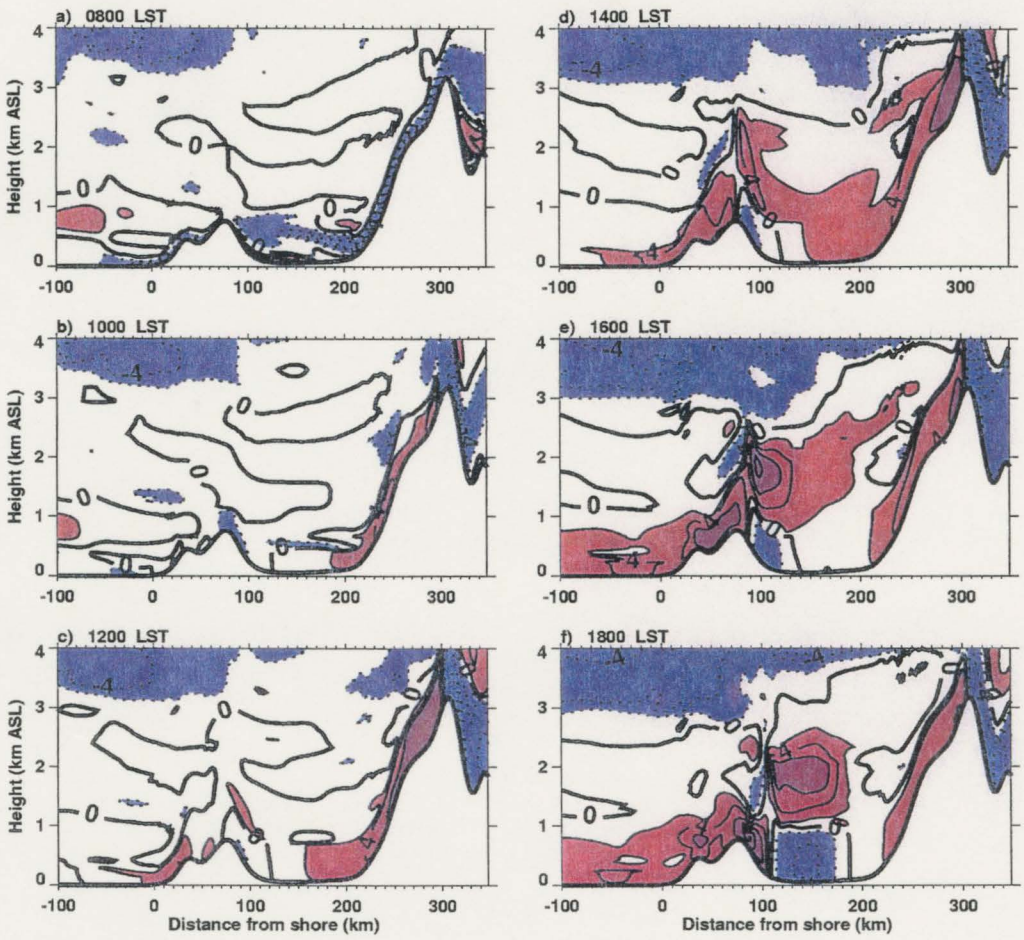

Figure 4.10 As in Fig. 4.1, except the vegetation was specified to be evergreen needleleaf rather than short grass.

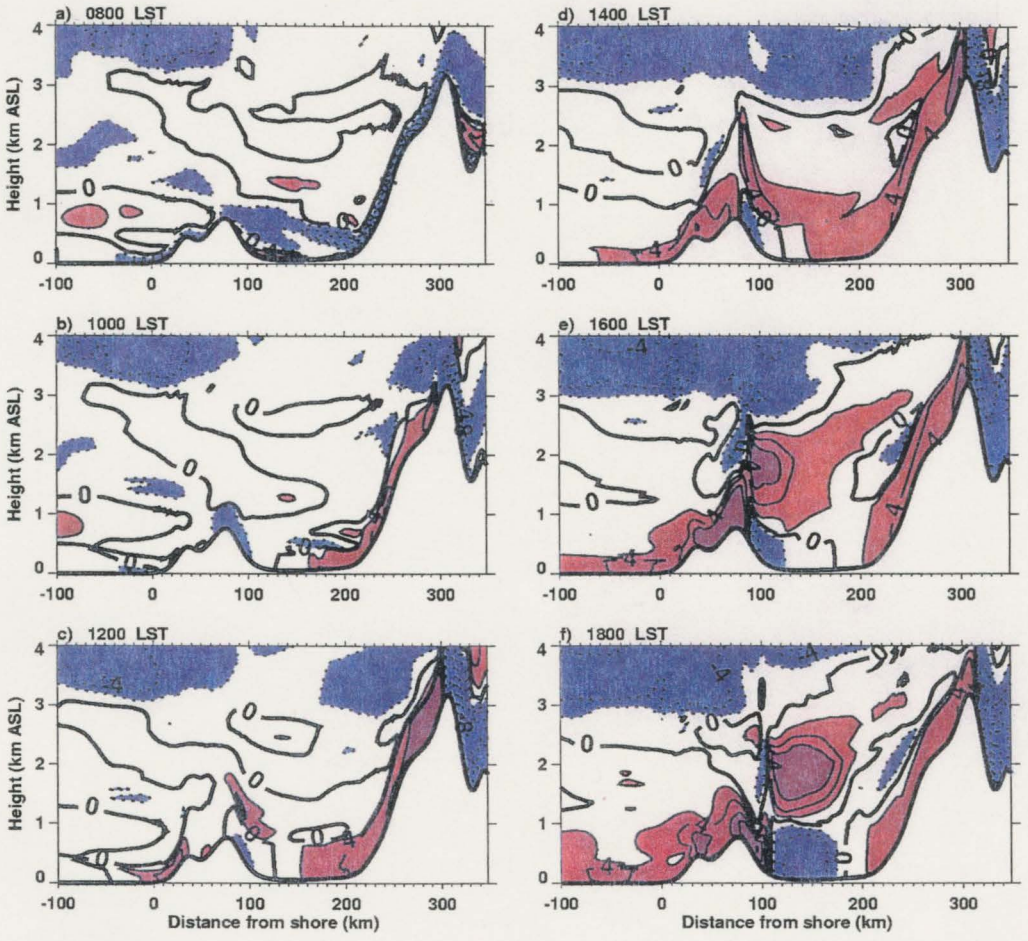

Figure 4.11 As in Fig. 4.1, except the vegetation was read from satellite data rather than specified as short grass.

component of the wind were compiled for each simulation and plotted in the same manner as the lidar time-height series shown in Fig. 2.7. A profile of the u-component of the wind and potential temperature, , were extracted from the shoreline grid point every one-half hour of the simulation. Our intention is to compare the modeled time-height series with the Doppler lidar time-height series, shown again in Fig. 4.14 for convenience, to assess the accuracy of the model results, and to attribute aspects of the lidar analysis to physical processes.

Model output time-height series for simulations including water in the western portion of the domain are shown in Figures 4.12 (u-component of the wind) and 4.13 (potential temperature). Judging from the u-component plots, the time-height series that most resembled lidar data (Fig. 4.14) were the smoothed terrain and idealized dual-mountain simulations, Fig. 4.12a and Fig. 4.12b, respectively.

The results in Fig. 4.12a are from the simulation with the smoothed terrain. Although the modeled sea breeze was slightly weaker than the lidar-measured sea breeze, the overall structure of the sea breeze (solid contours) in this simulation was quite similar to lidar data (Fig. 4.14), including the two scales (shallow and deep) of onshore flow. Above 1500 m ASL there were some general similarities with measurements, such as short-lived weak westerly flow above 2 km early in the period shown, but the model results were more realistic in the lowest part of the domain, below 1.5 km AGL. While the lidar-measured and modeled sea breezes were similar, the structure of the early morning offshore flow was quite different. Though almost as strong as in the lidar measurements, the offshore flow was much shallower in Fig. 4.12 a. This simulation was

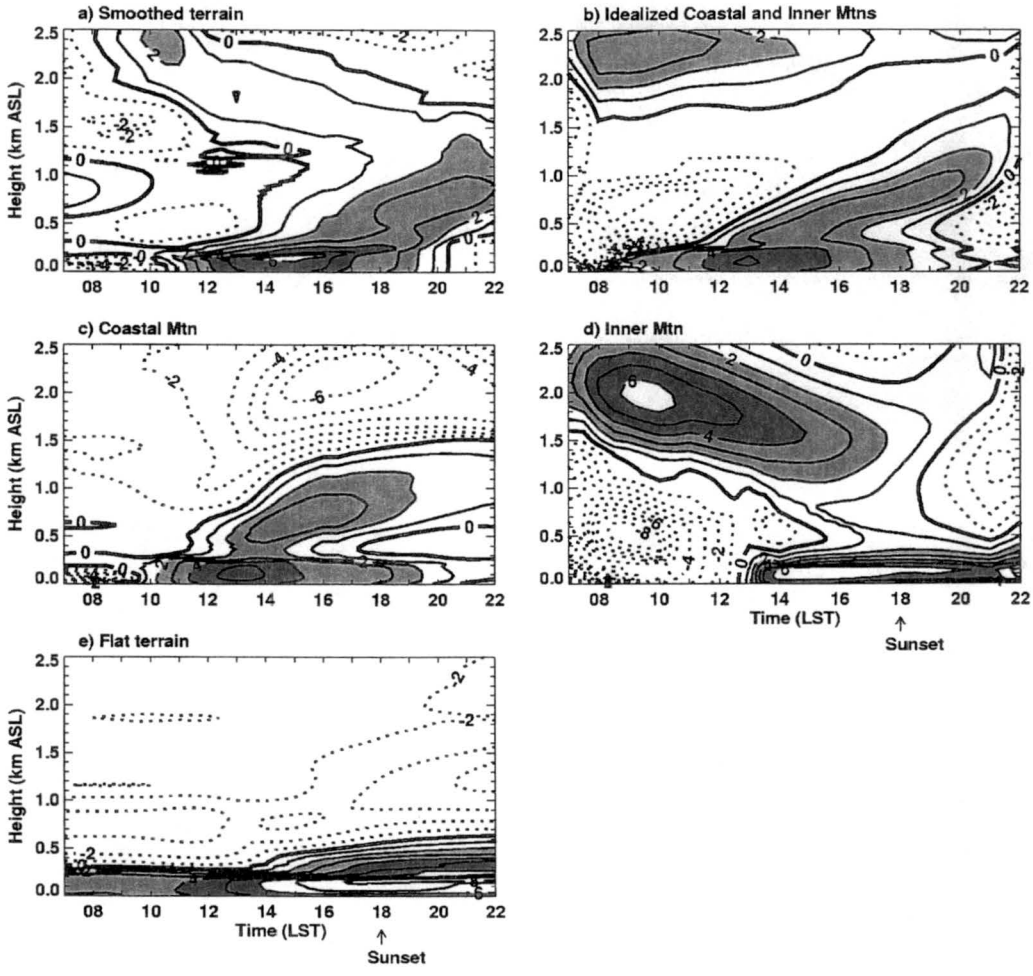

Figure 4.12 Time-height cross sections of the *u*-component of the wind (in m s^{-1}) extracted from the shore in the simulations shown in Figures 4.1 - 4.5. These simulations had water in the western portion of the domain. Profiles were extracted on the hour and half-hour from 0700 to 2200 LST. Solid (positive) contours indicate westerly flow. Dashed contours indicate easterly flow. Westerly flow 2-4 m s^{-1} is shaded grey and flow greater than 4 m s^{-1} is shaded blue. (a) Smoothed terrain. (b) Idealized dual-mountain. (c) Idealized coastal mountain. (d) Idealized inland mountain. (e) Flat terrain.

rerun with an initial sounding having a weaker inversion to see if the early morning offshore flow would be deeper. The strong offshore flow in the modified model results (not shown) was still much more shallow than the lidar observations.

Notable similarities between Fig. 4.12b (idealized dual-mountain case) and lidar data (Fig. 4.14) include: 1) a deep pre-sea breeze offshore flow with speeds up to 6 m s^{-1} at ~ 300 m ASL, 2) shallow, stronger onshore flow imbedded in weaker, deeper onshore flow, 3) the transition back to offshore flow below 1000 m ASL after sunset, and 4) the existence of onshore flow above 1500 m ASL early in the period shown. The most critical result of this simulation and the one shown in Fig. 4.12a is (2), the appearance of the 2 scales of onshore flow. The shallow sea breeze (flow below 300 m) was 2 m s^{-1} weaker than lidar measurements, but the maximum wind occurred at ~1300 LST, as in lidar measurements and surface station measurements (not shown). Although similarities were evident between lidar and RAMS results in the morning offshore flow, the vertical structure of this flow in the model results was more 'compressed' than observed, i.e., overall it was not as deep and the stronger speeds were in a thinner layer, but was closer to the lidar results than the smoothed terrain simulation. Again, the strongest similarities between model results and lidar data occurred in the lowest 1500 m of the domain. The offshore flow above the mature sea breeze in the lidar data does not appear in either of these simulation results (4.12a or 4.12b).

The difference in the vertical structure of the morning offshore flow between the two simulations shown in Figs. 4.12a and 4.12b was also evident in the potential temperature (θ) plots, Figs. 4.13a and 4.13b. Evidence of mixing (the nearly adiabatic

layer between 100 m and 1000 m, from 0800 and 1000 LST) in the idealized dual-mountain simulation was not apparent in the smoothed terrain simulation. Looking at the u-component and plots for all simulations, it appears that the presence and depth of the offshore flow was tied to the vertical structure of , i.e., where did not change much with height, offshore flow was present.

The effects of removing the inland mountain are seen in the model results presented in Fig. 4.12c. In this simulation only the coastal mountain was present. The structure of the sea-breeze flow itself was similar to the other simulations examined so far and to the lidar data, with a shallow, stronger layer of onshore flow embedded in a weaker, deeper layer. The modeled sea breeze had other characteristics similar to lidar data, such as timing of onset and depth, but the onshore flow was weaker. These results imply that the dual structure of the sea-breeze flow was associated with the coastal mountain, and not with the inland mountain. As in the smoothed terrain case, the early morning offshore flow near the surface was strong, yet the vertical extent was inhibited. The potential temperature time-series below 500 m were also quite similar between these two cases (Fig. 4.13a and Fig. 4.13c). The major effect of the missing inland mountain was the lack of westerly, or onshore, flow above 1500 m throughout the simulation. In the absence of westerly flow above the sea breeze layer, a 6 m s^{-1} offshore flow developed above the sea breeze, which was much stronger than seen in lidar measurements, and too strong to be a compensatory sea breeze return flow.

Dramatic differences existed in the model results shown in Fig. 4.12d compared to the other simulations and lidar measurements. In this simulation, the coastal mountain

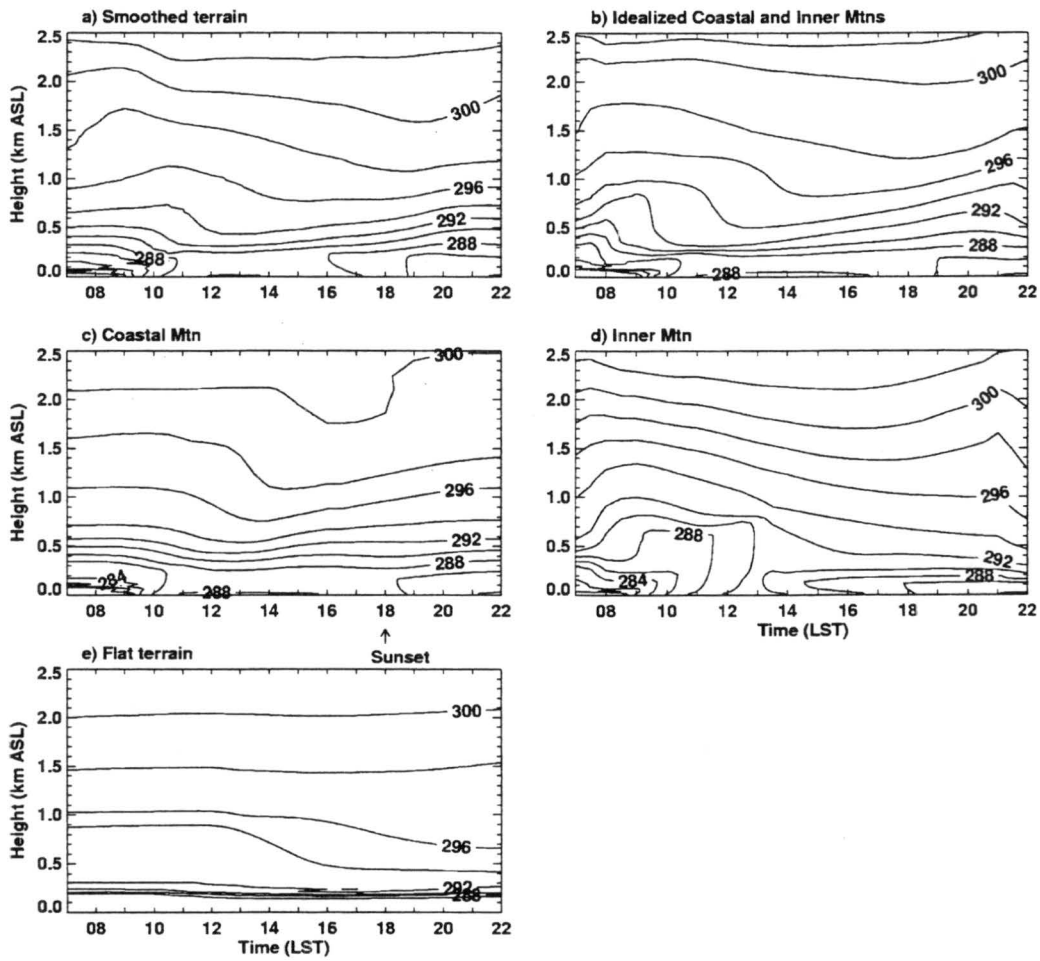

Figure 4.13 As in Fig. 4.12, except for potential temperature, θ.

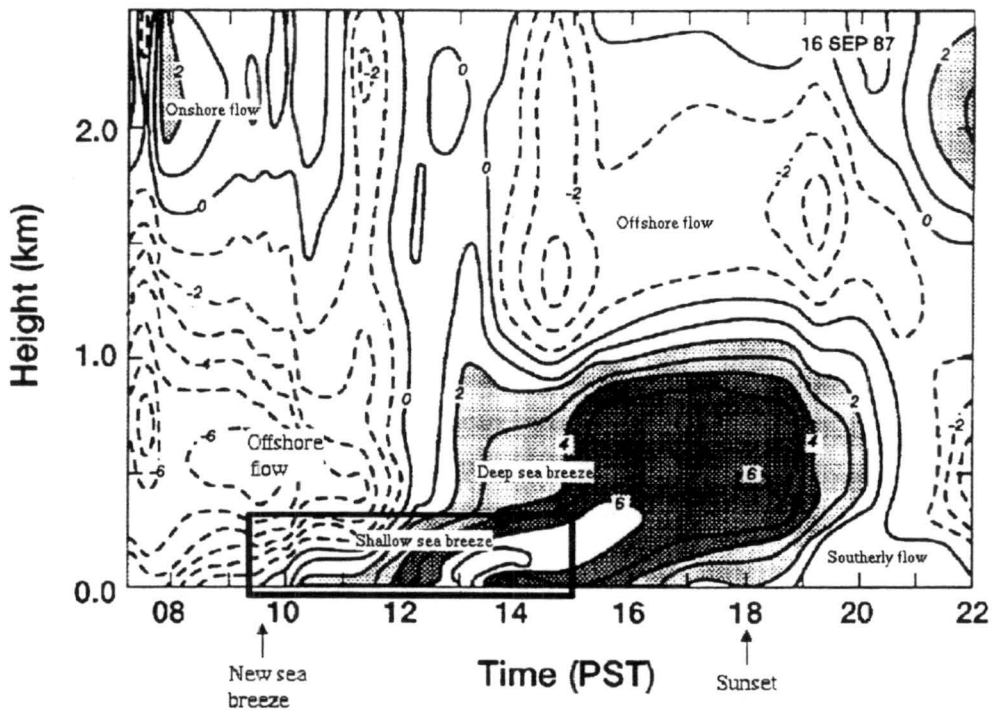

Figure 4.14 Time-height cross section of vertical profiles of the *u*-component of the wind as measured by the ETL Doppler lidar (explained in Section 2.2.2.2, Fig. 2.7, from Banta et al., 1993). Dashed lines represent flow from the east, solid lines flow from the west. Westerly flow 2-4 m s^{-1} has light shading, flow from 4 to 6 m s^{-1} has heavier shading.

was removed, leaving the land/water contrast and the inland mountain as the two driving forces for the mesoscale winds. There are three striking features in these results: 1) the lack of dual structure in the sea-breeze flow, 2) the strong offshore flow in the morning, and 3) the strong morning onshore flow aloft, above 1500 m ASL. The sea-breeze flow was strong (> 6 m s^{-1}) but shallow (< 500 m), without the weaker and deeper onshore flow seen in the other simulations and measurements. Early-morning offshore flow was deep, coinciding with the deeper mixing indicated in the plots between 10:00 and 12:00 LST, and reached speeds of 8 m s^{-1}. The opposing onshore flow above this was also strong, well defined, and lasted many hours. It is clear from comparing this simulation with the others, and measurements, that the depth of the modeled sea breeze was enhanced by the presence of the coastal mountain, and the presence of the inland mountain significantly affected winds above 1500 m ASL.

Figure 4.12e shows model results from the flat terrain simulation. The onshore winds were generated by the differential heating of the land and water only. As shown in the previous section, the sea breeze from the previous day did not reverse to a land breeze over night, therefore the plot shows onshore flow at the surface for the whole period. The depth of the onshore flow in this simulation did not exceed ~650 m ASL since the temperature inversion dominated the vertical structure of the sea-breeze flow (Fig. 4.13e).

When the flat terrain simulation (Fig. 4.12e) and the 'inland mountain only' simulation (Fig. 4.12d) are compared to simulations that included the coastal mountain (Fig's 4.12a, 4.12b, and 4.12c), we see that the depth of the onshore sea-breeze flow was limited without the coastal mountain, lacking the dual structure measured by the lidar,

and the flow was stronger. This implies that the coastal mountain generated a slope flow that enhanced the depth of the onshore flow, but not necessarily the speed of it. The depth of the onshore flow generated only by the local-scale land/water contrast (Fig. 4.12d and 4.12e) is similar in depth to the shallow portion of the sea breeze in the simulations that show the dual structure in the onshore flow. This implies that the land/water contrast drives the shallow sea breeze.

When the flat terrain simulation and the 'coastal mountain only' plot (Fig. 4.12c) are compared to simulations that included the inland mountain (Fig's 4.12a, 4.12b, and 4.12d), it is apparent that flows generated by a mountain of this size (3800 m), even 300 km inland, influenced the flow above 1500 m ASL near the shore.

4.2.2. Terrain sensitivity without the land/water contrast

Figures 4.15 and 4.16 show results from the simulations with short grass only in the domain. Therefore, the mesoscale wind flows generated in these simulations were due solely to the terrain. Comparing the dual-mountain results with water (Fig. 4.12a and Fig. 4.12b) to those without water (Fig. 4.15a and Fig. 4.15b) shows that above 1500 m ASL the results were fairly similar between the water and no-water runs. This implies that the land/water contrast did not strongly influence the winds above 1500 m in these simulations. The land/water contrast did strongly influence the flow in the lower 1500 m of the domain, however, as indicated by the large differences seen in the winds between all of the water and no-water simulations. plots (Fig. 4.16) also show large differences between the water and no-water simulations (Fig. 4.13). A deep mixed layer that developed by 10:00 LST in each no-water simulation was not seen in the simulations

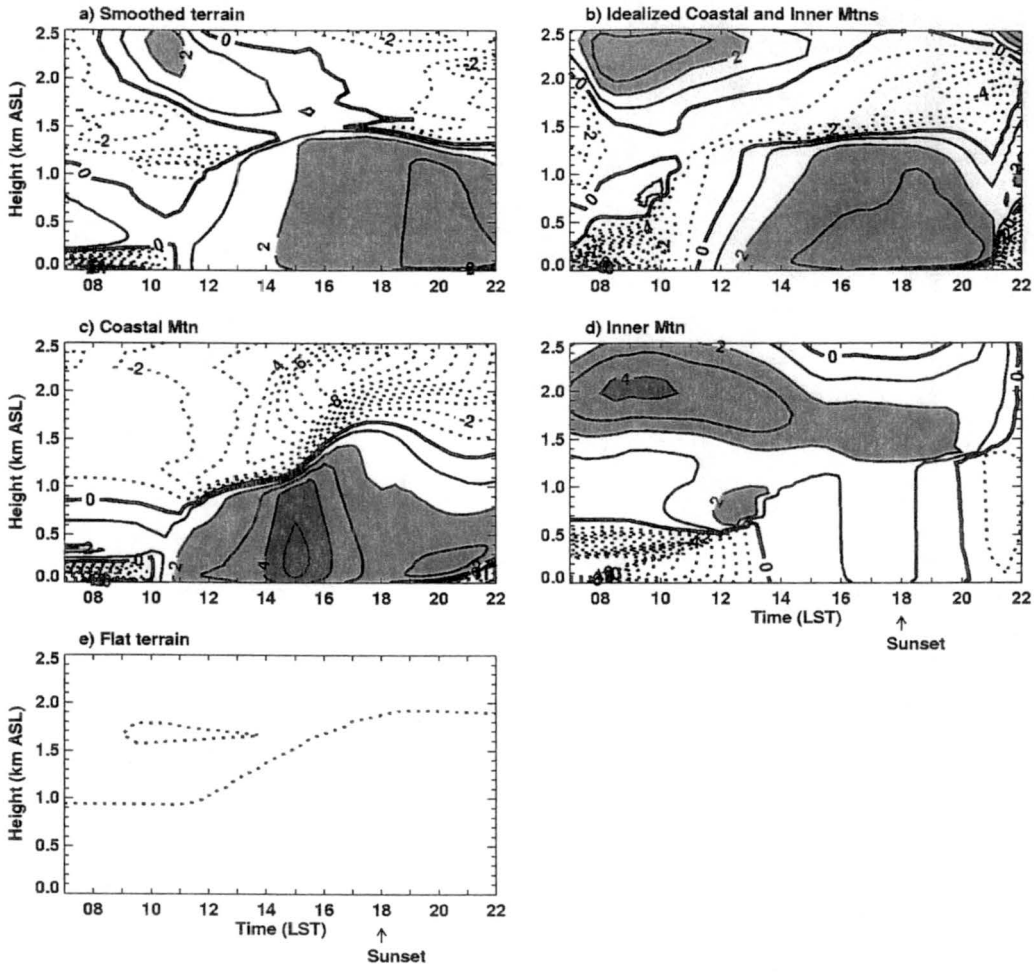

Figure 4.15 As in Fig. 4.12, except for the simulations shown in Figures 4.6 - 4.10, simulations with short grass rather than water in the western portion of the domain.

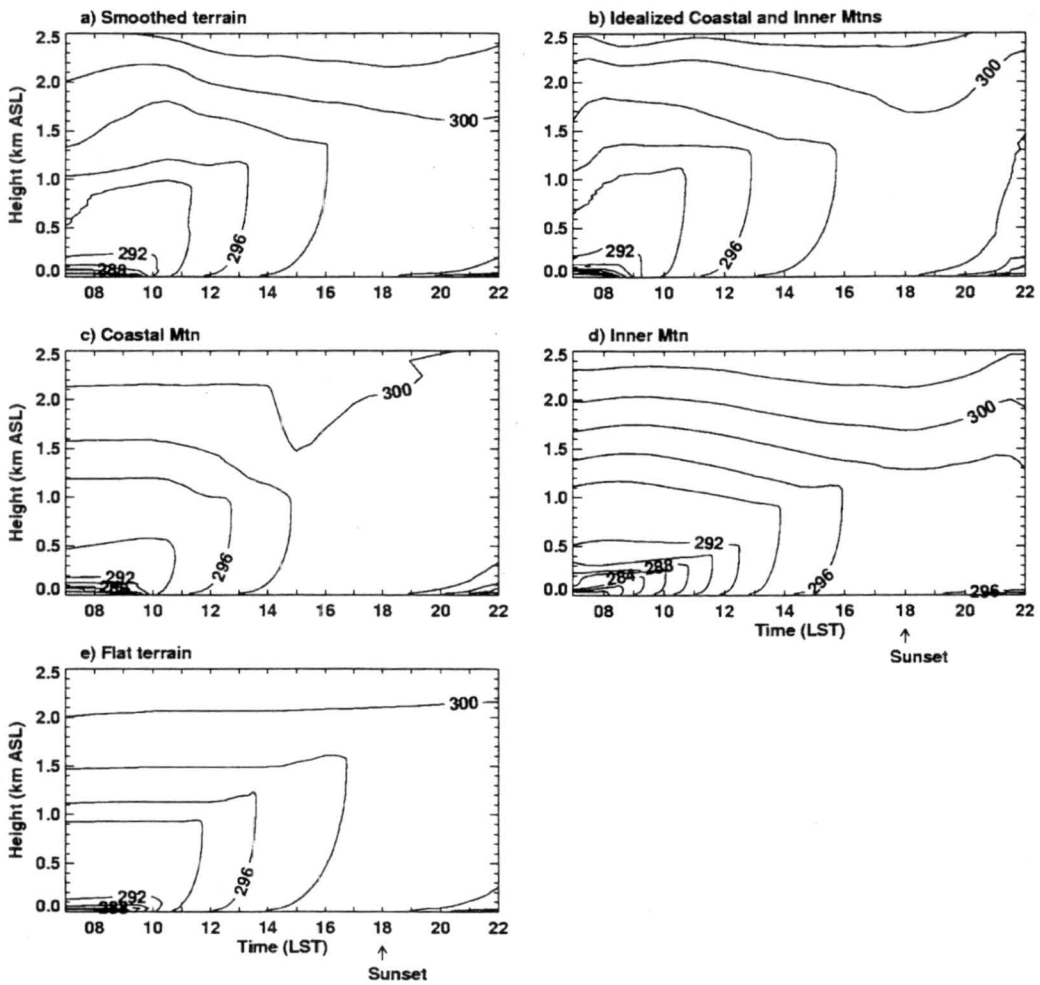

Figure 4.16 As in Fig. 4.13, except for simulations that had short grass rather than water in the western portion of the domain.

with water in the domain (Fig. 4.13). Without the cooling effect of the sea-breeze flow, the air mass west of the coastal mountain heated up much faster in the no-water simulations. Once the flow shifted from downslope to upslope, the vertical growth of the westerly flow occurred suddenly, coinciding with the mixing seen in the θ plots, and the ensuing westerly flow was weak and deep.

As in the dual-mountain cases, the coastal-mountain-only case (Fig. 4.15c) had weak and deep afternoon westerly flow, but it was stronger without the presence of the inland mountain, a characteristic also seen in the west-east cross sections. Winds above 1500 m AGL were similar in structure to the case with water (Fig. 4.12c). Without the coastal mountain or the land/water contrast (Fig. 4.15d), the afternoon westerly flow below 1500 m AGL was quite weak. Strong winds above 1500 m associated with the inland mountain appeared in the no-water simulation, as in the corresponding case with water in the domain, although weaker. Without any variation in terrain, or a land/water contrast, the winds barely evolved over time (Fig. 4.15e).

4.2.3 Vegetation

The differences in the wind flow among the three simulations with different vegetation classes were small (Fig. 4.17), especially early in the period plotted. Above 2000 m the winds were slightly stronger in the short grass simulation. θ plots (Fig. 4.18) show slightly warmer potential temperatures near the surface around noon LST in the short grass simulation. Associated with these warmer potential temperatures were stronger winds starting earlier, similar to lidar-measured winds. Weaker sea breezes were modeled when there was increased surface roughness due to the vegetation, i.e.,

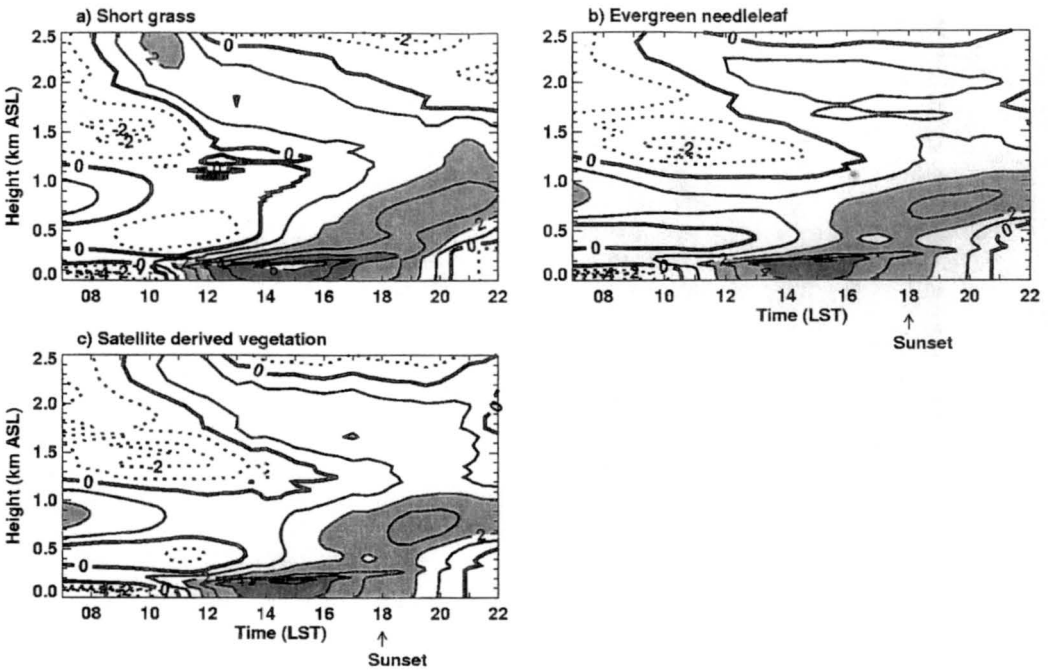

Figure 4.17 Time-height series as in Fig. 4.12 (smoothed terrain case, water in the western portion of the domain), except comparing the 3 simulations that had different vegetation classifications. (a) Short grass. (b) Evergreen needleleaf. (c) Satellite derived vegetation.

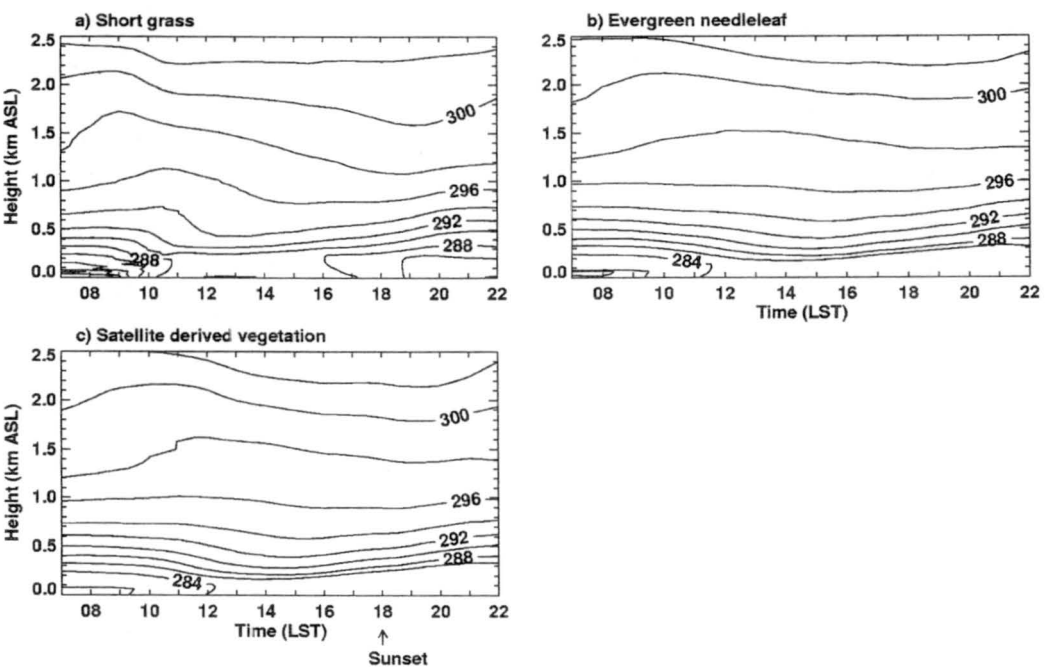

Figure 4.18 As in Fig. 4.17, except for potential temperature, θ.

evergreen needleleaf vs. short grass.

4.2.4. Summary

As expected, the inclusion of both the coastal and inland mountains in the model domain yielded the most realistic results. The slope flows generated by each mountain influenced the structure of the sea-breeze flow near the surface and the expected return flow above the sea-breeze layer. The coastal mountain generated a weak slope flow ~ 1500 m deep, producing the larger scale onshore flow seen in the lidar sea-breeze measurements. The land/water contrast was responsible for the shallow sea breeze. The presence of the inland mountain greatly influenced the flow above 1500 m ASL by generating westerly flow above 1500 m ASL. Since simulations with the inland mountain had westerly flow above 1500 m and simulations without it had only easterly flow at these heights, this topographic feature clearly affected winds near the shore even though it was hundreds of km inland. In this 2-D setting, the westerly flow above 1500 m ASL associated with the inland mountain hindered the development of a classic sea-breeze return flow.

Chapter 5

Factor separation

5.1 Method

Stein and Alpert (1993) have devised a simple method for computing the contribution of individual factors to the magnitude of a predicted field in a numerical model, and more importantly, the contribution of the interaction of two or more factors to the outcome of the simulation. It is standard among modelers to test a factor of interest by completing a simulation with and without the factor, e.g., topography, and then looking at the difference in the predicted field of interest (see, for example, Doyle (1997)). Stein and Alpert (1993) show that this method leads the investigator to ignore the interaction that occurs between dominating factors, therefore possibly missing important driving forces for the feature of interest. In their 1993 paper, they investigated the contribution of terrain, surface heat fluxes, and the interaction of the two to the amount of precipitation in the Mediterranean region. They found that topography alone, surface fluxes alone, and the interaction of the two factors enhanced rainfall differently in the domain. Using only the subtraction method of investigation, the investigators would have missed the regions where the interaction of the two factors had a strong influence. In addition to finding regions of enhanced precipitation due to topography, their results also indicated the regions where topography can have a negative contribution to, or

inhibit, precipitation.

Their method is based on the idea that a field f, which is a continuous function of c, can be decomposed into a part that is independent of c and a part that is dependent on c. The function is decomposed using a Taylor series-type expansion based on the number of factors to be tested, n. They show there must be 2^n simulations to apply the method.

In the following section we will present factor separation results for different pairs of factors, and investigate the triple interaction between the coastal mountain, inland mountain, and the land/water contrast. The equations used, taken from Stein and Alpert (1993), are as follows:

$$\hat{f}_0 = f_0 \tag{5.1}$$

$$\hat{f}_1 = f_1 - f_0 \tag{5.2}$$

$$\hat{f}_2 = f_2 - f_0 \tag{5.3}$$

$$\hat{f}_3 = f_3 - f_0 \tag{5.4}$$

$$\hat{f}_{12} = f_{12} - (f_1 + f_2) + f_0 \tag{5.5}$$

$$\hat{f}_{23} = f_{23} - (f_2 + f_3) + f_0 \tag{5.6}$$

$$\hat{f}_{13} = f_{13} - (f_1 + f_3) + f_0 \tag{5.7}$$

$$\hat{f}_{123} = f_{123} - (f_{12} + f_{23} + f_{13}) + (f_1 + f_2 + f_3) - f_0 \tag{5.8}$$

In each equation, $\hat{f}$, the fraction of f that is due to the factor or factors under investigation, is calculated from the model output, f, where f is a model-variable field, such as u, 量, etc. Equations (5.5) - (5.7) are for testing pairs of factors, while Eqn. (5.8) is for testing a triple interaction. If two factors to be investigated are (1) topography and (2)

the land/water contrast, and the predicted field of interest, f, is the u-component of the wind, then Eqn. (5.1) represents the simulation that does not include topography or a land/water contrast, and shows the influence on f of the 'hidden' factors, i.e., the factors not under consideration. In Eqn. (5.2), the effects of topography are isolated. A simulation is run with topography, but no land/water contrast, creating the wind field f_1. When the hidden factors, f_0, are subtracted from f_1, we get $\hat{f}_1$, the u-component of the wind as a result of topography only. Likewise, in Eqn. (5.3), the u-component of the wind as a result of the land/water contrast only are calculated, $\hat{f}_2$.

The final step for testing a pair of factors is to retrieve the field of interest due to the interaction of two factors, $\hat{f}_{12}$. Starting with the simulation that has both factors present, subtract the results due to the hidden factors and the factors of interest individually,

$$\hat{f}_{12} = f_{12} - \hat{f}_0 - \hat{f}_1 - \hat{f}_2 . \tag{5.9}$$

Using the right-hand side of Eqn's 5.1 - 5.3 to substitute for the $\hat{f}$ terms results in Eqn. 5.5. Large values of $\hat{f}_{12}$, calculated from Eqn. 5.5, represent regions where the interaction between the two fields is strong. All equations listed are similarly used to test a triple interaction.

5.2 Factor separation results

In this section we present the factor-separation results for three pairs of factors: 1) coastal (f_1) and inland (f_2) mountains (land/water contrast not included); 2) coastal (f_1) and inland (f_2) mountains (land/water contrast included); and 3) idealized dual-mountain

topography (f_1) and land/water contrast (f_2). The figures include west-east cross sections of f_0, f_1, f_2, f_{12}, and $\hat{f}_{12}$, as explained in the previous section. To fully understand the plot illustrating the wind flow as a result of the interaction of the factors, $\hat{f}_{12}$, there are three things to look for: 1) Where is $\hat{f}_{12} = 0$? The interaction of factors has no effect on f, the u- component of the wind, where $\hat{f}_{12} = 0$; 2) Where are the regions of greatest magnitude of $\hat{f}_{12}$? These are the places where the interaction has the most effect; and 3) What is the sign of these regions of greatest magnitude relative to the simulation including both factors? If the sign in $\hat{f}_{12}$ is the same as in the corresponding region of f_{12}, then the interaction of the two factors enhanced the flow modeled in f_{12}; if the sign is opposite, then the interaction of factors opposed, i.e., weakened, the modeled flow. Time-height series of $\hat{f}_{12}$ for the 3 factor pairs are also shown. In addition, a time-height series plot of $\hat{f}_{123}$, the winds as a result of the triple interaction among the coastal mountain, inland mountain, and the land/water contrast is shown.

The results for the coastal mountain (f_1) and inland mountain (f_2) factor pair, without water included in the domain, are shown for two times, 1400 LST (Fig. 5.1) and 1800 LST (Fig. 5.2). It is interesting how much weaker the coastal-mountain slope flows were when the inland mountain was present (compare Fig. 5.1b with Fig. 5.1d). Since the coastal-mountain slope flows were much stronger in f_1 than in f_{12} (and winds in the same region were negligible in f_0 and f_2), the winds due to the interaction of the mountain-induced flows, $\hat{f}_{12}$ (Fig. 5.1e), were opposite in sign to the coastal mountain solenoidal flow (Fig. 5.1d), except for a small region of westerly flow at x = 80 - 110 km and z = ~1 km. This signified that, for the most part, the interaction of both mountain-induced flows

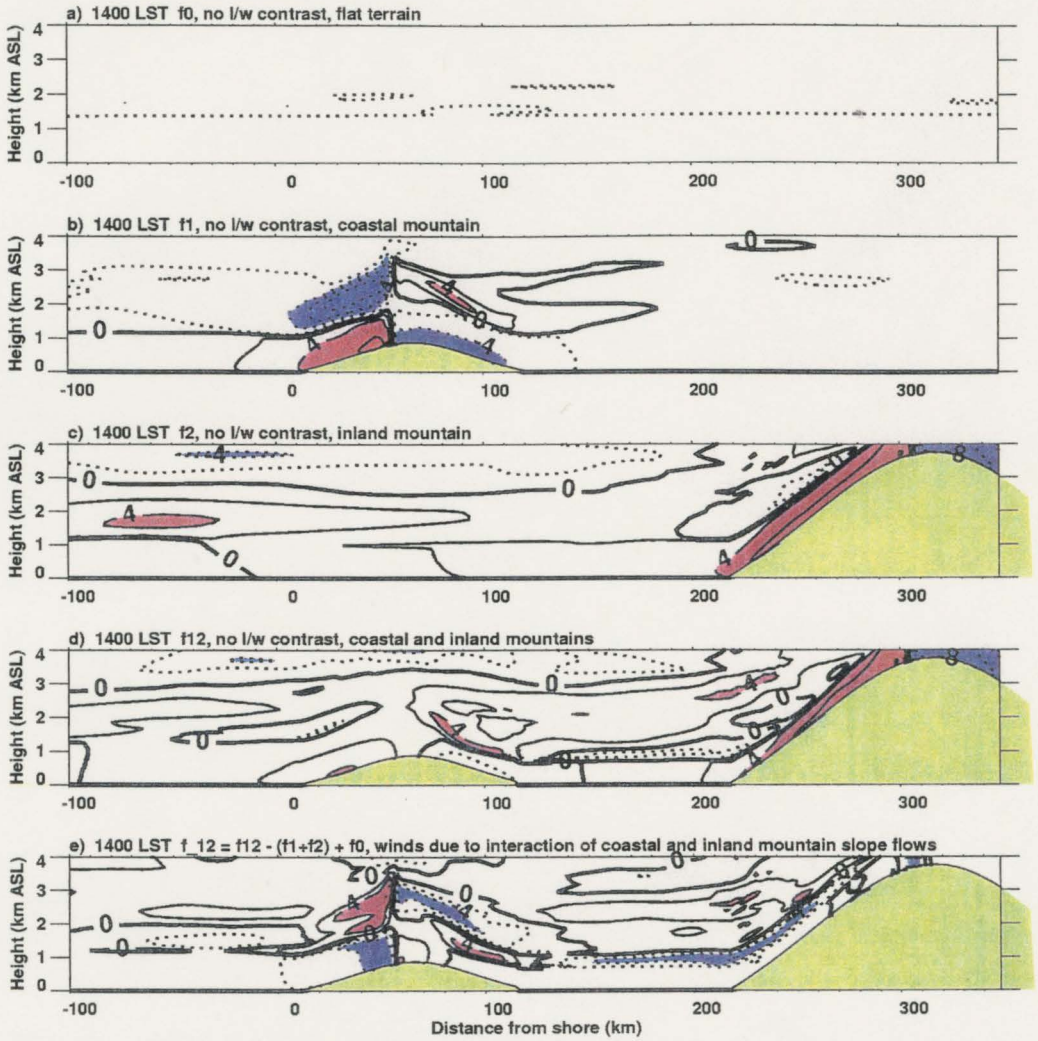

Figure 5.1 West-east cross sections of the modeled u-component of the wind. Solid (positive) contours indicate westerly flow, and increment every 2 m s^{-1}, except in the flat terrain plot, (a), which has 1 m s^{-1} increments. Speeds greater than 4 m s^{-1} are shaded red. Dashed (negative) contours indicate easterly flow, with speeds of magnitude greater than 4 m s^{-1} shaded blue. The first four panels are from the same time, 1400 LST, but different simulations, as indicated by the terrain (yellow shading). The bottom panel shows the winds as a result of the factor separation method employed (see text). The factor pair assessed in this figure is the coastal mountain and the inland mountain, with no water in the domain. (a) f_0 - neither mountain in the domain. (b) f_1 - coastal mountain only. (c) f_2 - inland mountain only. (d) f_{12} - both mountains. (e) $\hat{f}_{12}$ - the winds due to the interaction of the flows induced by both the coastal and inland mountains.

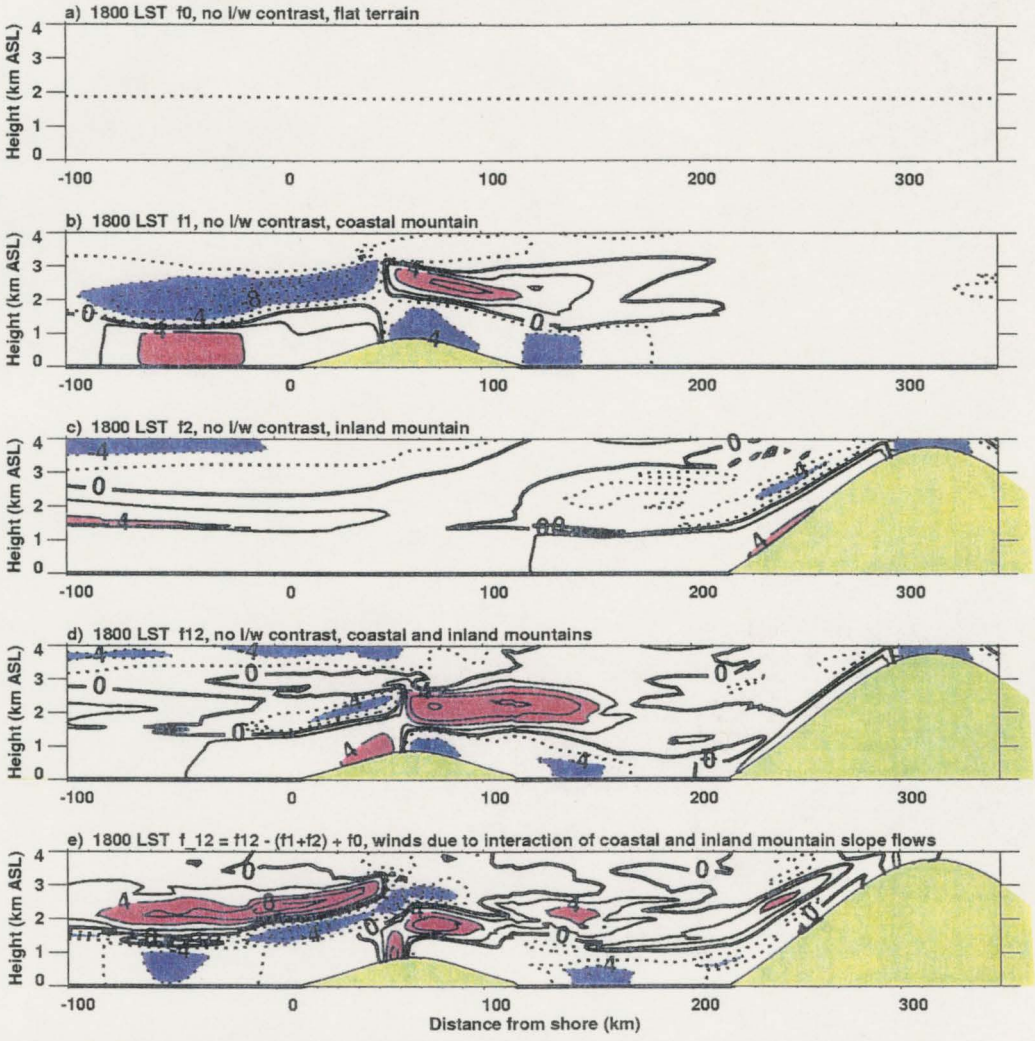

Figure 5.2 As in Fig. 5.1, except for 1800 LST, 4 hr later.

opposed the coastal-mountain solenoidal flow. The interaction of flows also influenced the valley flows in a thin layer above 800 m, somewhat opposing the inland mountain's upslope flow. At 1800 LST (Fig. 5.2) the coastal mountain slope flows with and without the presence of the inland mountain were in closer agreement than 4 hr earlier. The main difference in these winds occurred above 1.5 km ASL, especially in the return flow of the western branch of the coastal mountain upslope flow, which was much weaker when the inland mountain was present. The return flow for the eastern branch, on the other hand, was stronger. Consequently, the interaction of the mountain flows at this time had very little impact on the wind flow at the surface of the coastal mountain, except where the upslope flows converged. The interaction did have a strong influence above 1.5 km or so (Fig. 5.2e), enhancing the return flows, but only in a thin layer. Some influence was still evident on the valley flow, with easterly winds slightly enhanced at the surface.

Figures 5.3 (1400 LST) and 5.4 (1800 LST) show plots for the coastal mountain (f_1) and inland mountain (f_2) factor pair with the land/water contrast included. In this case, only the upslope flow on the east side of the coastal mountain was weaker when the inland mountain was present. The interaction of the slope-induced flows (Fig. 5.3e) enhanced the sea breeze/slope flow on the western side of the coastal mountain, except near the leading edge of the sea breeze where this interaction opposed the advance of the leading edge of the sea breeze. The interaction also enhanced the return flow for the sea breeze/slope flow. Both of these effects, at this time, were in contrast to the previous factor pair. Even with the return-flow enhancement, however, the sea-breeze return flow modeled in f_{12} (Fig. 5.3d) was nearly non-existent. Note that the modeled winds on the

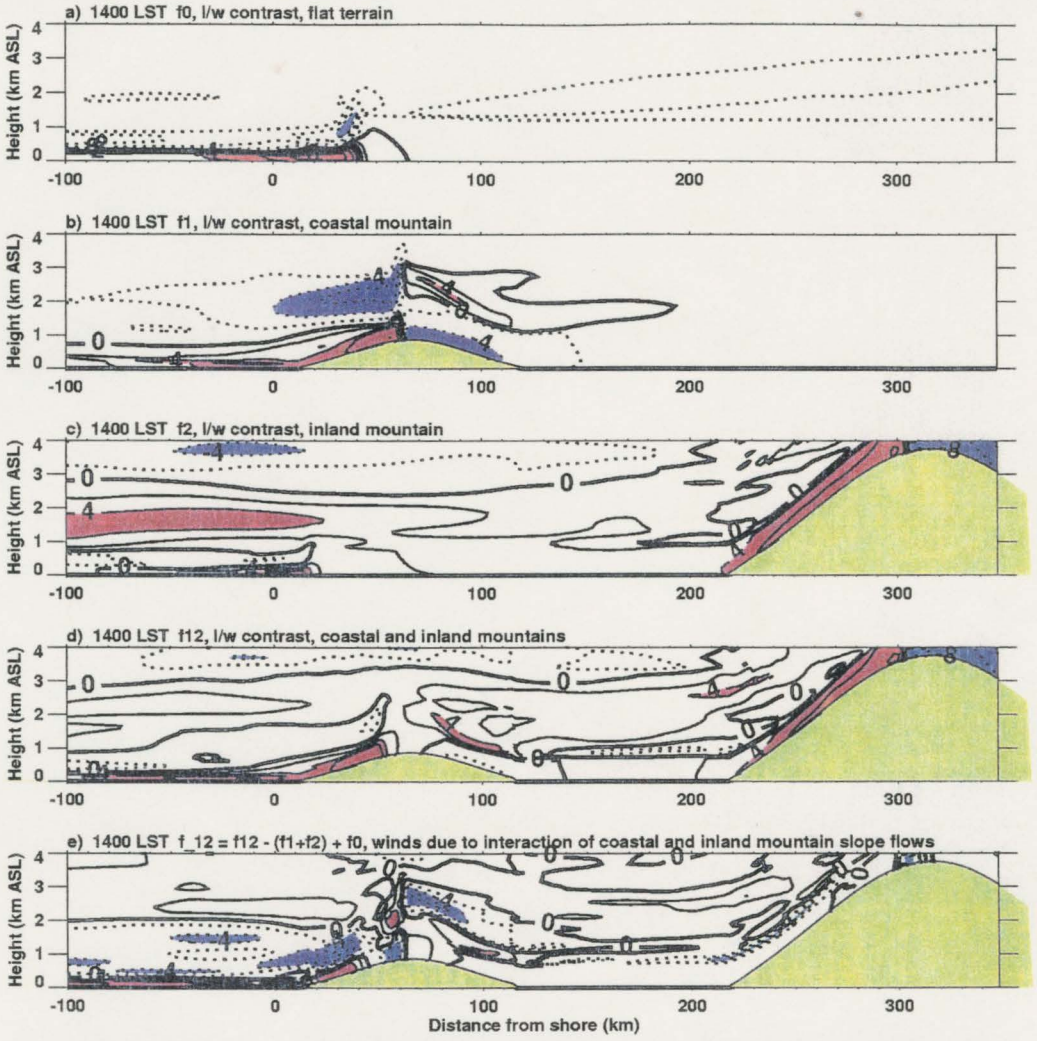

Figure 5.3 As in Fig. 5.1, but the factor pair is the coastal and inland mountains, with water in the western portion of the domain. (a) f_0 - neither mountain in the domain. (b) f_1 - coastal mountain only. (c) f_2 - inland mountain only. (d) f_{12} - both mountains. (e) $\hat{f}_{12}$ - the winds due to the interaction of the flows induced by both the coastal and inland mountains.

east side of the coastal mountain (and the interaction of flows results) were quite similar to the results in the previous factor pair, indicating that the presence of water in the western portion of the domain did not affect the winds east of the crest of the coastal mountain at this time.

Later in the day, 1800 LST (Fig. 5.4), the interaction of mountain flows continued to augment the westerly flow along the western slope of the coastal mountain, over the water and particularly at and ahead of the leading edge of the sea breeze, whereas 4 hr earlier the interaction opposed the leading edge of the sea-breeze flow. This is because of the position of the sea-breeze front in the flat-terrain simulation relative to the sea-breeze front in the simulations with the coastal mountain. The inland penetration in the flat-terrain simulation was less than in the simulations with sloping terrain at 1400 LST, but slightly ahead of the front in the sloping-terrain simulations at 1800 LST. The comparison of these results with those of the previous factor pair indicate that the presence of the sea breeze reversed the influence of the interaction of the mountain flows on the western slope of the coastal mountain and to its west.

Figures 5.5 (1400 LST) and 5.6 (1800 LST) show the plots for the idealized dual-mountain topography (f_1) and land/water contrast (f_2) factor pair. Fig. 5.5e, $\hat{f}_{12}$, shows that the interaction of these two factors had very little influence on f east of the crest of the coastal mountain. The affected region was from the crest of the coastal mountain (x = 65 km) westward, mostly in the lowest few hundred m above the surface. Where the values were negative (dashed lines), the interaction between the slope and land/water contrast opposed the modeled surface flow on the western slope of the coastal mountain

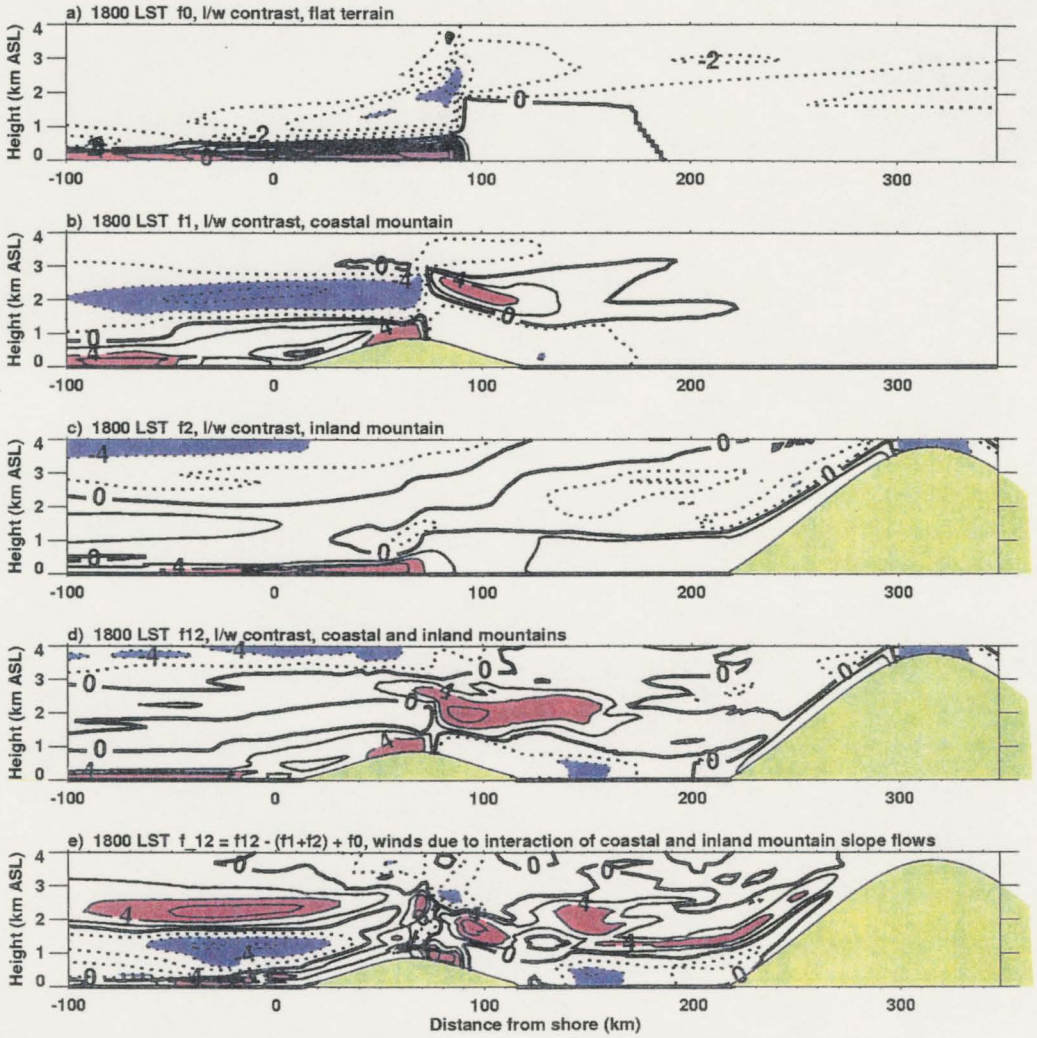

Figure 5.4 As in Fig. 5.3, except for 1800 LST, 4 hr later.

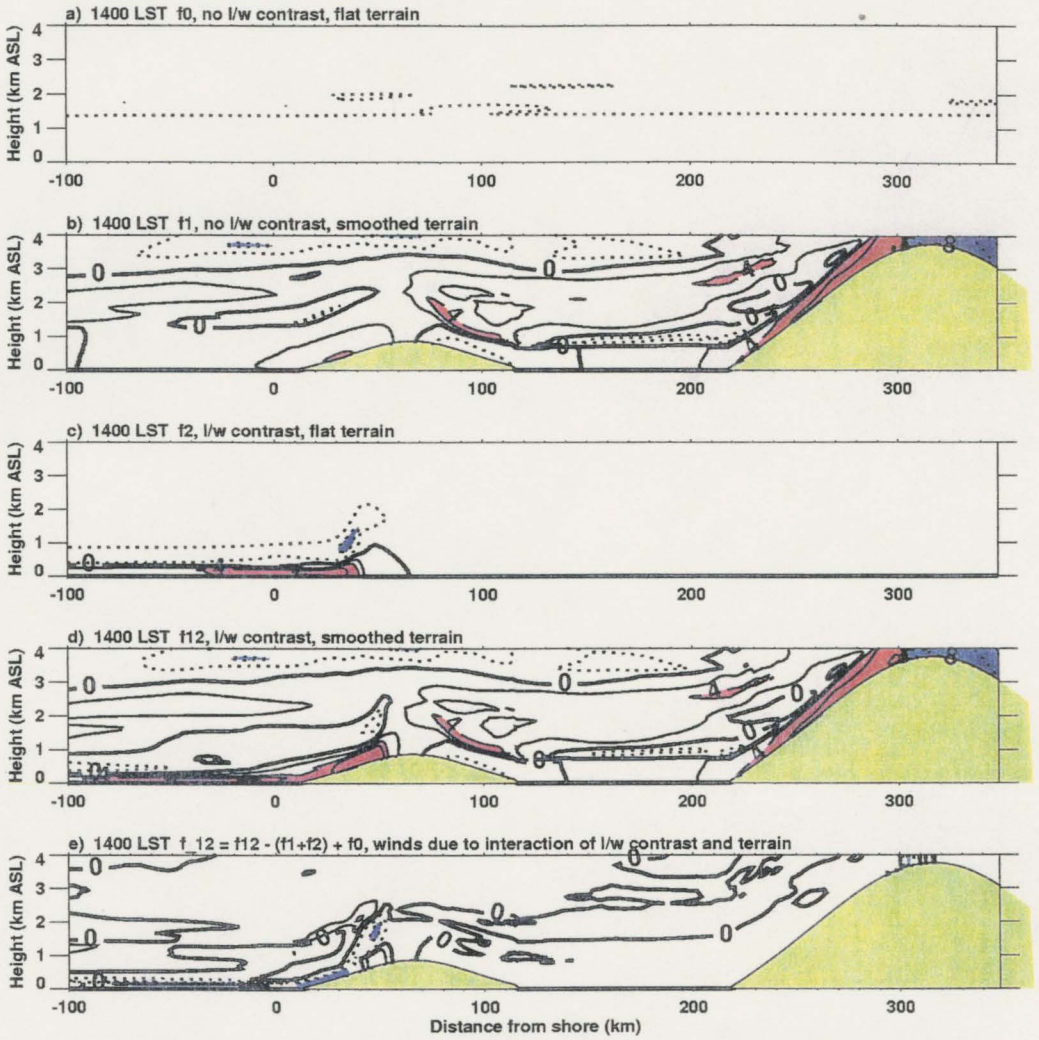

Figure 5.5 As in Fig. 5.1, but the factor pair is the land/water contrast and the idealized dual-mountains terrain. (a) f_0 - neither mountain nor water in the domain. (b) f_1 - both mountains, no water. (c) f_2 - flat terrain, with water. (d) f_{12} - both mountains. (e) $\hat{f}_{12}$ - the winds due to the interaction of the flows induced by the land/water contrast and the terrain.

and over the water (compare f_{12} to $\hat{f}_{12}$, Figures 5.5d and 5.5e, respectively). Behind the leading edge of the combined sea breeze/slope flow, however, there was a slight augmentation of the westerly flow. With time, this enhancement at the leading edge of the sea breeze weakened or reversed (Fig. 5.6e). At 1800 LST (Fig. 5.6), the interaction of the sea breeze and slope flows strongly opposed the sea breeze and upslope flow west of the crest of the coastal mountain at this time, as well as the return flow for this branch of the slope flow. There was little effect east of the coastal mountain.

Figure 5.7 shows time-height plots of $\hat{f}_{12}$ for the 3 cases discussed, and the triple interaction results, $\hat{f}_{123}$. The profiles were extracted from the shore, as were the profiles seen in Section 4.2, and illustrate the impact of the interaction of the factor pairs at the shore over time. In the case of the coastal and inland mountains with no water in the domain (Fig. 5.7a) the influence of the interaction of the slope flows near the surface occurred only in the morning and well after sunset. In the morning, the interaction acted to enhance onshore flow (red shading) until 0900 LST. During the rest of the morning and afternoon, the influence at the surface was very weak. In the evening, the interaction of the slope flows worked to enhance the offshore flow at the surface. The most significant effect of the interaction was above 1.5 km ASL during the afternoon and early evening hours.

When water was added to the domain, Fig. 5.7b, the promotion of onshore flow in the morning extended for several more hours, and had an even stronger effect than the case without water. After 1300 LST the effect was still to enhance westerly flow below 500 m, but very weakly. Above 500 m in the afternoon and early evening, easterly flow

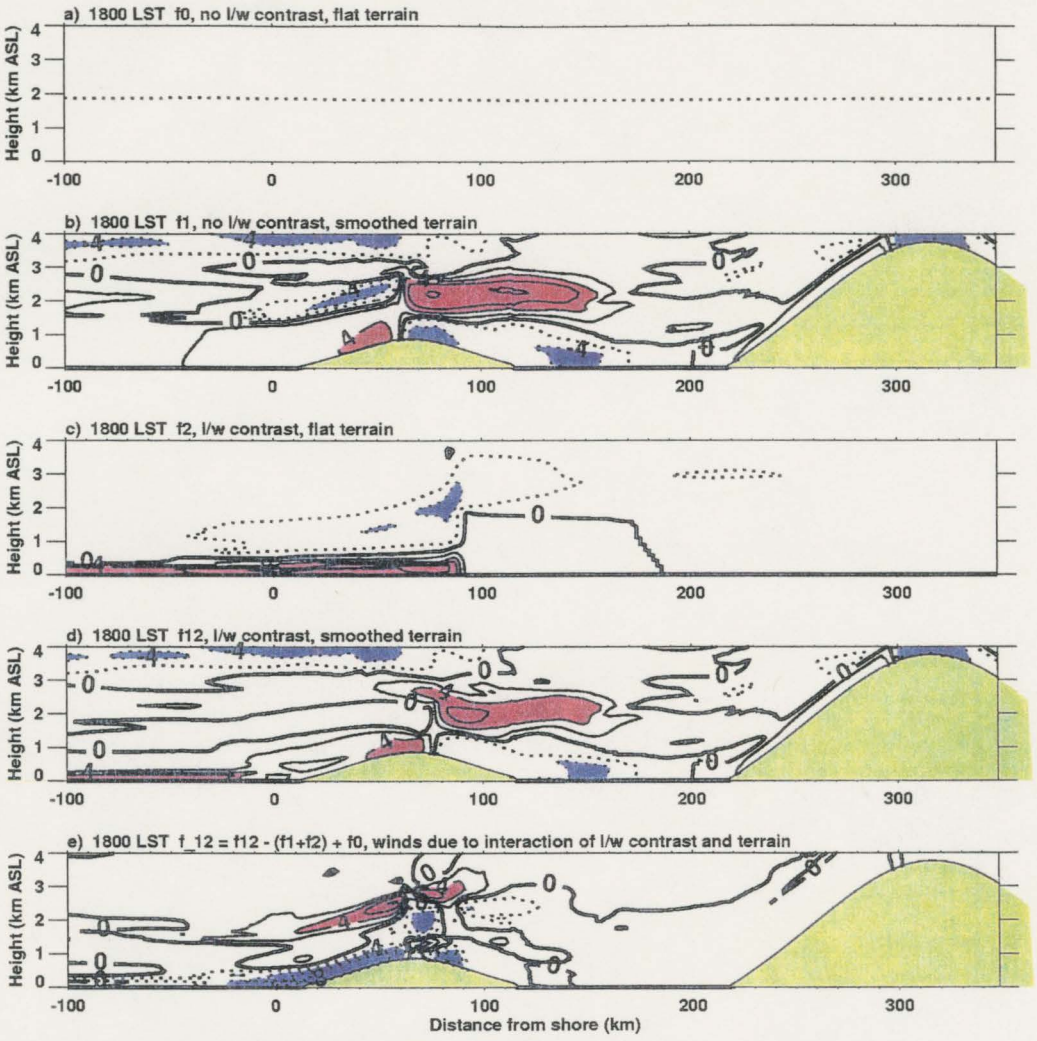

Figure 5.6 As in Fig. 5.5, except for 1800 LST, 4 hr later.

was enhanced, and then westerly flow above 2 km.

As in the $\hat{f}_{12}$ panels of the west-east cross sections, the interaction between the terrain- induced flows and the land/water contrast flows opposed the sea breeze flow in

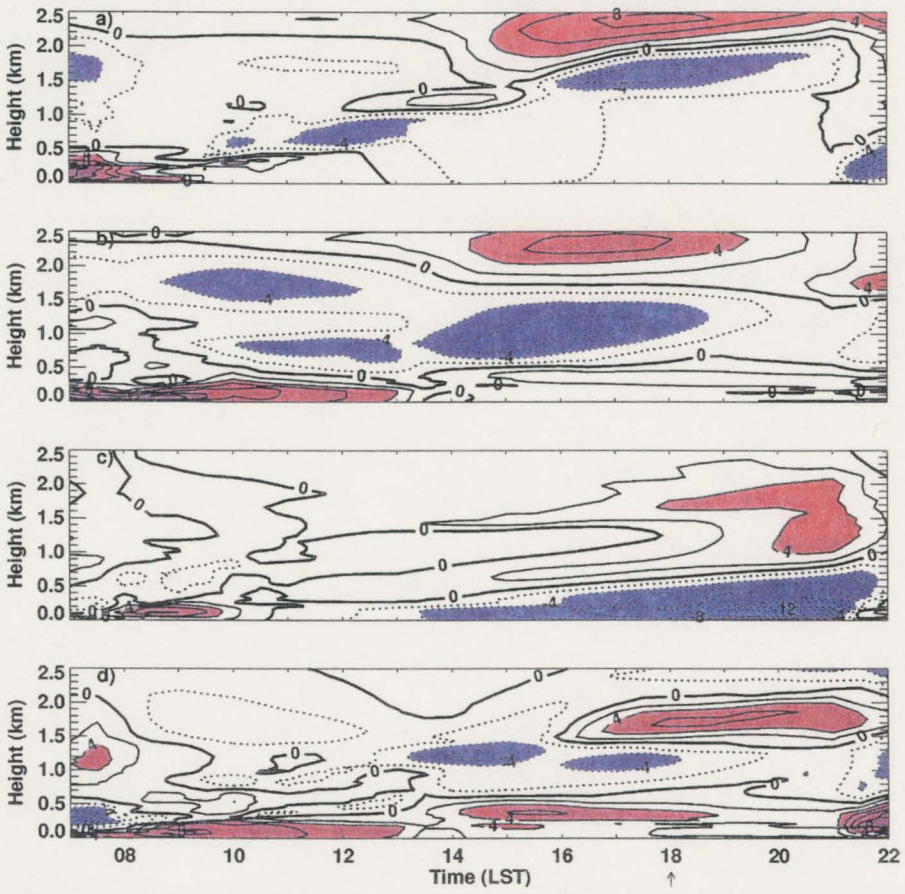

Figure 5.7 Time-height cross section of the calculated $\hat{f}_{12}$ field for the three factor pair cases presented and $\hat{f}_{123}$, the triple interaction. Solid contours represent westerly flow, dashed contours represent easterly flow. Red regions (westerly flow greater than 4 m s^{-1}) show where westerly flow was enhanced by the interactions. Blue regions (easterly flow greater than 4 m s^{-1}) indicate where easterly flow was enhanced by the interactions. (a) Flow due to the interaction of mountain induced flows, no water in the domain. (b) Flow due to the interaction of mountain induced flows, with water in the domain. (c) Flow due to the interaction of the flows due to the land/water contrast and the terrain. (d) Flow due to the triple interaction of the coastal mountain, inland mountain, and the land/water contrast.

the late afternoon and early evening (Fig. 5.7c). The strongest influence on the onshore surface flow was from 0800 to 1000 LST, with the onshore flow slightly augmented in a shallow layer. The augmentation of the morning sea breeze was weaker than in the mountain-flow interaction factor pair. During the sea breeze development phase, however, the influence was quite weak. From 1400 LST on, the interaction of the land/water contrast and the slope flows worked to oppose the sea breeze flow, particularly after sunset, in agreement with Kondo's (1990) findings that the sea breeze was enhanced in the morning and opposed in the afternoon when terrain was present. Above 500 m, it was only after sunset that the interaction had a major contribution at the shore. The results below 500 m ASL for the factor pairs with water in the domain (Figures 5.7 b and 5.7c) show that the interaction of mountain flows dominated in the morning (enhancing the sea breeze flow), whereas the interaction of the land/sea contrast and sloping terrain dominated in the afternoon (opposing the sea-breeze flow and enhancing the return to offshore flow after sunset).

The effects of the triple interaction among the coastal mountain, inland mountain, and the land/water contrast are shown in Fig. 5.7d. Except for the first 1.5 hr in the morning, the interaction below 500 m ASL enhanced the onshore flow. The development of the shallow sea breeze was strongly enhanced at ~0900 LST, which corresponded to the time of sea breeze onset seen in Fig. 4.12b, the time-height series of u from the simulation that included all three factors. After 1400 LST, the enhancement was elevated ~300 m from earlier in the day, corresponding to the onset of the deeper portion of the sea breeze.

Chapter 6

Summary and future work

6.1 Summary

The NOAA/ETL Doppler lidar deployed at Monterey Bay in September 1987 successfully measured the vertical structure of the sea breeze with high spatial-resolution scans perpendicular to the shore. The lidar measurements agree with surface station measurements on the timing of the wind shifts near the shore, and the vertical profiles of lidar winds agree with data from soundings launched from the R/V Silver Prince, stationed west of Monterey Bay (Banta et al. 1993). The complex terrain surrounding the Monterey Bay area causes the sea breeze to be more complex than predicted by theory, and the structure is highly three-dimensional. Nearly horizontal lidar scans show the horizontal variability quite well. Nevertheless, the lidar cross sections perpendicular to the coast yield much information about the vertical structure of the Monterey Bay sea breeze, and using them to assess model performance is a good starting point for numerically investigating the sea breeze.

The time-height series of the lidar-measured u-component of the wind, shown in Fig. 4.14, was comprised of 31 profiles obtained over 15 hours, an average of 1 profile every half-hour. Because the lidar has a narrow beam, the high-vertical resolution (28 m at 8 km range) allowed for detailed measurements that would be difficult to obtain

simultaneously over both land and water by other measurement schemes. The life-cycle of the sea breeze on 16 September 1987, as measured by the lidar and presented in Fig. 4.14, was as follows. Deep offshore flow in the morning that was too deep and strong to be a land breeze lasted until ~1000 LST. This deep layer of offshore flow was associated with a large-scale high pressure system centered off the west coast of the United States. A gradual transition to a shallow sea breeze occurred underneath the strong offshore flow from 1000 to 1200 LST. A sudden expansion to a deeper sea breeze occurred around 1200 LST, and two scales of onshore flow coexisted until the stronger, shallower sea breeze and the weaker, deeper sea breeze blended together. Once the deeper sea breeze became established, weak offshore flow lying above the sea breeze became more well defined. Four hours after sunset the switch to offshore flow began.

The time-height plots of the RAMS modeled *u*-component of the wind in the dual-mountain simulations replicated some of the key features seen in the lidar measurements, particularly the shallow and deep onshore flow. Comparisons between the time-height series of the simulations with and without the land/water contrast indicated that the coastal mountain was responsible for the weaker, deeper westerly flow. Comparing simulations with and without the coastal mountain made it clear that the land/water contrast was responsible for the stronger, shallow sea breeze.

Model results were more realistic in the lowest 1500 m of the domain. Low-angle lidar PPI scans indicated that the onshore flow was most likely to be perpendicular to the shore at the lowest levels (Fig. 2.3), and therefore the lower-level winds were more likely to be successfully reproduced in a 2-D model domain that was perpendicular to the shore.

Lidar data indicate that with time, the wind direction did change with height, and the winds were not always parallel to the shore. 2-D simulations could not account for these changes, particularly above 1500 m AGL, where the agreement between lidar and RAMS simulations was less successful.

Factor separation results (Figures 5.1 - 5.7) for the idealized dual-mountain sea-breeze simulation (Fig. 4.12b) showed that the interaction between the coastal and inland mountains was a dominating force in the morning hours, enhancing the onshore flow. The interaction between terrain and the land/water contrast was a dominating force in the afternoon, opposing the sea breeze flow. While the coastal mountain slope flow acted to enhance the sea breeze flow, particularly in the morning, the mountain also acted as a barrier to the sea breeze, impeding its progress in the afternoon. The triple interaction among the coastal and inland mountains and the land/water contrast worked to enhance onshore flow at the surface for the whole time period analyzed (0700 to 2200 LST). However, this enhancement became quite weak in the afternoon when the opposing effects due to the interaction of the land/water contrast and terrain became very strong.

The results of the interactions above the sea breeze layer, where the expected return flow would be, were not clear cut. The triple interaction and the interaction of the mountain flows acted to promote easterly flow from 500 to 1500 m AGL in the afternoon, yet only very weak easterly flow was seen at this time in the dual-mountain simulations. The factor separation results did not explain the early morning westerly flow above 2 km either, although in the time-height series comparison this flow was clearly associated with the inland mountain.

6.2 Future work

The next logical step in continuing this case study would be to execute nested-grid 3-D simulations, since this is obviously a 3-D problem. In this scenario, the Coriolis parameter would also be included in the simulations. East-west cross sections could be extracted along the same latitude as the lidar deployment and compared to both lidar data and the 2-D east-west slices. This would provide more information about effects of the terrain on the vertical structure of the sea breeze and return flow. The horizontal variability as measured by the lidar, particularly the effects of the Salinas River valley, could be examined with constant height slices of the wind fields, analyzing the influences of terrain.

Using the factor separation method of Stein and Alpert (1993), sensitivity studies of more factors could be done. Additional factors of interest include soil moisture, land use changes in the San Joaquin valley, different ambient wind directions, grid spacing, and changes in sea surface temperature.

Recent advances in remote sensing bring new ways to more closely investigate the sea breeze. Doppler lidars are now deployed on both ships and aircraft. Flights legs across Monterey Bay and across the San Joaquin valley to the slope of the Sierras with a Doppler lidar taking measurements in the boundary layer would provide a wealth of information regarding the slope flows, sea breeze penetration, layers of flow, etc. Lidars with spatial and temporal resolution greater than the system used in LASBEX take measurements with less range, but turbulent quantities can be calculated with the measurements, and with 30 m along-beam resolution, much smaller wind features can be

resolved. Measurements like these would complement the measurements obtained by the Doppler lidar used during LASBEX.

With the proliferation of radar wind profilers with radio acoustic sounding systems (RASS), and the ability to deploy these systems on buoys, a future sea breeze experiment in the Monterey Bay area could include a network of profilers over land and water, and the data could then be ingested into 3-D RAMS simulations. Profilers operate 24 hr a day, and the hourly wind profiles would be invaluable for successfully modeling the sea breeze and the wind flows in which they are imbedded.

References

Arritt, R.W., 1989: Numerical modelling of the offshore extent of sea breezes. *Quart. J. Roy. Meteor. Soc.*, **115**, 547-570.

Atkins, N.T. and R.M. Wakimoto, 1997: Influence of the synoptic-scale flow on sea breezes observed during CaPE. *Mon. Wea. Rev.*, **125**, 2112-2130.

Atkinson, B.W., 1981: *Mesoscale Atmospheric Circulations*. Academic Press, 125-214.

Avissar, R., M..D. Moran, G. Wu, R.N. Meroney, and R.A. Pielke, 1990: Operating ranges of mesoscale numerical models and meteorological wind tunnels for the simulation of sea and land breezes. *Boundary-Layer Meteorol., **50**, 227-275.*

Banta, R.M., 1995: Sea breezes shallow and deep on the California coast. *Mon. Wea. Rev.*, **123**, 3614-3622.

_____, L. D. Olivier, and D. H. Levinson, 1993: Evolution of the Monterey Bay sea-breeze layer as observed by pulsed Doppler lidar. *J. Atmos. Sci.*, **50**, 3959-3982.

_____, L. S. Darby, P. Kaufman, D. H. Levinson, and C. J. Zhu, 1999: Wind flow patterns in the Grand Canyon as revealed by Doppler lidar. *J. Appl. Meteor.*, **38**, 1069-1083.

_____, P. B. Shepson, J. W. Bottenheim, K. G. Anlauf, H. A. Wiebe, A. Gallant, T. Biesenthal, L. D. Olivier, C. J. Zhu, I. G. McKendry, and D. G. Steyn, 1997: Nocturnal cleansing flows in a tributary valley. *Atmos. Environ.*, **31**, 2147-2162.

Browning, K.A., and R. Wexler, 1968: The determination of kinematic properties of a wind field using a Doppler radar. *J. Appl. Meteor.*, **7**, 105-113.

Chen, Y. and J. Li, 1995: Characteristics of surface airflow and pressure patterns over the island of Taiwan during TAMEX. *Mon. Weather Rev.*, **123**, 695-716.

Cui, Z., M. Tjernstrom, and B. Grisogono, 1998: Idealized simulations of atmospheric coastal flow along the central coast of California. *J. Appl. Meteor.*, **37**, 1332-1363.

Darby, L. S., W. D. Neff, and R. M. Banta, 1999: Multiscale analysis of a Meso-α frontal passage in the complex terrain of the Colorado Front Range. *Mon. Weather Rev.*, **127**, 2062-2081.

Doyle, J.D., 1997: The influence of mesoscale orography on a coastal jet and rainband. *Mon. Weather Rev.*, **125**, 1465-1488.

Eastman, J.L., R.A. Pielke, and W.A. Lyons, 1995: Comparison of lake-breeze model simulations with tracer data. *J. Appl. Meteor.*, **34**, 1398-1418.

Estoque, M.A., 1961: A theoretical investigation of the sea breeze. *Quart. J. Roy. Meteor. Soc.*, **87**, 136-146.

_____, 1962: The sea breeze as a function of the prevailing synoptic situation. *J. Atmos. Sci.*, **19**, 244-250.

Fagan, M., 1988: The sea breeze circulation during the Land Sea Breeze Experiment (LASBEX) in central California. M.S. thesis, Department of Meteorology, Naval Postgraduate School, Monterey, California 93943-5000, 127 pp.

Fisher, E.L., 1960: An observational study of the sea breeze. *J. Meteor.*, **17**, 645-660.

_____, 1961: A theoretical study of the sea breeze. *J. Meteor.*, **18**, 216-233.

Frenzel, C.W., 1962: Diurnal wind variations in Central California. *J. Appl. Meteor.*, **1**, 405-412.

Guan, S., P.L. Jackson, and C.J.C. Reason, 1998: Numerical modeling of a coastal trapped disturbance. Part I: Comparison with observations. *Mon. Wea. Rev.*, **126**, 972-990.

Haurwitz, B., 1947: Comments on the sea-breeze circulation. *J.. Meteor.*, **4**, 1-8.

Holland, G.J., and J.L. McBride, 1989: Quasi-trajectory analysis of a sea-breeze front. *Quart. J. Roy. Meteor. Soc.*, **115**, 571-580.

Holton, J.R., 1992: *An introduction to dynamic meteorology*. Academic Press, 87-92.

Intrieri, J.M., C.G. Little, W.J. Shaw, R.M. Banta, P.A. Durkee, and R.M. Hardesty, 1990: The Land/Sea Breeze Experiment (LASBEX). *Bull. Amer. Meteor. Soc.*, **71**, 656-664.

Jackson, P.L., C.J.C. Reason, and S. Guan, 1999: Numerical modeling of a coastal

trapped disturbance. Part II: Structure and dynamics. *Mon. Wea. Rev.*, **127**, 535-550.

Johnson, A., Jr., and J.J. O'Brien, 1973: A study of an Oregon sea breeze event. *J. Appl. Meteor.*, **12**, 1267-1283.

Johnson, R. and R.F. Bresch, 1991: Diagnosed characteristics of precipitation systems over Taiwan during the May-June 1987 TAMEX. *Mon. Weather Rev.*, **119**, 2540-2557.

Kimura F. and T. Kuwagata, 1993: Thermally induced wind passing from plain to basin over a mountain range. *J. Appl. Meteor.*, **32**, 1538-1547.

Kitada, T., K. Okamura, and S. Tanaka, 1998: Effects of topography and urbanization on local winds and thermal environment in the Nohbi Plain, coastal region of central Japan: A numerical analysis by mesoscale meteorological model with a [illegible]-[illegible] turbulence model. *J. Appl. Meteor.*, **37**, 1026-1046.

Kolev, I., O. Parvanov, B. Kaprielov, E. Doney, and D. Ivanov, 1998: Lidar observations of sea-breeze and land-breeze aerosol structure on the Black Sea. *J. Appl. Meteor.*, **37**, 982-995.

Kotroni, V., G. Kallos, K. Lagouvardos, M. Varinou, and R. Walko, 1999: Numerical simulations of the meteorological and dispersion conditions during an air pollution episode over Athens, Greece. *J. Appl. Meteor.*, **38**, 432-447.

Kondo, H., 1990: A numerical experiment on the interaction between sea breeze and valley wind to generate the so-called "extended sea breeze". *J. Meteor. Soc. Japan*, **68**, 435-446.

Lyons, W.A. and L.E. Olsson, 1973: Detailed mesometeorological studies of air pollution dispersion in the Chicago lake breeze. *Mon. Weath. Rev.*, **101**, 387-403.

Lu, R., and R.P. Turco, 1994: Air pollutant transport in a coastal environment. Part I: Two-dimensional simulations of sea-breeze and mountain effects. *J. Atmos. Sci.*, **51**, 2285-2308.

Mahrer, Y., and R.A. Pielke, 1977: The effects of topography on sea and land breezes in a two-dimensional numerical model. *Mon. Weath. Rev.*, **105**, 1151-1162.

McPherson, R.D., 1970: A numerical study of the effect of a coastal irregularity on the sea breeze. *J. Appl. Meteor.*, **9**, 767-777.

Meyer, J.H., 1971: Radar observations of land breeze fronts. *J. Appl. Meteor.*, **10**, 1224-1232.

Mizuma, Mitsuo, 1995: General aspects of land and sea breezes in Osaka Bay and surrounding area. *J. Meteor. Soc. Japan*, **73**, 1029-1040.

Mizzi, A.P. and R.A. Pielke, 1984: Numerical study of the mesoscale atmospheric circulation observed during upwelling event on 23 August 1972, Pt. 1, Sensitivity studies. *Mon. Wea. Rev.*, **112**, 76-90.

Moroz, W.J., 1967: A lake breeze on the eastern shore of Lake Michigan: Observations and model. *J. Atmos. Sci.*, **24**, 337-355.

Nakane, H., and Y. Sasano, 1986: Structure of a sea-breeze front as revealed by a scanning lidar observation. *J. Meteor. Soc. Japan*, **64**, 787-792.

Neumann, J., and Y. Mahrer, 1971: A theoretical study of the land and sea breeze circulation. *J. Atmos. Sci.*, **28**, 532-542.

Ookouchi, Y., M. Uryu, and R. Sawada, 1978: A numerical study on the effects of a mountain on the land and sea breezes. *J. Meteor. Soc. Japan*, **56**, 368-385.

Pearce, R.P., 1955: The calculation of a sea-breeze circulation in terms of the differential heating across the coastline. *Quart. J. Roy. Meteor. Soc.*, **81**, 351-381.

Physick, W., 1976: A numerical model of the sea-breeze phenomenon over a lake or gulf. *J. Atmos. Sci.*, **33**, 2107-2135.

Pielke, R.A., 1973: A three dimensional numerical model of the sea breezes over South Florida. Ph.D. dissertation, The Pennsylvania State University, 135 pp.

_____, 1974: A three-dimensional numerical model of the sea breeze over south Florida. *Mon. Weath. Rev.*, **102**, 115-139.

_____, 1984: *Mesoscale meteorological modeling*. Academic Press, 612 pp.

_____, Sr., R.L. Walko, L.T. Steyaert, P.L. Vidale, G.E. Liston, W.A. Lyons, and T.N. Chase, 1999: The influence of anthropogenic landscape changes on weather in south Florida. *Mon. Wea. Rev.*, **127**, 1663-1673.

Post, M.J., and R.E. Cupp, 1990: Optimizing a pulsed Doppler lidar. *Appl. Opt.*, **29**, 4145-4158.

Reason, C.J.C, K.J. Tory, and P.L. Jackson, 1999: Evolution of a southeast Australian coastally trapped disturbance. *Meteor. Atmos. Phys.*, **70**, 141-165.

Reible, D.D., J.E. Simpson and P.F. Linden, 1993: The sea breeze and gravity-current frontogenesis. *Quart. J. Roy. Meteor. Soc.*, **119**, 1-16.

Schmidt, F.H., 1947: An elementary theory of the land- and sea-breeze circulation. *J.. Meteor.*, **4**, 9-15.

Schroeder, M.M., M.A. Fosberg, O.P. Cramer, and C.A. O'Dell, 1967: Marine air invasion of the Pacific coast: A problem analysis. *Bull. Amer. Meteor. Soc.*, **48**, 802-808.

Simpson, J.E., 1994: *Sea breeze and local winds*. Cambridge University Press, 234 pp.

_____, Mansfield, D.A. and Milford, J.R., 1977: Inland penetration of sea-breeze fronts. *Quart. J. Roy. Meteor. Soc.*, **103**, 47-76.

Skinner, T. and N. Tapper, 1994: Preliminary sea breeze studies over Bathurst and Melville Islands, Northern Australia, as part of the Island Thunderstorm Experiment (ITEX). *Meteor. Atmos. Phys.*, **53**, 77-94.

Snook, J.S., P.A. Stamus, J. Edwards, C. Zaphiris, and J.A. McGinley, 1998: Local-domain mesoscale analysis and forecast model support for the 1996 Centennial Olympic Games. *Wea. Forecasting*, **13**, 138-150.

Stein, U., and P. Alpert, 1993: Factor separation in numerical simulations. *J. Atmos. Sci.*, **50**, 2107-2115.

Tremback, C.J., and R.L. Walko, 1994: RAMS technical manual (draft). ASTeR Division of MRC, 50 pp.